Experimental validation of the Topological Sensitivity approach to elastic-wave imaging

A DISSERTATION
SUBMITTED TO THE FACULTY OF THE GRADUATE SCHOOL
OF THE UNIVERSITY OF MINNESOTA
BY

Roman D. Tokmashev

IN PARTIAL FULFILLMENT OF THE REQUIREMENTS
FOR THE DEGREE OF
Doctor of Philosophy

Bojan B. Guzina

August, 2015

Acknowledgements

I would like to thank my adviser, Prof. Bojan Guzina, for his major support in my research and education during the Ph.D. program. His input significantly helped me grow academically and fostered my deeper understanding of challenging technical problems which in turn brought me to successful results.

Next, all the effort of the committee members, namely Professors J. Labuz, S. Gonella, and F. Santosa, is highly appreciated.

I'm also very grateful to all my instructors from the Novosibirsk State University and the University of Minnesota for giving me state-of-the-art knowledge and enhancing my analytical skills which significantly helped me during the course of my Ph.D.

The financial support is provided by the Department of Energy via Nuclear Energy University Programs (NEUP) Grant #10-862 and Sommerfeld Fellowship, endowed Shimizu Professorship.

Dedication

In memory of a remarkable person and instructor, Sergey I. Chikichev.

Abstract

The focus of this dissertation is on: i) non-invasive imaging of discrete damage in solids by way of the Topological Sensitivity (TS) approach to elastic-wave tomography, ii) experimental verification of the TS imaging technique using non-contact vibration measurements obtained by 3D Scanning Laser Doppler Vibrometer, and iii) upgrade of the Finite Element (FE) elastodynamic computational platform to treat long range wave propagation toward enhancing the imaging performance of TS under the conditions of limited testing aperture.

Contents

List of Tables

List of Figures

Chapter 1

Introduction

In applied mathematics and engineering, the past two decades have witnessed the flourish of a diverse array of non-iterative techniques for tackling inverse scattering problems that dispense with the "legacy" (simplifying and computational) deterrents to customary linearization and nonlinear optimization strategies [1, 2, 3, 4] for waveform tomography. As examples, one may mention the linear sampling method [5, 6], the factorization method [7], the reciprocity gap approach [8] and the probe method [9] in terms of extended scatterers, as well as the multiple signal classification (MUSIC) algorithm [10], the time reversal approaches [11, 12], and the direct method [13, 14] as techniques catering primarily for point-like but also extended targets [15, 16].

Another technique in the same vein, that is the focus of this study, is the method of topological sensitivity (TS) [17, 18, 19] rooted in the theories of shape optimization [20, 21, 22]. Over the past decade, this method has emerged as an effective tool for non-iterative treatment of the inverse scattering problems in acoustics [23, 24, 25, 26], electromagnetism [27, 28], and elastodynamics [29, 30, 31, 32, 33] entailing extended obstacles. Mathematically, the TS signifies the obstacle-size-independent factor in the leading-order perturbation of a given (say L^2) cost functional when an infinitesimal scatterer is introduced in the *reference* (homogeneous or heterogeneous) domain whose properties are known beforehand. In terms of waveform tomography, this quantity is then used as *obstacle indicator* through an assembly of sampling points where it attains pronounced negative values. Typically, the TS formulas are expressible as a bilinear form in terms of germane (free and adjoint) fields defined over the reference domain, which

lends itself to an effective computation of the indicator function. One notable drawback of the TS approach in regard to the aforementioned alternatives is that the justification of its performance has been largely heuristic; however, several recent works [30, 34, 35] have made strides toward surpassing this limitation.

On the verification side, the effectiveness of topological sensitivity as an obstacle reconstruction tool has been substantiated by an extensive set of numerical simulations, see e.g. [17, 19, 29, 30, 31, 32] in the context of elastic waves. It is universally acknowledged, however, that "it's only with data that a link to reality can be forged" [36]. To this end, several recent works [37, 38, 39] have examined the variants of the TS approach, of the topological energy (TE) type, in an experimental setting. In essence, the TE-based indicators in [37, 38] and [39] represent heuristic reductions of their TS predecessor (written in terms of the same free and adjoint fields) that forgo the information about the geometry and material characteristics of a vanishing obstacle. Notwithstanding such simplification, the two-dimensional reconstructions of multiple defects via elastic waves in [37] and acoustic waves in [39] (that deploy "dense" linear ultrasonic arrays) have been shown to be highly effective.

To date, however, systematic experimental investigations of the genuine TS indicator function as a tool for tackling inverse scattering problems are still lacking. To help bridge the gap, this study deploys the topological sensitivity in a laboratory setting toward obstacle reconstruction using elastic waves in a thin aluminum plate (2D), and in a nuclear graphite block (3D) endowed with discrete internal defects. In the approach, the specimens are excited by a single piezoelectric transducer, while monitoring the induced motion on the surface via a Scanning Laser Doppler Vibrometer (SLDV) system. In this setting, the source aperture is controlled by repeating the experiment for a number of transducer locations. By deploying a time-domain Finite Element Model (FEM) to simulate the free and adjoint fields in the damage-free (reference) domain, the TS obstacle reconstruction is effected under varying experimental conditions. The results show a good accord between the defect geometry and regions where the topological sensitivity attains pronounced negative values. The influences of key testing parameters on the fidelity of TS reconstruction, including the rate of excitation, the source aperture, and the temporal length of experimental observations, are investigated. From the analysis point of view, it is shown that the use of a continuous, compactly-supported temporal

windowing function in specifying the L^2 cost functional (from which the TS derives) is critical both theoretically and numerically.

When imaging in finite domains in difficult testing conditions, i.e. when the sensory data are only available from a (small) portion of the outer boundary and/or when the excitation does not provide sufficient illumination of internal defects, one way to effectively enrich the recorded scattering information is to increase the duration of the observed wave propagation such that the anomalies are also probed by numerous waves reflected from the outer boundaries. The latter, however, poses a major demand on the accurate numerical treatment of the free and adjoint fields describing the long-range transient wave propagation problem. In the last part of this study, an effort is made towards upgrading the conventional FEM treatment to a more robust and accurate numerical wave propagation tool based on the Discontinuous Galerkin (DG) approach. Driven by the need to minimize the accumulated numerical error in the simulated waveform, the so-called Arbitrary high-order DERivative Discontinuous Galerkin method (ADER-DG) [40, 41] was implemented in Matlab and shown to accurately capture the behavior of elastic waves after propagating $O(10)$ wavelengths from the source. While producing accurate numerical results, that are the hallmark of DG methods, auxiliary degrees of freedom are added to the system which cater for discontinuities in the numerical solution – thus significantly increasing the computational cost both in terms of required memory and CPU time. In an attempt to compensate for the latter, an effort was also made towards parallelizing the computations. Using Runge-Kutta DG method (RKDG) [42], good scalability of the method was demonstrated on a multicore architecture with the aid of parallel implementation in an open-source finite element software package FEniCS [43]. Equipped with the latter, accurate 3D simulations of the free and adjoint fields underpinning the TS imaging of a nuclear graphite block were performed. The results demonstrated, for the first time, the capability of the TS approach to elastic waveform tomography in the situations of testing with poor excitation and sensing apertures.

Thesis outline Chapter 2 introduces the concept of topological sensitivity pertaining to the inverse scattering of transient elastic waves in (2D and 3D) finite homogeneous reference solids. In this setting, the TS analysis is formulated for generality within two alternative frameworks, catering respectively for the sensory data in the form of

particle displacement and particle velocity. It is also shown that the use of a smoothing temporal windowing function in specifying the L^2-norm misfit between the model and the data (that forms the basis for the TS formulation) is essential from both theoretical and computational points of view. Chapter 3 then introduces the experimental motion sensing platform that makes us of the 3D scanning laser Doppler Vibrometer. The experimental setups are presented for SLDV-TS testing of a plate (2D plane stress) and a block (3D) specimen. Next, Chapter 4 introduces the computational platform based on the conventional (continuous Galerkin) finite element method. For verification purposes, given in this chapter are also the results of preliminary synthetic imaging in the graphite block. Chapter 5 is dedicated for the results of experimental TS imaging in both plate and block specimens – including parametric studies under varying experimental configurations. Based on the obtained results, it is concluded that one major source of error in the evaluated TS distributions is affiliated with the numerical dispersion pertaining to the long-range propagation of numerical wavefields. Finally, Chapter 6 makes an attempt to mitigate the effect of the latter error via more accurate and robust computational treatment based on the discontinuous Galerkin method. In conclusion, Chapter 7 summarizes the main findings of this study.

Chapter 2

Theoretical background

This section briefly introduces the Topological Sensitivity (TS) approach for non-invasive defect reconstruction in the scope of transient elastodynamics. It also examines a particular restriction on the L^2-norm misfit function (featured by the germane cost functional) that guarantees the validity of the conventional bilinear representation of the TS formula in terms of the Riemann convolution between the free and adjoint elastodynamic states.

2.1 Forward problem

Let $\mathbb{R}_{\mathrm{T}} = (-\infty, T]$ denote a time interval, and let $\Omega \in \mathbb{R}^d$, $d = 2, 3$, be an open connected set with boundary $S = \partial\Omega$ representing the support of a *reference* isotropic elastic body (hereafter $d = 2$ is employed for a plane-stress case) endowed with Young's modulus E, Poisson's ratio ν, and mass density ρ. A cavity (or a set thereof) B, bounded by the traction-free surface $\Gamma = \partial B$, is embedded in Ω. To facilitate the analysis, the external surface S of the cavitated body $\Omega^- = \Omega \backslash \overline{B}$ is split into a Dirichlet part S^{D} and Neumann part S^{N}, associated respectively with prescribed displacements $\boldsymbol{u}^\star \in C^1(S^{\mathrm{D}} \times \mathbb{R}_{\mathrm{T}})$ and surface tractions $\boldsymbol{t}^\star \in C^0(S^{\mathrm{N}} \times \mathbb{R}_{\mathrm{T}})$, where the featured continuity requirements are understood in the sense of [44]. Assuming further that $\boldsymbol{u}^\star$ and $\boldsymbol{t}^\star$ have *quiescent past*, i.e. , thus induced elastodynamic state $[\boldsymbol{u}_{\mathrm{B}}, \boldsymbol{\sigma}[\boldsymbol{u}_{\mathrm{B}}]]$ in Ω^- satisfies the field equations

and boundary conditions

$$\begin{aligned}
\nabla\cdot\boldsymbol{\sigma}[\boldsymbol{u}_{\mathrm{B}}](\boldsymbol{\xi},t)-\rho\,\ddot{\boldsymbol{u}}_{\mathrm{B}}(\boldsymbol{\xi},t) &= \mathbf{0} && \text{on} \quad \Omega^{-}\times\mathbb{R}_{\mathrm{T}},\\
\boldsymbol{n}\cdot\boldsymbol{\sigma}[\boldsymbol{u}_{\mathrm{B}}](\boldsymbol{\xi},t) &= \mathbf{0} && \text{on} \quad \Gamma\times\mathbb{R}_{\mathrm{T}},\\
\boldsymbol{n}\cdot\boldsymbol{\sigma}[\boldsymbol{u}_{\mathrm{B}}](\boldsymbol{\xi},t) &= \boldsymbol{t}^{\star} && \text{on} \quad S^{\mathrm{N}}\times\mathbb{R}_{\mathrm{T}},\\
\boldsymbol{u}_{\mathrm{B}}(\boldsymbol{\xi},t) &= \boldsymbol{u}^{\star} && \text{on} \quad S^{\mathrm{D}}\times\mathbb{R}_{\mathrm{T}},\\
\boldsymbol{u}_{\mathrm{B}}(\boldsymbol{\xi},t) &= \mathbf{0} && \text{on} \quad \Omega^{-}\times\mathbb{R}_{0}.
\end{aligned} \tag{2.1}$$

Here $\boldsymbol{u}_{\mathrm{B}}\in C^2(\Omega^-\times\mathbb{R}_{\mathrm{T}})\cap C^1(\overline{\Omega^-}\times\mathbb{R}_{\mathrm{T}})$ denotes the displacement vector, and $\boldsymbol{\sigma}[\boldsymbol{u}_{\mathrm{B}}]=\boldsymbol{C}:\nabla\boldsymbol{u}_{\mathrm{B}}\in C^0(\overline{\Omega^-}\times\mathbb{R}_{\mathrm{T}})$ is the affiliated Cauchy stress tensor [44]; $\dot{f}=\partial f/\partial t$; $\boldsymbol{n}$ is the outward normal on $\partial\Omega^-$; $\mathbb{R}_0=(-\infty,0]$, and $\boldsymbol{C}$ is the isotropic elasticity tensor given by

$$\boldsymbol{C}=\lambda_d\,\boldsymbol{I}_2\otimes\boldsymbol{I}_2+2\mu\,\boldsymbol{I}_4,\qquad \lambda_2=\frac{E\nu}{1-\nu^2},\qquad \lambda_3=\frac{E\nu}{(1+\nu)(1-2\nu)},\qquad \mu_2=\mu_3=\mu=\frac{E}{2(1+\nu)} \tag{2.2}$$

where $\boldsymbol{I}_k$ is the (symmetric) kth-order identity tensor in d dimensions, and λ_d, μ_d denote Lame moduli endowing a plane-stress ($d=2$) or a three-dimensional problem ($d=3$). For future references, compressional c_{P} and shear wave c_{S} phase velocities are also defined as follows:

$$c_{\mathrm{P}}=\sqrt{\frac{\lambda_d+2\mu}{\rho}},\qquad c_{\mathrm{S}}=\sqrt{\frac{\mu}{\rho}}. \tag{2.3}$$

Note that the quiescent past condition in (2.1) can be alternatively imposed by requiring $\boldsymbol{u}(\cdot,0)=\dot{\boldsymbol{u}}(\cdot,0)=\mathbf{0}$. In the context of the present study, however, the format featured in (2.1) brings about the clarity of discussion that betters that of its substitute.

2.2 Inverse problem

With the above definitions, the inverse problem of cavity identification consists in reconstructing the topology and geometry of a hidden void, $B^{\mathrm{true}}\subset\Omega$, from a set of overdetermined data on the measurement part of the external boundary $S^{\mathrm{obs}}\subseteq S^{\mathrm{N}}$. To this end, the displacement field induced in $\overline{\Omega}\backslash B^{\mathrm{true}}$ by the boundary excitation $(\boldsymbol{u}^{\star},\boldsymbol{t}^{\star})$ is monitored over S^{obs} during time interval $[0,T]$, see Fig. 2.1a. On denoting the featured

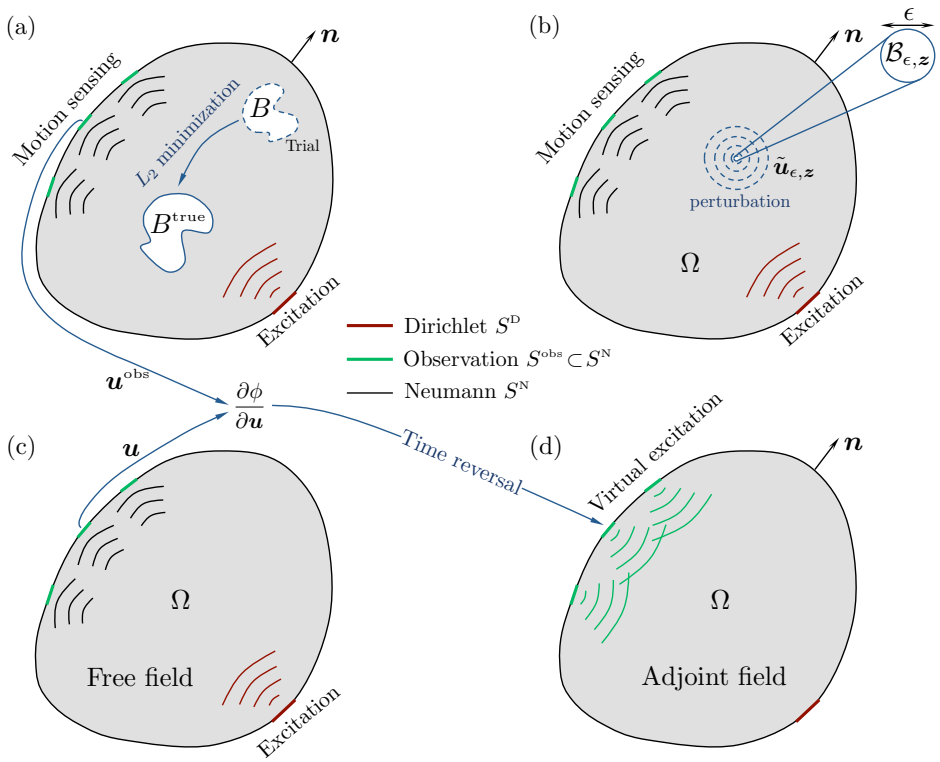

Figure 2.1: Elastodynamic defect reconstruction by way of TS: a) motion sensing in the cavitated domain $\overline{\Omega}\backslash B^{\text{true}}$ in the context of a minimization problem; b) scattering of the free field in the "punctured" domain $\Omega^{-}_{\epsilon,\boldsymbol{z}}$; c) free field in the reference domain Ω; d) adjoint field in Ω.

boundary measurements by $\boldsymbol{u}^{\text{obs}}$, the problem can be mathematically formulated as a task of minimizing the cost functional

$$\mathsf{J}(B) \;=\; \int_0^T \int_{S^{\text{obs}}} \phi[\boldsymbol{u}_{\text{B}}(\boldsymbol{\xi},t),\boldsymbol{\xi},t]\,\mathrm{d}S_\xi\,\mathrm{d}t, \tag{2.4}$$

where B is a trial void (that may be multiply connected); $\boldsymbol{u}_{\text{B}}$ solves (2.1), and ϕ is a misfit function that is hereon assumed to take the least squares format. To aid the ensuing developments, it is further convenient to introduce a non-negative windowing function $W(t)$ that is *compactly supported* over $[0,T]$ and to write

$$\phi[\boldsymbol{u}_{\text{B}}(\boldsymbol{\xi},t),\boldsymbol{\xi},t] \;=\; W(t)\,\tfrac{1}{2}\big\|\boldsymbol{u}_{\text{B}}(\boldsymbol{\xi},t)-\boldsymbol{u}^{\text{obs}}(\boldsymbol{\xi},t)\big\|^2 \qquad \text{on} \quad S^{\text{obs}}\times\mathbb{R}. \tag{2.5}$$

2.3 Topological sensitivity

Consider the perturbation of J with respect to the creation of a vanishingly small void $\mathcal{B}_{\epsilon,\boldsymbol{z}}$ of characteristic size ϵ at location $\boldsymbol{z} \in \Omega$ inside the reference, i.e. *defect-free* domain Ω as shown in Fig. 2.1b. Formally, the infinitesimal defect is specified by $\mathcal{B}_{\epsilon,\boldsymbol{z}} = \boldsymbol{z} + \epsilon\,\mathcal{B}$ where $\boldsymbol{z}$ is the sampling point, and $\mathcal{B} \subset \mathbb{R}^2$ is the prescribed "unit" shape (containing the origin) with boundary $\mathcal{S} = \partial\mathcal{B}$. For further reference, the open domain with a vanishing void is denoted by $\Omega^-_{\epsilon,\boldsymbol{z}} = \Omega \backslash \overline{\mathcal{B}}_{\epsilon,\boldsymbol{z}}$. As shown in [30], the leading asymptotic behavior of $\mathsf{J}(\mathcal{B}_{\epsilon,\boldsymbol{z}})$ as $\epsilon \to 0$ in the elastodynamic case when $\partial\mathcal{B}_{\epsilon,\boldsymbol{z}}$ is traction-free can be written as

$$\mathsf{J}(\mathcal{B}_{\epsilon,\boldsymbol{z}}) \;=\; \mathsf{J}(\emptyset) \;+\; \epsilon^d\,|\mathcal{B}|\,\mathsf{T}(\boldsymbol{z}) \;+\; o(\epsilon^2), \tag{2.6}$$

where $\mathsf{J}(\emptyset)$ signifies the cost functional (2.4) computed for the defect-free domain. Following the usual heuristic [17, 33], the void (or a system thereof) B^{true} is identified via regions where $\mathsf{T}(\boldsymbol{z};\cdot)$ attains pronounced negative values. For this reason, the latter is often referred to as an obstacle indicator function.

On decomposing the total elastodynamic field in the "punctured" solid as

$$\boldsymbol{u}_{\mathcal{B}_{\epsilon,\boldsymbol{z}}} \;=\; \boldsymbol{u} \,+\, \tilde{\boldsymbol{u}}_{\epsilon,\boldsymbol{z}} \qquad \text{on} \quad \overline{\Omega^-_{\epsilon,\boldsymbol{z}}} \times \mathbb{R}_{\text{T}} \tag{2.7}$$

where $\boldsymbol{u}_{\mathcal{B}_{\epsilon,\boldsymbol{z}}}$ solves (2.1) with $B = \mathcal{B}_{\epsilon,\boldsymbol{z}}$; $\boldsymbol{u}$ denotes the so-called *free field* solving (2.1) with $B = \emptyset$ (Fig. 2.1c), and $\tilde{\boldsymbol{u}}_{\epsilon,\boldsymbol{z}} = o(\epsilon^d)$ is the affiliated scattered field, one finds from (2.4)–(2.6) that

$$\mathsf{T}(\boldsymbol{z}) \;=\; \lim_{\epsilon\to 0}\, \frac{1}{\epsilon^d\,|\mathcal{B}|} \int_0^T \!\!\int_{S^{\text{obs}}} \frac{\partial\phi}{\partial\boldsymbol{u}}[\boldsymbol{u}(\boldsymbol{\xi},t),\boldsymbol{\xi},t] \cdot \tilde{\boldsymbol{u}}_{\epsilon,\boldsymbol{z}}(\boldsymbol{\xi},t)\,\mathrm{d}S_\xi\,\mathrm{d}t, \tag{2.8}$$

where

$$\frac{\partial\phi}{\partial\boldsymbol{u}}[\boldsymbol{u}(\boldsymbol{\xi},t),\boldsymbol{\xi},t] \;=\; W(t)\,[\boldsymbol{u} - \boldsymbol{u}^{\text{obs}}](\boldsymbol{\xi},t) \qquad \text{on} \quad S^{\text{obs}} \times \mathbb{R} \tag{2.9}$$

according to (2.5). Note that T is omitted from the list of arguments on the left-hand side of (2.8) for it is taken as a parameter. To obtain a compact representation of T, an auxiliary elastodynamic state $[\hat{\boldsymbol{u}}, \boldsymbol{\sigma}[\hat{\boldsymbol{u}}]]$ with quiescent past, termed the *adjoint state* [29],

see Fig. 2.1d, is introduced via

$$\begin{aligned}
\nabla\cdot\boldsymbol{\sigma}[\hat{\boldsymbol{u}}](\boldsymbol{\xi},t)-\rho\,\ddot{\hat{\boldsymbol{u}}}(\boldsymbol{\xi},t) &= \boldsymbol{0} && \text{on} \quad \Omega\times\mathbb{R}_{\mathrm{T}},\\
\boldsymbol{n}\cdot\boldsymbol{\sigma}[\hat{\boldsymbol{u}}](\boldsymbol{\xi},t) &= \tfrac{\partial\phi}{\partial\boldsymbol{u}}[\boldsymbol{u}(\boldsymbol{\xi},T-t),\boldsymbol{\xi},T-t] && \text{on} \quad S^{\mathrm{obs}}\times\mathbb{R}_{\mathrm{T}},\\
\boldsymbol{n}\cdot\boldsymbol{\sigma}[\hat{\boldsymbol{u}}](\boldsymbol{\xi},t) &= \boldsymbol{0} && \text{on} \quad S^{\mathrm{N}}\backslash S^{\mathrm{obs}}\times\mathbb{R}_{\mathrm{T}},\\
\hat{\boldsymbol{u}}(\boldsymbol{\xi},t) &= \boldsymbol{0} && \text{on} \quad S^{\mathrm{D}}\times\mathbb{R}_{\mathrm{T}},\\
\hat{\boldsymbol{u}}(\boldsymbol{\xi},t) &= \boldsymbol{0} && \text{on} \quad \Omega\times\mathbb{R}_{0}.
\end{aligned} \tag{2.10}$$

On deploying the Graffi's reciprocity identity in elastodynamics [44] for states with quiescent past over $\Omega^{-}_{\epsilon,\boldsymbol{z}}$ in terms of $\tilde{\boldsymbol{u}}_{\epsilon}$ and $\hat{\boldsymbol{u}}$, one finds that

$$\int\limits_{S\cup\partial\mathcal{B}_{\epsilon,\boldsymbol{z}}}\big(\boldsymbol{t}[\hat{\boldsymbol{u}}]*\tilde{\boldsymbol{u}}_{\epsilon,\boldsymbol{z}}-\boldsymbol{t}[\tilde{\boldsymbol{u}}_{\epsilon,\boldsymbol{z}}]*\hat{\boldsymbol{u}}\big)\,\mathrm{d}S_{\xi} \;=\; 0 \qquad \text{on} \quad \mathbb{R}, \tag{2.11}$$

where $\boldsymbol{t}[\hat{\boldsymbol{u}}]=\boldsymbol{n}\cdot\boldsymbol{\sigma}[\hat{\boldsymbol{u}}]$ is the surface traction, and

$$\boldsymbol{v}(\boldsymbol{\xi},t)*\boldsymbol{w}(\boldsymbol{\xi},t) \;=\; \big\{\boldsymbol{v}*\boldsymbol{w}\big\}(\boldsymbol{\xi},t) \;=\; \begin{cases} \int\limits_{0}^{t}\boldsymbol{v}(\boldsymbol{\xi},\tau)\cdot\boldsymbol{w}(\boldsymbol{\xi},t-\tau)\,\mathrm{d}\tau, & t\in(0,\infty)\\ 0, & t\in(-\infty,0] \end{cases} \tag{2.12}$$

denotes the temporal convolution of tensor fields $\boldsymbol{v}$ and $\boldsymbol{w}$. Note that the "dot" product in (2.12) signifies inner tensor contraction such that $\boldsymbol{v}\cdot\boldsymbol{w}$ is a *scalar* [29]. On the basis of (2.1) with $B=\mathcal{B}_{\epsilon,\boldsymbol{z}}$, (2.7), (2.10) and (2.11), one finds that

$$\mathsf{T}(\boldsymbol{z}) \;=\; \lim_{\epsilon\to 0}\frac{-1}{\epsilon^{d}\,|\mathcal{B}|}\int\limits_{\partial\mathcal{B}_{\epsilon,\boldsymbol{z}}}\big\{\boldsymbol{t}[\hat{\boldsymbol{u}}]*\tilde{\boldsymbol{u}}_{\epsilon,\boldsymbol{z}}+\boldsymbol{t}[\boldsymbol{u}]*\hat{\boldsymbol{u}}\big\}(\boldsymbol{\xi},T)\,\mathrm{d}S_{\xi} \tag{2.13}$$

which, upon performing the asymptotic analysis [29, 32] of the featured integral as $\epsilon\to 0$, yields

$$\mathsf{T}(\boldsymbol{z})=\big\{\boldsymbol{\sigma}[\hat{\boldsymbol{u}}]*(\mathcal{A}_{d}\!:\!\boldsymbol{\sigma}[\boldsymbol{u}])+\rho\,\dot{\hat{\boldsymbol{u}}}*\dot{\boldsymbol{u}}\big\}(\boldsymbol{z},T). \tag{2.14}$$

Here $\mathcal{A}_d$ denotes the (constant) fourth-order polarization tensor for a void with prescribed shape $\mathcal{B}$ in an unbounded solid $\mathbb{R}^d$ endowed with elastic tensor $\boldsymbol{C}$ (2.2). In this study, $\mathcal{B}$ is for simplicity taken as a unit circle ($d=2$), unit sphere ($d=3$), in which case

$$\begin{aligned}
\mathcal{A}_2 &= \frac{1}{\mu(1+\nu)}\Big[2\boldsymbol{I}_4-\frac{1-\nu+2\nu^2}{2(1-\nu^2)}\boldsymbol{I}_2\otimes\boldsymbol{I}_2\Big],\\
\mathcal{A}_3 &= \frac{3(1-\nu)}{2\mu(7-5\nu)}\Big[5\boldsymbol{I}_4-\frac{1+5\nu}{2(1+\nu)}\boldsymbol{I}_2\otimes\boldsymbol{I}_2\Big],
\end{aligned} \tag{2.15}$$

see e.g. [30, 33].

2.4 Choice of the misfit function ϕ

Formula (2.14), which compactly represents the TS in terms of two elastodynamic states computed for the reference domain Ω – the free field and the adjoint field, relies on the premise that $[\hat{\boldsymbol{u}}, \boldsymbol{\sigma}[\hat{\boldsymbol{u}}]]$ is an elastodynamic state *with quiescent past*. Referring again to the definition of an elastodynamic state as in [44, 45], this requirement in particular implies $\boldsymbol{\sigma}[\hat{\boldsymbol{u}}] \in C^0(\overline{\Omega} \times \mathbb{R}_{\mathrm{T}})$. On recalling that $\mathbb{R}_{\mathrm{T}} = (-\infty, T]$, one finds from (2.10) (and the fact that the free field $[\boldsymbol{u}, \boldsymbol{\sigma}[\boldsymbol{u}]]$ is an elastodynamic state with quiescent past) the consequent restriction on (2.9) as

$$\frac{\partial \phi}{\partial \boldsymbol{u}}[\boldsymbol{u}(\boldsymbol{\xi}, t), \boldsymbol{\xi}, t] \; \in \; C^0(S^{\mathrm{obs}} \times [0, \infty)). \tag{2.16}$$

If the misfit function (2.5) is left "unmodulated" as in a number of previous studies [29, 33, 32] which, in the context of the present study, translates into a rectangular window function

$$W(t) \; = \; \begin{cases} 1, & t \in [0, T], \\ 0, & t \notin [0, T], \end{cases} \tag{2.17}$$

(2.16) requires that

$$\frac{\partial \phi}{\partial \boldsymbol{u}}[\boldsymbol{u}(\boldsymbol{\xi}, T), \boldsymbol{\xi}, T] \; = \; \mathbf{0} \qquad \text{on} \quad S^{\mathrm{obs}}. \tag{2.18}$$

For unbounded reference domains, (2.18) can be met by taking T to be sufficiently large thanks to the radiation condition [45]. Unfortunately (2.18) is practically never satisfied in *finite* elastic bodies, regardless of T, owing to the utter absence of dissipation mechanisms. In this regard, one may note that even if the definition of an elastodynamic state was relaxed to allow for the stress fields that are discontinuous in time, the violation of (2.18) and thus (2.16) poses a fundamental challenge in terms of the customary computational (e.g. finite element or finite difference) treatments, see Sec. 4.2 for further details.

The simplest way of meeting (2.18) for finite elastic bodies, that are of interest in this study, is to select a windowing function $W \in C^0(\mathbb{R})$ that is compactly supported over $[0, T]$. This approach forms the basis for the ensuing developments and will be detailed in the sequel.

For completeness, however, it is of interest to expose the structure of the TS under the premise of a rectangular windowing function (2.17). In this case, (2.5) can be conveniently decomposed as

$$\phi[\boldsymbol{u}(\boldsymbol{\xi},t),\boldsymbol{\xi},t] \;=\; \varphi[\boldsymbol{u}(\boldsymbol{\xi},t),\boldsymbol{\xi},t] \,+\, \phi[\boldsymbol{u}(\boldsymbol{\xi},T),\boldsymbol{\xi},T], \tag{2.19}$$

where $\partial\varphi/\partial\boldsymbol{u}$ clearly satisfies the continuity requirement (2.16). Accordingly, the TS takes the form

$$\mathsf{T}(\boldsymbol{z}) = \big\{\boldsymbol{\sigma}[\hat{\boldsymbol{u}}']*(\mathcal{A}_d\!:\!\boldsymbol{\sigma}[\boldsymbol{u}])+\rho\,\dot{\hat{\boldsymbol{u}}}'*\dot{\boldsymbol{u}}\big\}(\boldsymbol{z},T) + \int\limits_{S^{\rm obs}} \Big\{\frac{\partial\phi}{\partial\boldsymbol{u}}[\boldsymbol{u}(\boldsymbol{\xi},T),\boldsymbol{\xi},T]\cdot\int\limits_0^T \lim_{\epsilon\to 0}\,\frac{\tilde{\boldsymbol{u}}_{\epsilon,\boldsymbol{z}}(\boldsymbol{\xi},t)}{\epsilon^d\,|\mathcal{B}|}\,\mathrm{d}t\Big\}\mathrm{d}S_\xi, \tag{2.20}$$

where the adjoint field $\hat{\boldsymbol{u}}'$ solves (2.10) with $\phi=\varphi$. On adopting the integral equation approach as in e.g. [32], the limit featured in (2.20) can be formally written as

$$\lim_{\epsilon\to 0}\,\frac{\tilde{\boldsymbol{u}}_{\epsilon,\boldsymbol{z}}(\boldsymbol{\xi},t)}{\epsilon^d\,|\mathcal{B}|} \;=\; \sum_{k=1}^{d}\boldsymbol{e}_k\Big\{\boldsymbol{\sigma}[\boldsymbol{U}^k](\boldsymbol{z},\boldsymbol{\xi},t)*(\mathcal{A}_d\!:\!\boldsymbol{\sigma}[\boldsymbol{u}](\boldsymbol{z},t))+\rho\,\dot{\boldsymbol{U}}^k(\boldsymbol{z},\boldsymbol{\xi},t)*\dot{\boldsymbol{u}}(\boldsymbol{z},t)\Big\}, \qquad \boldsymbol{z}\in\Omega \tag{2.21}$$

where $\boldsymbol{e}_k$ ($k=\overline{1,d}$) is the unit vector in the kth (Cartesian) coordinate direction, and $\boldsymbol{U}^k(\boldsymbol{z},\boldsymbol{\xi},t)$ signifies the elastodynamic Green's function for the reference body Ω due to time-impulsive point load $\boldsymbol{e}_k\delta(t)\delta(\boldsymbol{z}-\boldsymbol{\xi})$ acting at $\boldsymbol{\xi}\in\Omega$ in direction k. With the aid of (2.21), the second entry of (2.20) can be further simplified; for instance, one can show on the basis of the $C^2[0,\infty)$ continuity in time of $\boldsymbol{U}^k(\boldsymbol{z},\boldsymbol{\xi},t)$ and $\boldsymbol{u}(\boldsymbol{z},t)$ for $\Omega\ni\boldsymbol{z}\neq\boldsymbol{\xi}$, the properties [44] of the convolution operator (2.12), and the boundary integral representation of an elastodynamic field in Ω that

$$\begin{aligned}
&\int\limits_{S^{\rm obs}}\Big\{\frac{\partial\phi}{\partial\boldsymbol{u}}[\boldsymbol{u}(\boldsymbol{\xi},T),\boldsymbol{\xi},T]\cdot\int\limits_0^T\sum_{k=1}^{d}\rho\,\boldsymbol{e}_k\,\dot{\boldsymbol{U}}^k(\boldsymbol{z},\boldsymbol{\xi},t)*\dot{\boldsymbol{u}}(\boldsymbol{z},t)\,\mathrm{d}t\Big\}\mathrm{d}S_\xi \;=\\
&\int\limits_{S^{\rm obs}}\Big\{\frac{\partial\phi}{\partial\boldsymbol{u}}[\boldsymbol{u}(\boldsymbol{\xi},T),\boldsymbol{\xi},T]\cdot\sum_{k=1}^{d}\rho\,\boldsymbol{e}_k\,\boldsymbol{U}^k(\boldsymbol{z},\boldsymbol{\xi},T)*\dot{\boldsymbol{u}}(\boldsymbol{z},T)\Big\}\mathrm{d}S_\xi \;=\; \rho\sum_{k=1}^{d}\boldsymbol{e}_k\cdot\boldsymbol{w}^k(\boldsymbol{z},T),
\end{aligned} \tag{2.22}$$

where $[\boldsymbol{w}^k, \boldsymbol{\sigma}[\boldsymbol{w}^k]]$, $k=\overline{1,d}$ are the elastodynamic states solving

$$\begin{aligned}
\nabla\cdot\boldsymbol{\sigma}[\boldsymbol{w}^k](\boldsymbol{\xi},t) &= \mathbf{0} && \text{on} \quad \Omega,\\
\boldsymbol{n}\cdot\boldsymbol{\sigma}[\boldsymbol{w}^k](\boldsymbol{\xi},t) &= \tfrac{\partial\phi}{\partial\boldsymbol{u}}[\boldsymbol{u}(\boldsymbol{\xi},T),\boldsymbol{\xi},T]\,\dot{u}_k(\boldsymbol{z},t) && \text{on} \quad S^{\text{obs}},\\
\boldsymbol{n}\cdot\boldsymbol{\sigma}[\boldsymbol{w}^k](\boldsymbol{\xi},t) &= \mathbf{0} && \text{on} \quad S^{\text{N}}\backslash S^{\text{obs}},\\
\boldsymbol{w}^k(\boldsymbol{\xi},t) &= \mathbf{0} && \text{on} \quad S^{\text{D}}.
\end{aligned} \tag{2.23}$$

Here $\dot{u}_k=\dot{\boldsymbol{u}}\cdot\boldsymbol{e}_k$ is the kth component of the free-field particle velocity vector $\dot{\boldsymbol{u}}$, whereby the prescribed boundary traction in (2.23) reads

$$\frac{\partial\phi}{\partial\boldsymbol{u}}[\boldsymbol{u}(\boldsymbol{\xi},T),\boldsymbol{\xi},T]\,\dot{u}_k(\boldsymbol{z},t) \;=\; (\boldsymbol{u}-\boldsymbol{u}^{\text{obs}})(\boldsymbol{\xi},T)\,\dot{u}_k(\boldsymbol{z},t) \;\in C^0(S^{\text{obs}}\times\mathbb{R}_{\text{T}}), \qquad \boldsymbol{z}\in\Omega.$$

From (2.21)–(2.23), it is clear that the integral in (2.20) entails evaluation of additional elastodynamic states with sampling-point-dependent excitation, which renders the use of rectangular windowing function (2.17) impractical from both analytical and computational point of view.

2.5 TS formulation in terms of particle velocity observations

In situations where the sensing is effected with the aid of a velocity measurement equipment, such as the one employed in this study (see Sec. 3), numerical integration is commonly deployed to compute the affiliated displacement data. Alternatively, the cost functional (2.5) and TS formula (2.14) can be recast in terms of the *velocity* input data. In practical terms, such rearrangement may simplify data interpretation as it allows one to avoid numerical integration and affiliated filtering of the LDV records. To investigate the latter possibility, consider the velocity-based counterpart of (2.5), namely

$$\phi[\dot{\boldsymbol{u}}_{\text{B}}(\boldsymbol{\xi},t),\boldsymbol{\xi},t] \;=\; W(t)\,\tfrac{1}{2}\big\|\dot{\boldsymbol{u}}_{\text{B}}(\boldsymbol{\xi},t)-\dot{\boldsymbol{u}}^{\text{obs}}(\boldsymbol{\xi},t)\big\|^2 \qquad \text{on} \quad S^{\text{obs}}\times\mathbb{R}. \tag{2.24}$$

On substituting (2.24) in (2.4) and (2.6), one finds by following the developments in Sec. **??** that

$$\mathsf{T}(\boldsymbol{z}) \;=\; \lim_{\epsilon\to 0}\frac{1}{\epsilon^2\,|\mathcal{B}|}\int_0^T\!\!\int_{S^{\text{obs}}}\frac{\partial\phi}{\partial\dot{\boldsymbol{u}}}[\dot{\boldsymbol{u}}(\boldsymbol{\xi},t),\boldsymbol{\xi},t]\cdot\dot{\tilde{\boldsymbol{u}}}_{\epsilon,\boldsymbol{z}}(\boldsymbol{\xi},t)\,\mathrm{d}S_\xi\,\mathrm{d}t. \tag{2.25}$$

By analogy to (2.10), an auxiliary elastodynamic state $[\check{\boldsymbol{u}}, \boldsymbol{\sigma}[\check{\boldsymbol{u}}]]$ with quiescent past is introduced via

$$\begin{aligned}
\nabla\cdot\boldsymbol{\sigma}[\check{\boldsymbol{u}}](\boldsymbol{\xi},t) - \rho\,\ddot{\check{\boldsymbol{u}}}(\boldsymbol{\xi},t) &= \boldsymbol{0} && \text{on} \quad \Omega\times\mathbb{R}_{\mathrm{T}},\\
\boldsymbol{n}\cdot\boldsymbol{\sigma}[\check{\boldsymbol{u}}](\boldsymbol{\xi},t) &= \tfrac{\partial\phi}{\partial\dot{\boldsymbol{u}}}[\dot{\boldsymbol{u}}(\boldsymbol{\xi},T-t),\boldsymbol{\xi},T-t] && \text{on} \quad S^{\mathrm{obs}}\times\mathbb{R}_{\mathrm{T}},\\
\boldsymbol{n}\cdot\boldsymbol{\sigma}[\check{\boldsymbol{u}}](\boldsymbol{\xi},t) &= \boldsymbol{0} && \text{on} \quad S^{\mathrm{N}}\backslash S^{\mathrm{obs}}\times\mathbb{R}_{\mathrm{T}},\\
\check{\boldsymbol{u}}(\boldsymbol{\xi},t) &= \boldsymbol{0} && \text{on} \quad S^{\mathrm{D}}\times\mathbb{R}_{\mathrm{T}},\\
\check{\boldsymbol{u}}(\boldsymbol{\xi},t) &= \boldsymbol{0} && \text{on} \quad \Omega\times\mathbb{R}_{0}.
\end{aligned} \tag{2.26}$$

On differentiating the Graffi's reciprocity identity in elastodynamics [44] for states with quiescent past over $\Omega^{-}_{\epsilon,\boldsymbol{z}}$ in terms of $\tilde{\boldsymbol{u}}_{\epsilon}$ and $\check{\boldsymbol{u}}$, namely

$$\frac{\mathrm{d}}{\mathrm{d}t}\int\limits_{S\cup\partial\mathcal{B}_{\epsilon,\boldsymbol{z}}}\big(\boldsymbol{t}[\check{\boldsymbol{u}}]*\tilde{\boldsymbol{u}}_{\epsilon,\boldsymbol{z}}-\boldsymbol{t}[\tilde{\boldsymbol{u}}_{\epsilon,\boldsymbol{z}}]*\check{\boldsymbol{u}}\big)\,\mathrm{d}S_{\xi} = 0 \qquad \text{on} \quad \mathbb{R},$$

and deploying the property of the convolution operator

$$\frac{\mathrm{d}}{\mathrm{d}t}\big\{\boldsymbol{a}*\boldsymbol{b}\big\} = \big\{\dot{\boldsymbol{a}}*\boldsymbol{b}\big\} = \big\{\boldsymbol{a}*\dot{\boldsymbol{b}}\big\}$$

together with the time-invariance of $\boldsymbol{C}$, one finds

$$\mathsf{T}(\boldsymbol{z}) = \lim_{\epsilon\to 0}\frac{-1}{\epsilon^{2}\,|\mathcal{B}|}\int\limits_{\partial\mathcal{B}_{\epsilon,\boldsymbol{z}}}\big\{\boldsymbol{t}[\check{\boldsymbol{u}}]*\dot{\tilde{\boldsymbol{u}}}_{\epsilon,\boldsymbol{z}}+\boldsymbol{t}[\dot{\boldsymbol{u}}]*\check{\boldsymbol{u}}\big\}(\boldsymbol{\xi},T)\,\mathrm{d}S_{\xi}. \tag{2.27}$$

Proceeding with the asymptotic analysis of (2.27) as in [29], it can further be shown that

$$\mathsf{T}(\boldsymbol{z}) = \big\{\boldsymbol{\sigma}[\check{\boldsymbol{u}}]*(\mathcal{A}\!:\!\boldsymbol{\sigma}[\dot{\boldsymbol{u}}])+\rho\,\dot{\check{\boldsymbol{u}}}*\ddot{\boldsymbol{u}}\big\}(\boldsymbol{z},T). \tag{2.28}$$

Inherently, (2.29) requires that the free field $\boldsymbol{u}$ and thus the boundary conditions in (2.1) meet more restrictive smoothness requirements in that $\boldsymbol{u}^{\star}\in C^{1}(S^{\mathrm{D}})\times C^{2}(\mathbb{R}_{\mathrm{T}})$ and $\boldsymbol{t}^{\star}\in C^{0}(S^{\mathrm{N}})\times C^{1}(\mathbb{R}_{\mathrm{T}})$. Under such hypothesis, one can formally rewrite (2.27) in terms of $\boldsymbol{v}\equiv\dot{\boldsymbol{u}}$ and $\check{\boldsymbol{u}}$ as

$$\mathsf{T}(\boldsymbol{z}) = \big\{\boldsymbol{\sigma}[\check{\boldsymbol{u}}]*(\mathcal{A}\!:\!\boldsymbol{\sigma}[\boldsymbol{v}])+\rho\,\dot{\check{\boldsymbol{u}}}*\dot{\boldsymbol{v}}\big\}(\boldsymbol{z},T), \tag{2.29}$$

where the elastodynamic state $[\boldsymbol{v},\boldsymbol{\sigma}[\boldsymbol{v}]]$ is defined by

$$\begin{aligned}
\nabla\cdot\boldsymbol{\sigma}[\boldsymbol{v}](\boldsymbol{\xi},t) - \rho\,\ddot{\boldsymbol{v}}(\boldsymbol{\xi},t) &= \boldsymbol{0} && \text{on} \quad \Omega\times\mathbb{R}_{\mathrm{T}},\\
\boldsymbol{n}\cdot\boldsymbol{\sigma}[\boldsymbol{v}](\boldsymbol{\xi},t) &= \dot{\boldsymbol{t}}^{\star} && \text{on} \quad S^{\mathrm{N}}\times\mathbb{R}_{\mathrm{T}},\\
\boldsymbol{v}(\boldsymbol{\xi},t) &= \dot{\boldsymbol{u}}^{\star} && \text{on} \quad S^{\mathrm{D}}\times\mathbb{R}_{\mathrm{T}},\\
\boldsymbol{v}(\boldsymbol{\xi},t) &= \boldsymbol{0} && \text{on} \quad \Omega^{-}\times\mathbb{R}_{0}.
\end{aligned} \tag{2.30}$$

Chapter 3

Data acquisition and implementation of the SLDV testing system

This chapter briefly describes the principles and operation of the 3D Scanning Laser Doppler Vibrometer (SLDV) motion sensing apparatus that is employed in this study for acquiring the sensory data. A particular case of low impact excitation is considered and an insight is given towards improving the accuracy of SLDV sensing, in particular as it pertains to the tangential components of surface motion.

3.1 Principle of 3D SLDV data acquisition

Surface motion sensing is effected in a non-contact way via an SLDV system PSV-400-3D by Polytec, Inc. By deploying the principles of optical Doppler effect and three independent scanning heads targeting a material point from different angles as shown in Fig. 3.1, the system is capable of capturing the normal and in-plane velocity components of the surface motion over a prescribed grid of points with the spatial resolution better than 0.1 mm. In the experiment, the scan heads are positioned at stand-off distance of roughly 50-100 cm from the center of the object such that all scan points can be reached by each unit with the deflection angle (i.e. the angle between the laser beam

and the axis of the scan head) less than 20 degrees, see display (c). The system further utilizes an inverse coordinate transform to convert the velocity signal $\tilde{\boldsymbol{v}} = \tilde{v}_i\, \tilde{\boldsymbol{e}}_i$, $i = \overline{1,3}$, obtained at each scan point in the laser beams frame (see display (b)) to a cartesian frame $\boldsymbol{v} = v_i\, \boldsymbol{e}_i$, such that:

$$\tilde{\boldsymbol{v}} = \mathrm{A}(\boldsymbol{\phi})\boldsymbol{v}, \tag{3.1}$$

where $\mathrm{A}(\boldsymbol{\phi})$ is a cosine matrix of basis $\{\tilde{\boldsymbol{e}}_i\}_{i=1}^{3}$ and $\boldsymbol{\phi} = (\phi_{1\mathrm{h}}, \phi_{1\mathrm{v}}, \phi_{2\mathrm{h}}, \phi_{2\mathrm{v}}, \phi_{3\mathrm{h}}, \phi_{3\mathrm{v}})$ denotes six degrees of freedom in the SLDV coordinate space, i.e. angles of rotation of the scanning mirrors with two angles per head (actuating horizontal (h) and vertical (v) movement of the laser beam), see display (c). Matrix A is obtained in a procedure called 3D alignment that utilizes nonlinear interpolation to calculate the mapping $\boldsymbol{\phi} \to \mathrm{A}(\boldsymbol{\phi})$ from a set of prescribed reference points. The latter can be assigned with the aid of the manufacturer-provided 3D geometry reference object, or integrated into one of the scan heads rangefinder device (geometry scan unit) that measures distances via the laser beam time-of-flight measurements. Given scan points lying on the plane (e.g., edge of a 3D block), a sufficient accuracy of the 3D alignment is reached with 4 reference points located in the farthest corners of the scan points area and at least one more reference point set along the normal to the plane, about 15-30 cm toward the scan heads.

3.2 Physical excitation

Dynamic excitation of the specimens is provided via either a 32 mm-diameter 0.5 MHz (Olympus V101), or a 16 mm-diameter 1.0 MHz (Olympus V103) contact piezoceramic compressional (P-) wave transducer attached to the surface of the specimen via cyanoacrylate glue, see Fig. 3.2. The 0.5 MHz transducer is employed to excite 2D specimen (plates); attached such that its axis lies approximately in the mid-plane of a plate, see display (a), it generates mostly in-plane motion. The 1.0 MHz transducer is used to excite 3D specimens (blocks); attached to the transducer's contact patch is a circular transfer rod with a cross-section reduction from 16 mm to 6 mm (see display (b)) that enables to concentrate excitation energy on a smaller area thus reducing an uncertainty in specifying excitation boundary condition in the elastodynamic model as detailed later.

The transducer is excited via internal random signal generator, the excitation wavelet

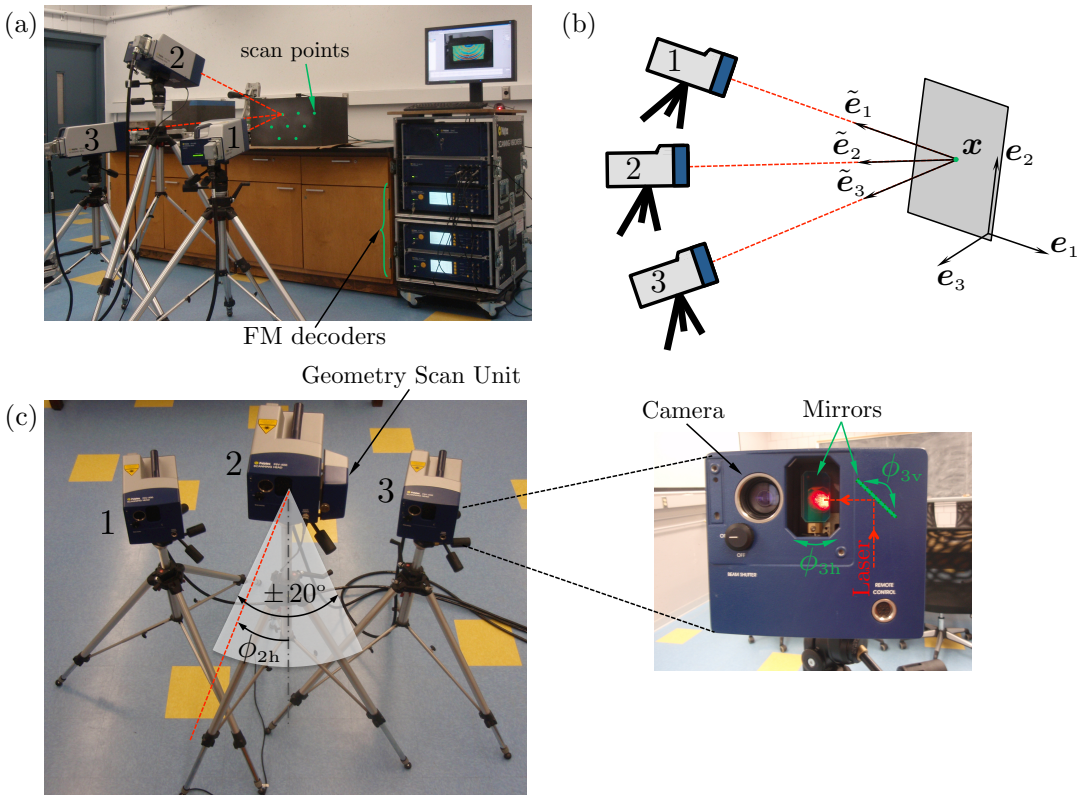

Figure 3.1: 3D data acquisition via SLDV: a) SLDV setup with scan heads set on floor tripods; b) laser beams in a cartesian frame; c) mirror-activated movement of the laser beam.

is taken as a modulated 5-cycle burst

$$s(t) \;=\; \begin{cases} \sin\left(\frac{\pi f_c}{5}\,t\right)\,\sin\left(2\pi f_c t\right), & t \leqslant 5/f_c \\ 0, & t > 5/f_c \end{cases} \tag{3.2}$$

shown in Fig. 3.3, with carrier i.e. "center" frequency f_c. To investigate the effect of the rate of excitation on the quality and spatial resolution of TS defect reconstruction in the experimental setting, f_c was subsequently set to 10, 20, 30, and 40 kHz, giving rise to the illuminating wavefields with p-wave wavelengths of several centimeters. However, due to pronounced resonance-type behavior of the piezotransducers, the impact displacement of the transducers at these frequencies is at the order of *tens of nm*, which poses a challenge in terms of 3D SLDV motion sensing.

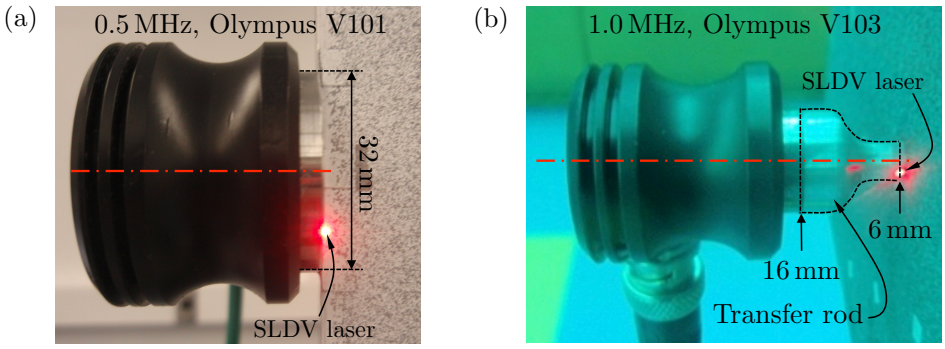

Figure 3.2: Piezoceramic P-wave transducers by Olympus employed for dynamic excitation: 0.5 MHz, 1″ (a), and 1 MHz, 0.5″ (b).

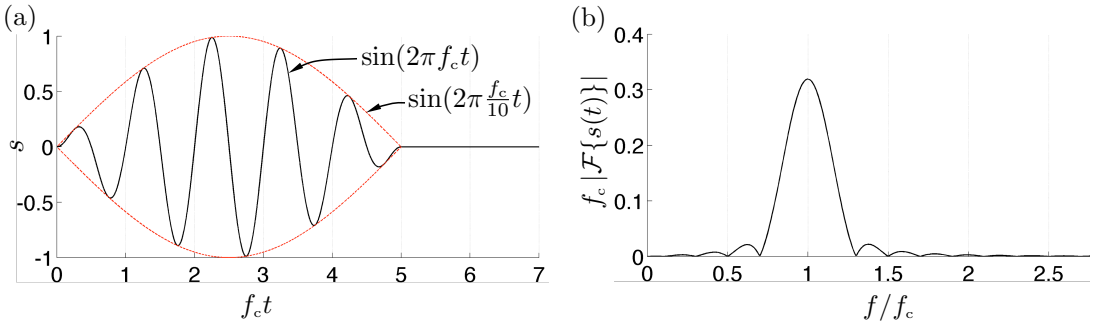

Figure 3.3: Excitation wavelet $s(t)$ with carrier frequency f_c: time domain (a), and amplitude frequency spectrum (b).

3.3 Directional sensitivity of SLDV

From the preliminary experiments it was noticed that the out-of-plane component of the velocity time signal (v_3 in Fig. 3.1(b)) is generally characterized by considerably better signal-to-noise ratio (SNR) compared to the in-plane components – which is a consequence of enhanced out-of-plane/poor in-plane directional sensitivity of the scan heads setup. In other words, in a typical setup the lasers are more sensitive to the out-of-plane component of motion since this is a dominant direction of the beams hitting the surface, see the display. Choosing more efficient setup can be established using the properties of the alignment matrix A – which must be well-conditioned to facilitate accurate inversion of system (3.1). In other words, given the uncertainty (any kind of noise) in the recorded signals $\tilde{\boldsymbol{v}}$ it is desired to minimize the uncertainty in the solution

$\boldsymbol{v}=\mathrm{A}^{-1}\tilde{\boldsymbol{v}}$. The latter is controlled by condition number $\kappa(\mathrm{A})$ of A that is defined in the sense of square-summable sequence space ℓ^2:

$$\kappa(\mathrm{A}) = \frac{\sigma_{\max}(\mathrm{A})}{\sigma_{\min}(\mathrm{A})}, \tag{3.3}$$

where $\sigma_{\max}(\mathrm{A})$, $\sigma_{\min}(\mathrm{A})$ denote respectively the maximum and the minimum eigenvalues of A. For a given Cartesian frame $\{\boldsymbol{e}_i\}_{i=1}^3$ and location $\boldsymbol{x}$ of the scan point, minimizing $\kappa(\mathrm{A})$ with respect to directions $\tilde{\boldsymbol{e}}_i$, $i=\overline{1,3}$ yields an optimal configuration of the scan heads. Tackling a general minimization problem is beyond the scope of this study, however an insight could be obtained from a simple numerical example, shown in Fig. 3.4. In this case a simplified geometry is assumed in which the scan heads are arranged in the vertices of an equilateral triangle inscribed in a circle of radius r while the scan point is located on the centroid of this triangle at distance h, see left panel on the figure. Shown on the right panel is numerically calculated $\kappa(\mathrm{A})$ as a function of parameters h and r. As can be seen from the display, the condition number of A is minimized (equals to 1) in r–h plane on the line $h=r/\sqrt{2}$ which corresponds to the case when $\{\tilde{\boldsymbol{e}}\}_{i=1}^3$ forms an alternative Cartesian basis, i.e. the lasers converge at right angles with respect to each other. In this particular case, A is nothing else but a 3D rotation matrix whose determinant and condition number are both unity. This conclusion provides a rule of thumb as to how to set the distance h from the laser heads to the object in order to improve the sensitivity of the measurements of the in-plane components. For completeness, the figure also demonstrates that if distance h is increased twice, $h=r\sqrt{2}$, i.e. the condition number is increased twice as well – which can considerably degrade the SNR of the in-plane velocity measurements in case of sensing low-amplitude motion as observed in the experiment.

3.4 SLDV sensing of low-amplitude motion

In case of relatively high SNR, the directional sensitivity of 3D SLDV might be of little concern; however, as pointed out in Section 3.2, this study deals with extremely low amplitude vibrations such that any noise multiplication might cause significant reduction of the SNR. In the absence of a special robotic arm by Polytec designed to automatically move the scan heads, readjusting the arrangement of the scan heads at each scan point

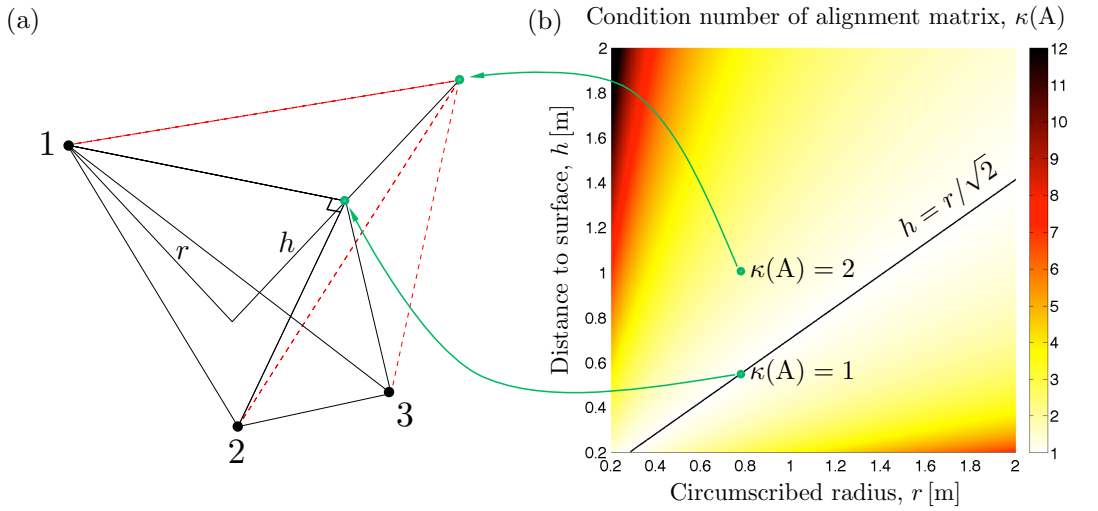

Figure 3.4: Directional sensitivity of 3D SLDV: a) laser heads and a scan point arranged in the vertices of a regular pyramid; b) condition number of the alignment matrix plot as a function of r and h.

in the sense of Fig. 3.4a for best measurement is too laborious and rather defies the concept of automatic scanning. Therefore, if both in-plane and out-of-plane components of the motion are to be acquired in the experiment, the preferable permanent location of the scan heads is such that the condition number of the alignment matrix does not become much larger than unity within the range of all scan points. Unfortunately, the available acquisition software by Polytec does not provide this information during the alignment procedure, only through an auxiliary Visual Basic script one can retrieve the coordinates of the scan heads to calculate the corresponding alignment matrix at a given scan point. Moreover, one often has to sacrifice the directional sensitivity to comply with the required arrangement of the scan points on the object within a single SLDV setup, see Fig. 3.1(c). In this vein, an effort is made to minimize the effect of random noise in the system (both optical and mechanical) through: (i) signal stacking over an ensemble of at least 50 realizations at each scan point, and (ii) surface enhancement via retroreflective tape by 3M. In this setting, the transducer is excited in periodically such that between the excitation bursts a large period of relaxation time is allowed until all waves in the specimen attenuate to zero while the recorded velocity signals are averaged over an ensemble of the stack, see Fig. 3.5. Decoding the raw Doppler signals is performed using a built-in velocity decoder VD-03 with the sensitivity and sampling

frequency F_s set respectively at 10 mm/s·V and 2.56 MHz. At these settings, the velocity resolution of the SLDV system in the absence of mechanical and optical noise is approximately 300 μm/s (assuming no stacking) for frequencies below 100 kHz, and the amplitude error is ± 0.1 dB at 1 kHz. All internal filters, both analog and digital, were disabled to minimize phase-related errors in the observed surface motion.

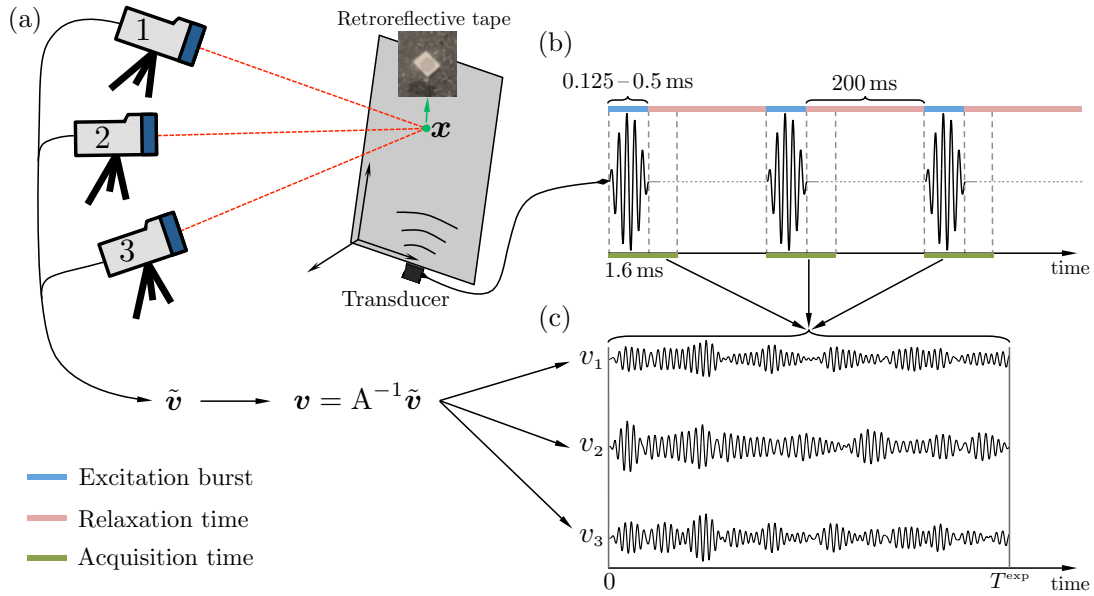

Figure 3.5: Measurement at a single scan point: a) SLDV setup; b) excitation signal fed to the transducer; c) velocity signals in cartesian frame averaged over several realizations.

3.5 SLDV-TS experimental setup and procedure

This section describes the experimental setups employed for testing: (i) thin aluminum plate in a demonstrative 2D defect reconstruction problem, (ii) similar setup for a thin graphite plate, and (iii) graphite block in a "realistic" 3D configuration with a *limited aperture* of illuminating sources/motion sensors.

3.5.1 Aluminum plate

A square plate made of T6061-T6 aluminum alloy, with thickness $d = 8\,\text{mm}$ and side length $\ell = 993\,\text{mm}$, is used as the "reference" domain. The alloy is characterized by the Young's modulus $E = 69\,\text{GPa}$, Poisson's ratio $\nu = 0.33$, and mass density $\rho = 2700\,\text{kg/m}^3$. The plate is kept in the upright position via two slotted bar supports (hereon referred to as the "legs"), affixed to its bottom corners, see Fig. 3.6a.

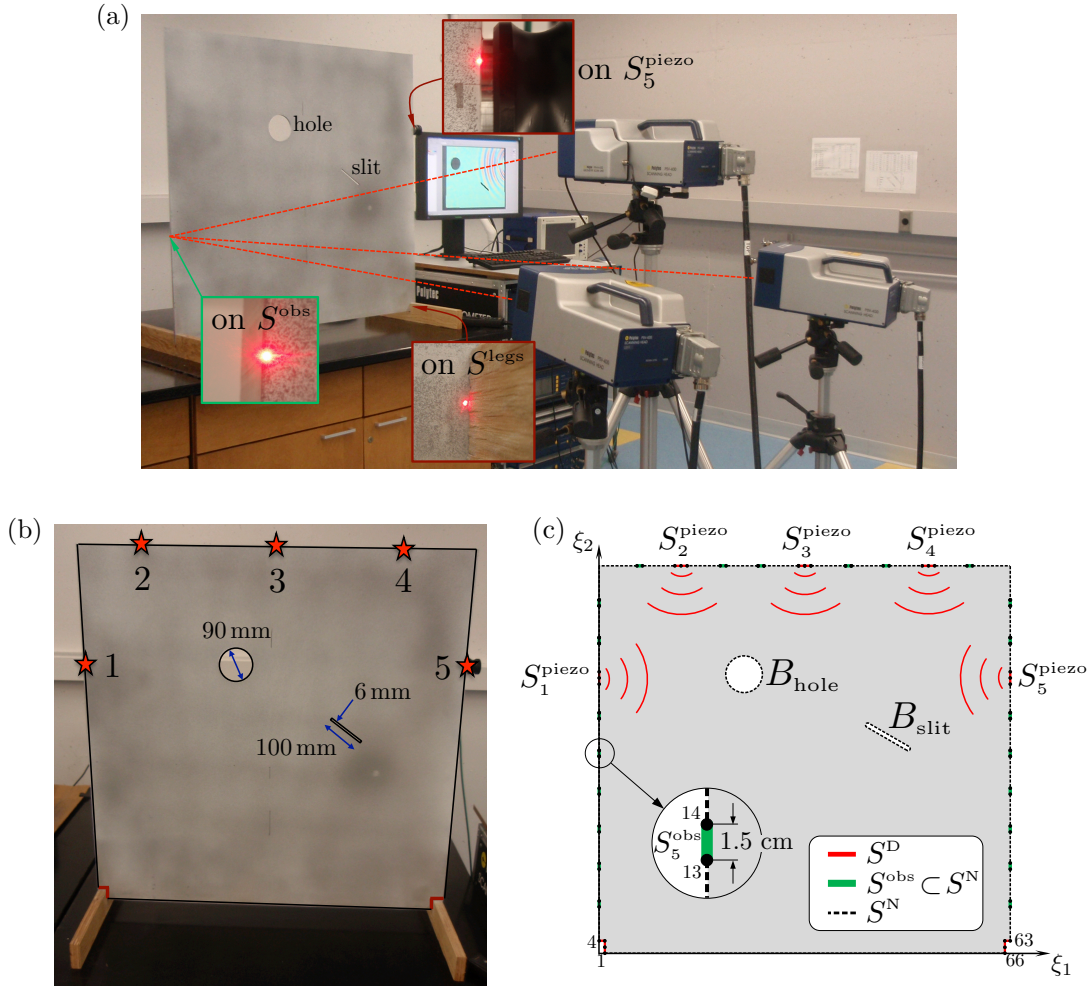

Figure 3.6: Aluminum plate experimental setup: a) measurement of the Dirichlet/observations data by way of SLDV; b) 5 transducer locations employed to illuminate both defects B_{hole} and B_{slit}; c) SLDV scan points spatial arrangement.

In this setting, an elastodynamic state generated in the plate can be approximated by way of the *plane stress* assumption [46] provided that the frequency content of the propagating waves is such that the dominant observed wavelength, λ, is significantly larger than the plate thickness d. On deploying the thin-plate model as in [47, 48], one finds from (2.3) the compressional (P-) and shear (S-) wave speeds in the plate as

$$c_{\mathrm{P}} = \sqrt{\frac{E}{(1-\nu^2)\rho}} \simeq 5355\tfrac{\mathrm{m}}{\mathrm{sec}}, \qquad c_{\mathrm{S}} = \sqrt{\frac{E}{2(1+\nu)\rho}} \simeq 3100\tfrac{\mathrm{m}}{\mathrm{sec}}. \tag{3.4}$$

With reference to (2.3), it is hereon assumed that the plane stress hypothesis is met with sufficient accuracy as long as $\lambda_{\mathrm{S}} = c_{\mathrm{S}}/f_{\mathrm{c}} > 9d$, where f_{c} is the dominant i.e. "center" frequency of the prescribed excitation wavelet. In the context of the Lamb's analysis [47] this particular threshold implies, assuming $\nu = 0.33$, that the error committed by approximating $c_{\mathrm{S}}(f)$ by its zero-frequency limit as in (2.3) is less than 0.7%. Accordingly, the ensuing experiments and data analysis are performed under the restriction $f_{\mathrm{c}} < c_{\mathrm{S}}/(9d) \simeq 43\,\mathrm{kHz}$.

For reconstruction purposes, two "defects" were machined in the plate: a 90 mm-diameter circular hole, and a 100 mm × 6 mm rectangular slit with rounded edges, see Fig. 3.6a. The damaged domain $\Omega \backslash \overline{B}^{\mathrm{true}}$ is shown schematically in Fig. 3.6c, where $B^{\mathrm{true}} = B_{\mathrm{hole}} \cup B_{\mathrm{slit}}$. As shown in a number of previous studies by way of numerical simulations, the performance of TS-based defect reconstruction is strongly affected by the apertures of both source and observation grids. In particular, each of the two grids should maximize the solid angle around the (expected) damaged region to make the best use of a fixed number of experimental measurements. In this vein, the testing configuration adopted in the present study consists of five source segments S_k^{piezo}, $k = \overline{1,5}$, and 22 observation segments S_j^{obs}, $j = \overline{1,22}$, as shown in Fig. 3.6c. For the kth source location, the induced elastodynamic wavefield is monitored (in terms of in-plane velocity components $\dot{\boldsymbol{u}}^{\mathrm{obs}}$) over 66 SLDV scan points distributed over the left, upper, and right edge of the plate. Here the measurements from scan points 1–4, 63–66, and the points belonging to S_k^{piezo} are used to impose (linearly interpolated) Dirichlet data on $S^{\mathrm{D}} = S_k^{\mathrm{piezo}} \cup S^{\mathrm{legs}}$, while the remainder are deployed to provide the sensory data $\boldsymbol{u}^{\mathrm{obs}}$ on S^{obs}. In the experiment, the 0.5 MHz transducer (Fig. 3.2a) is first placed at S_1^{piezo} to illuminate the damaged area "from the left"; the SLDV motion sensing is then performed at all scan points providing both excitation and observations data. The data

thus obtained ($\boldsymbol{u}^*$ and $\boldsymbol{u}^{\text{obs}}$) are then used to compute the free and adjoint elastodynamic states $[\boldsymbol{u}, \boldsymbol{\sigma}[\boldsymbol{u}]]$ and $[\hat{\boldsymbol{u}}, \boldsymbol{\sigma}[\hat{\boldsymbol{u}}]]$, whose bilinear form (2.14) gives the affiliated single-source TS distribution. The source transducer is then moved to the second location S_2^{piezo}, for which the testing and computational procedure are performed anew. In what follows, the superposition of these individual TS distributions is used as a tool to highlight the effect of source aperture on the quality of TS reconstruction. To facilitate the discussion, the set of excitation sources that is used to compute any given TS map is denoted by $\mathcal{S} \subseteq \{1, 2, 3, 4, 5\}$.

SLDV data post-processing As a preparatory step toward computing the TS map, the data were post-processed via filtering of the SLDV velocity signals, numerical integration of the latter to obtain $\boldsymbol{u}^{\text{obs}}$, and supplemental filtering of the displacement signals. The first filter reduces the measurement noise embedded in the "raw" velocity records, while its companion eliminates the spurious low-frequency displacements arising as a consequence of temporal integration. Both velocity and displacement signals were treated by a common band-pass filter with $[f_{\text{low}}, f_{\text{high}}] = [5\,\text{kHz}, 50\,\text{kHz}]$ shown in Fig. 3.7. For the purpose of computing the TS distribution, it is critical that the filter does not distort *the phase* of the motion data that are subsequently used to calculate the adjoint field in (2.10). Accordingly, the particular filter adopted in this study was that of the finite impulse response (FIR) type that has linear phase response.

3.5.2 Nuclear graphite ultrasonic bench testing

Aimed at verifying the isotropic constitutive behavior of nuclear graphite and obtaining its elastic moduli, several ultrasonic bench tests were performed on several specimens manufactured out of nuclear graphite. To asses isotropic behavior, the velocities of compressional P- and shear S- waves were measured in a series of transmission tests with transducers located on the opposite sides of a graphite block. The discrepancy between the phase velocities registered in orthogonal directions was measured at 2% for P-waves and 1% for S-waves, which within the accuracy of the measuring device renders isotropic behavior of the graphite. As for specifying the elastic properties of the graphite, measurements were conducted at 1 MHz transmission on a selection graphite specimens not directly involved in the later SLDV testing. The results, including the

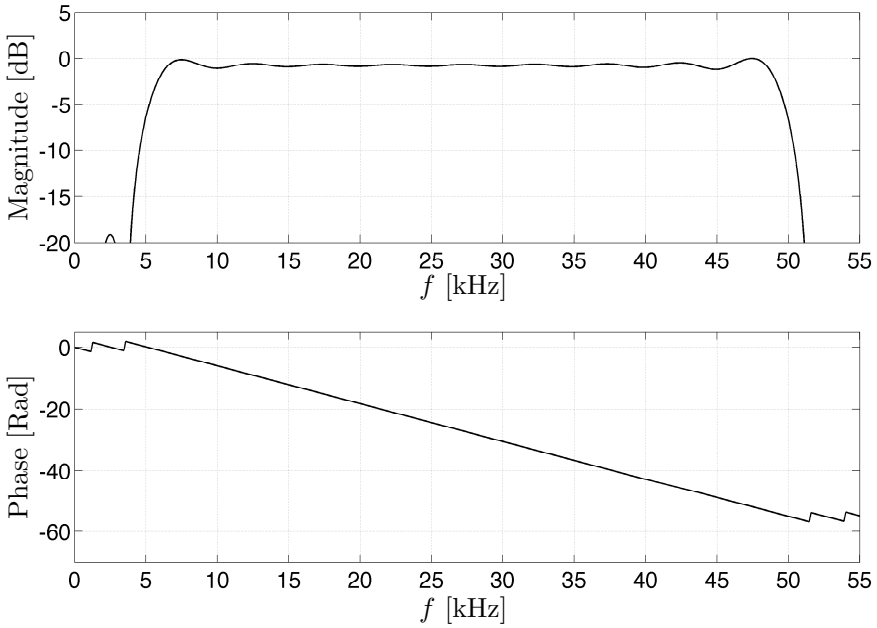

Figure 3.7: Band-pass finite impulse response filter employed for denoising SLDV velocity and (numerically integrated) displacement data.

measured quantities: mass density ρ, P-wave velocity c_{P}, S-wave velocity c_{S}, and the derived elastic moduli: Poisson's ratio ν, Young's modulus E, and shear modulus μ, are presented in Table 3.1.

Sample	ρ [kg/m^3]	c_{S} [m/s]	c_{P} [m/s]	ν	E [GPa]	μ [GPa]
1	1849	1578	2693	0.24	11.41	4.60
2	1832	1443	2605	0.28	9.76	3.82
3	1835	1445	2648	0.29	9.87	3.83
4	1845	1458	2676	0.29	10.11	3.92
5	1847	1597	2680	0.22	11.54	4.71
6	1835	1451	2610	0.28	9.86	3.86
7	1849	1448	2667	0.29	10.01	3.88
8	1849	1444	2614	0.28	9.87	3.86
9	1847	1462	2680	0.29	10.17	3.95

Table 3.1: Ultrasonic bench measurements of a selection of graphite specimens.

As seen from the table, most of the specimens yield similar elastic moduli except for samples 1 and 5 whose Young's moduli are about 15% higher than the average of the rest. Such discrepancy could be induced due to manufacturing process. To this end,

additional ultrasonic tests were performed on the graphite specimens that are directly involved in the SLDV-TS imaging, results presented in Table 3.2. Both the plate and the block graphite specimens were originally manufactured out of a single block and thus have the same properties further utilized in 2D and 3D FE models. One can notice that the measured elastic moduli are similar to those of samples 1 and 5 in the bench tests. On the other hand, the similar test conducted on another available graphite block specimen, not used for SLDV testing, showed elastic properties closer to the rest of the bench test specimens.

$\rho\,[\mathrm{kg/m^3}]$	$c_{\mathrm{S}}\,[\mathrm{m/s}]$	$c_{\mathrm{P}}\,[\mathrm{m/s}]$	ν	$E\,[\mathrm{GPa}]$	$\mu\,[\mathrm{GPa}]$
1842	1573	2725	0.25	11.4	4.56

Table 3.2: Elastic properties of the graphite specimens utilized in SLDV-TS testing.

3.5.3 Graphite plate

A graphite plate of thickness $d=20\,\mathrm{mm}$ with linear sizes $W=\ell=364\,\mathrm{mm}$ (width), $H=306\,\mathrm{mm}$ (height) was tested using SLDV-TS technique in a setup similar to the one utilized for the aluminum plate. A through hole (B_{hole}) of 25 mm in diameter was cut in the plate, see Fig. 3.8b. For the purpose of testing no fixing was required to keep the plate in the upright position. To maximize the traction-free surface, the plate was located onto two supporting props minimizing the contact area with the ground, see display (a). The testing configuration adopted for the graphite plate consists of four source segments S_k^{piezo}, $k=\overline{1,4}$, and 19 observation segments S_j^{obs}, $j=\overline{1,19}$, as shown in Fig. 3.8c. For the kth source location, the induced elastodynamic wavefield is monitored (in terms of in-plane velocity components $\dot{\boldsymbol{u}}^{\mathrm{obs}}$) over 62 SLDV scan points distributed over all four edges of the plate. In contrast to the aluminum plate testing, no scan points were set in the vicinity of the bottom corners of the graphite plate while the (small) contact area is approximated as traction-free surface. In this vein, the points belonging to S_k^{piezo} are used to impose (linearly interpolated) Dirichlet data on S^{D}, while the remainder are deployed to provide the sensory data $\boldsymbol{u}^{\mathrm{obs}}$ on S^{obs}. In the experiment, the 0.5 MHz transducer (Fig. 3.2a) is first placed at S_1^{piezo} to illuminate the damaged area "from the left"; the SLDV motion sensing is then performed at all scan points providing both excitation and observations data. Furhter procedure of computing the TS fields is exactly

the same as in the case of aluminum plate.

It is worth noting that since the graphite plate is considerably thicker than the aluminum plate, the plane stress approximation only holds for smaller frequencies. Indeed, with reference to Table 3.2, $f_c < c_S/9d = 9\,\text{kHz}$. It is nevertheless instructive to examine the performance of TS reconstruction at larger frequencies. In this vein, SLDV data were collected for a regular range of frequencies f_c as described in Sec. 3.2.

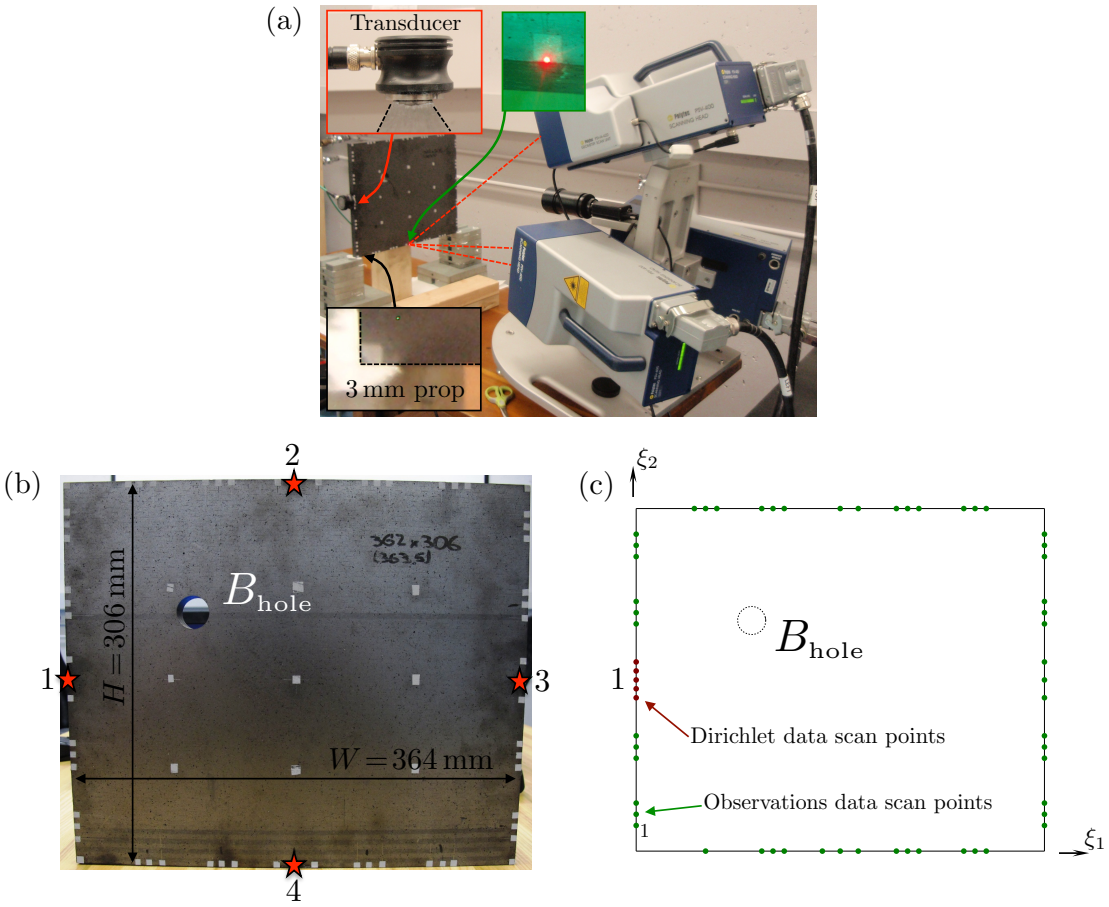

Figure 3.8: Graphite plate experimental setup: a) measurement of the observations data by way of SLDV; b) transducer locations employed to illuminate B_{hole} from all four directions; c) SLDV scan points arrangement in the immediate vicinity of the plate's edges.

3.5.4 Graphite block

A graphite block with dimensions $W = \ell = 364\,\text{mm}$ (width), $H = 306\,\text{mm}$ (height), and $D = 172\,\text{mm}$ (depth) was manufactured for SLDV-TS testing in a 3D setting. For reconstruction purposes, a cylindrical cavity of radius 13 mm and of depth 130 mm was drilled in the block, see Fig. 3.9a. In the following developments, thus created dead-end void is assumed to be located at the back side of the block (see the display) that is "unreachable" for testing purposes, i.e. no excitation/motion sensing is implemented on that part of the boundary. In this setting, SLDV motion sensing is performed over the front, left, and right sides of the block. With the aid of a table tripod setup, a special cart was employed for quick relocation of the scan heads assembly around the block for measurement on either sides, see Fig. 3.9a. During testing, the block was fixed on three rubber supports/props to elevate the specimen above the ground level as seen in the figure.

The block was excited using the 1 MHz transducer glued to the surface of the block at one of the seven locations, shown in Fig. 3.9c. Similar to the case of plate testing, both excitation and observations data were collected via SLDV. In this case, however, a modified setup was employed for the measurement of (Dirichlet) excitation data: in particular, the scan heads were relocated on the floor tripods to focus the laser beams on the base of the transfer rod (Sec. 3.2) as shown in Fig. 3.9b. Here, the transfer rod enables to shoot the lasers at a greater angle with respect to each other – thus facilitation the measurement with sufficient sensitivity in both lateral and axial directions of the transducer's motion. Recall also that the reduced output cross-section of the transfer rod (Fig. 3.2b) helps concentrate the impact of the transducer on a smaller contact patch, which reduces the error in interpolating the respective boundary condition. In this case, the latter is approximated by a constant, i.e. $\boldsymbol{u}^\star(\boldsymbol{\xi}, t) = \boldsymbol{u}^\star(t)$, $\boldsymbol{\xi} \in S_k^{\text{piezo}}$, where S_k^{piezo}, $k = \overline{1,7}$, represents the contact area for the transducer at kth location. The rest of the block's surface was assumed to be traction-free thanks to the premise of insignificant size of the rubber supports. Supporting the latter hypothesis is also the fact that little to no change was registered in the SLDV-recorded motion when the locations of the supports was altered. In this setting, no additional scan points were set in the proximity of the "legs". As in the previous section, SLDV motion sensing was performed anew for each of the locations of the transducer. Also for the sake of simplicity, observation

surface S^{obs} was reduced to a set of boundary points corresponding to the locations of the SLDV scan points so that the virtual excitation of the adjoint field (2.10) takes the form:

$$\boldsymbol{n}\cdot\boldsymbol{\sigma}[\hat{\boldsymbol{u}}](\boldsymbol{\xi},t) \;=\; \sum_{i=1}^{N} \frac{\partial\phi}{\partial\boldsymbol{u}}[\boldsymbol{u}(\boldsymbol{\xi}_i,T-t),\boldsymbol{\xi}_i,T-t]\delta(\boldsymbol{\xi}-\boldsymbol{\xi}_i),$$

with $\boldsymbol{\xi}_i$, $i=\overline{1,N}$, denoting a set of scan points, shown in Fig. 3.9d for a particular case of excitation at the first source location.

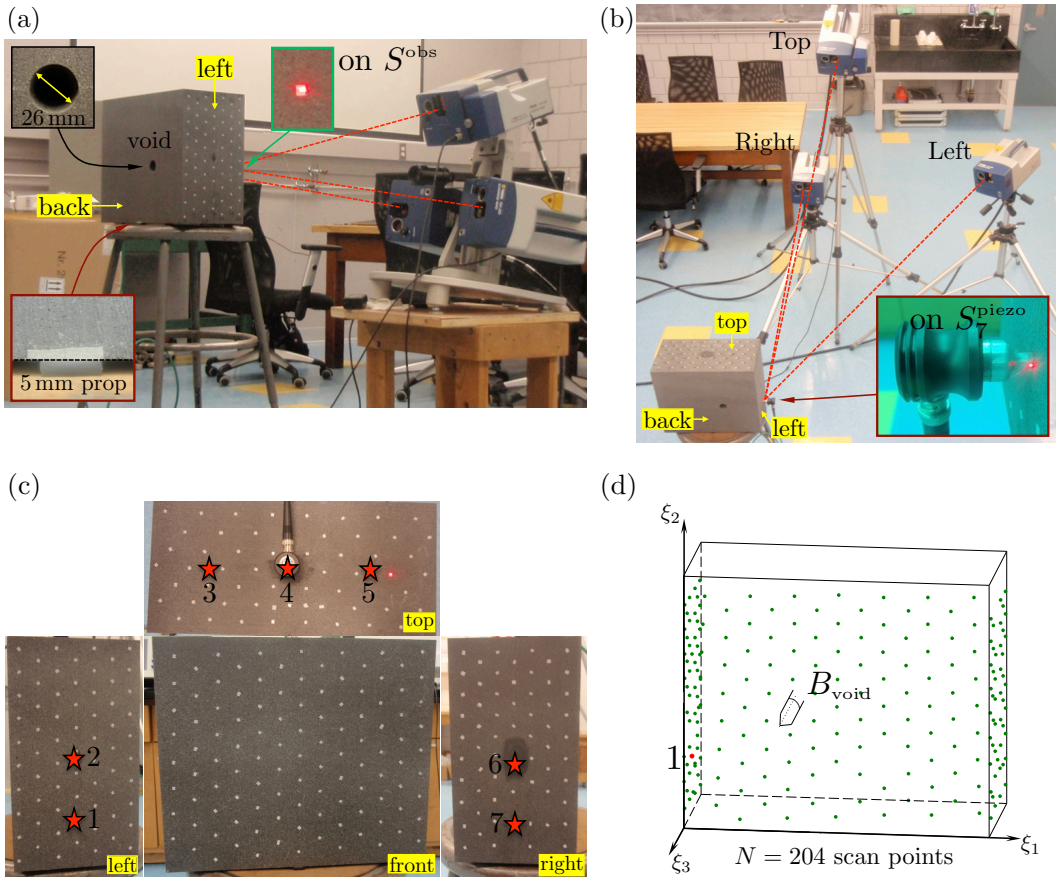

Figure 3.9: Experimental setup for the 3D elastodynamic imaging of a graphite block: a) measurement of the sensory data by way of SLDV; b) specific arrangement of the scan heads for the source (Dirichlet) data acquisition; c) transducer locations on the top, left, and right sides of the block employed to illuminate B_{void}; d) SLDV scan points spatial arrangement in a single-source experiment.

Chapter 4

Computational platform

This chapter (i) describes the FEM computational platform employed for computing the free and adjoint forward elastodynamic states whose bilinear form is used to calculate the TS formula, (ii) deals with the choice of the time windowing function characterizing the proposed cost functional, and (iii) presents the results of synthetic TS reconstruction of damage in a graphite block which approximates the SLDV-TS testing conditions.

4.1 FEM implementation

It is well known that finite element (FE) simulation of elastodynamic problems, such as that deployed herein, produces a number of spurious features in the numerical solution, including dispersion, attenuation, anisotropy, and polarization of elastic waves [49, 50]. In the context of the present study most such distortions, whose effect accumulates with travel distance, may pose a hurdle for TS obstacle reconstruction when the observation interval T in (2.4) takes significant values in the sense that $T \geqslant O(\ell/c_{\mathrm{P}})$, where ℓ is the largest dimension of the domain and c_{P} is the phase velocity of compressional waves.

The numerical scheme adopted for solving (2.1) is a conventional FE method coupled with unconditionally-stable Newmark scheme ($\beta = 0.25$, $\gamma = 0.5$). To reduce the cost of the simulations (especially in 3D), linear elements were implemented, i.e. constant-strain triangles in 2D and constant-strain tetrahedra in 3D. To diminish the effects of numerical anisotropy, dissipation and dispersion dense spatial discretization was proposed featuring unstructured meshes yielding at least 12 elements per dominant S-wavelength, such

that $\kappa = c_S/(f_c h_{max}) \geq 12$, where h_{max} is the maximum distance between the nodes of the mesh, and f_c is the center frequency of the excitation wavelet (Fig. 3.3). An example of such mesh is given in Fig. 4.1a featuring the 2D mesh of aluminum plate generated for FE simulations of the free and adjoint fields at $f_c = 30\,\text{kHz}$ with $\kappa = 12.9$. Given $f_c = 30\,\text{kHz}$, Fig. 4.1b is an example of a coarser 3D mesh for graphite block featuring $\kappa = 8$. In the generated meshes, additional nodes were also added to specific points on the surface of the domain that correspond to the location of the scan points during preceding SLDV testing to reduce the effort of interpolating the input SLDV data.

The Newmark integration time step Δt was chosen such that $h_{max}/(c_P \Delta t) = 1.45$, while the duration of simulations $T = N\Delta t$, where N is the required number of time steps, was conveniently measured in terms of $\tau = \ell/c_P$ – characteristic time required for the P-wave to travel the largest dimension ℓ of the specimen. For example, evaluation of the free field state for duration $T = 6\,\tau$ arising in a specimen characterized by ℓ and spatially discretized with h_{max} requires $N = T/\Delta t = 8.7\,\ell/h_{max}$ time steps.

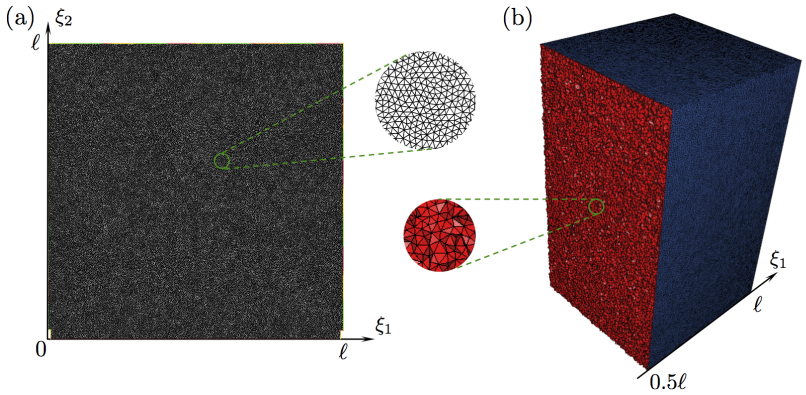

Figure 4.1: Examples of the reference meshes generated for numerical FE simulations of $f_c = 30\,\text{kHz}$ wavefields in: a) aluminum plate; b) graphite block.

Verification of the spatiotemporal discretization in 2D To verify the suitability of the proposed spatiotemporal discretization, a simple test was designed by making use of the fundamental elastodynamic solution $\mathring{\boldsymbol{U}}^1(\boldsymbol{x}, \boldsymbol{\xi}, t)$ in $\mathbb{R}^2$ due to impulsive body force $\boldsymbol{e}_1 \delta(\boldsymbol{x} - \boldsymbol{\xi})\delta(t)$ as in [51]. In this setting, the response of $\mathbb{R}^2$ due to wavelet excitation $\boldsymbol{e}_1 \delta(\boldsymbol{x} - \boldsymbol{\xi}) s(t)$ with time dependence $s(t)$ is computed via the convolution

$$\boldsymbol{u}^s(\boldsymbol{x}, t) = \mathring{\boldsymbol{U}}^1(\boldsymbol{x}, \boldsymbol{\xi}, t) * s(t), \qquad \boldsymbol{x} \in \mathbb{R}^2 \backslash \{\boldsymbol{\xi}\}, \quad t \in \mathbb{R}. \tag{4.1}$$

On taking the excitation wavelet $s(t)$ as in Fig. 3.3 with $f_c = 20\,\text{kHz}$, the numerical approximation of $\boldsymbol{u}^s$ is computed by discretizing the "test" square domain $\Omega^{\text{test}} = [0, L^{\text{test}}] \times [0, L^{\text{test}}]$ ($L^{\text{test}} = 4\,\text{m}$) with triangular finite elements so that $\kappa = 12.7$. Here, material properties of the domain are taken the same as in the aluminum plate (3.4). To preclude contamination of the FE solution with reflections from $\partial\Omega^{\text{test}}$, the point source was placed at $\Omega^{\text{test}} \ni \boldsymbol{\xi} = (L^{\text{test}}/4, L^{\text{test}}/2)$, while the elastodynamic domain response was recorded during a time interval preceding the arrival of the boundary reflections. The FE simulations were performed with two time steps: one computed following the recommendation in [52], namely $\Delta t = h_{\max}/(1.45 c_{\text{S}}) = 2.73\,\mu\text{s}$, and the other taken as $\Delta t = h_{\max}/(1.45 c_{\text{P}}) = 1.58\,\mu\text{s}$. Fig. 4.2 compares the analytical solution in terms of u_1^s versus FE simulations at two radial distances, $r = |\boldsymbol{\xi} - \boldsymbol{x}| = 1.9\lambda_{\text{P}}$ and $r = 9.3\lambda_{\text{P}}$. In both panels, the time interval over which the solutions are compared corresponds to the arrival of the incident P-wave. As can be seen from the display, the larger time step (specified with reference to c_{S}) introduces notable time delay in the arrival of the P-wave at $r = 9.3\lambda_{\text{P}}$, while the smaller time step computed on the basis of c_{P} clearly performs better. Note that further reduction of Δt did not bring about a meaningful improvement of the numerical solution. In the context of cost functional (2.4) and the $\ell \times \ell$ reference domain in Fig 3.6, it is for completeness noted that the arrival of the P-wave at $r = 9.3\lambda_{\text{P}}$ in Fig. 4.2 corresponds to the recording time interval $T \simeq 2.5\,\ell/c_{\text{P}}$.

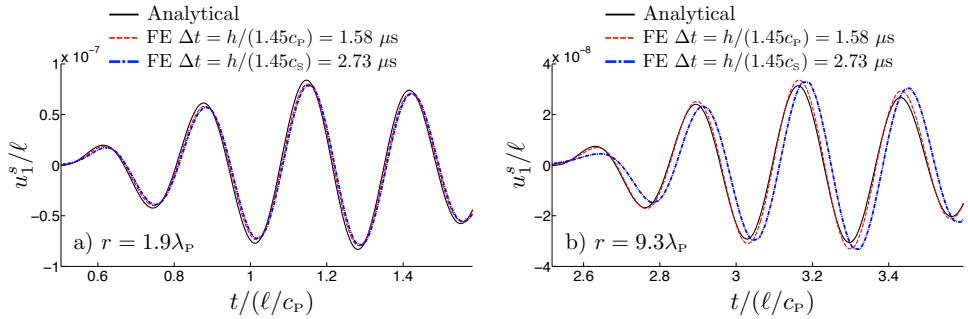

Figure 4.2: Analytical solution vs. FE simulations of the elastodynamic waves in $\mathbb{R}^2$ endowed with material properties of the aluminum plate: temporal variation of $u_1^s(\boldsymbol{x} = (r, 0), \boldsymbol{0}, t)$ immediately following the arrival of the P-wave at distances $r = 1.9\lambda_{\text{P}}$ (left panel) and $r = 9.3\lambda_{\text{P}}$ (right panel).

Implementation in MATLAB and FEniCS In the sequel, data processing as well as computation of the TS map via (2.14) were performed in Matlab with the aid of Digital Signal Processing toolbox, while the FE simulations were carried out using two C++-based open source FEM software packages: (i) FreeFEM++ [53] for 2D plane stress problem; and (ii) FEniCS package [43] for more expensive 3D problem. Developed by the mathematical society, FEniCS has better support in terms of preconditioners/linear solvers and various types of the elements as compared to the more "engineering" approach of FreeFEM++. In this vein, with the aid of Jacobi preconditioner and Conjugate Gradient (CG) iterative solver, FEniCS is better suited for inverting a $O(10^6)$ system such as the one adopted for modeling 3D wavefields in graphite block. Also, since FEniCS is developed in Python, an efficient interface to MATLAB can be established via SciPy add-on which is especially helpful for storing and processing large SLDV-input/FE-output binary data arrays. Note that all FE simulations were performed on a regular multicore desktop machine, in which setting the so-called "embarrassing" parallelization was employed featuring simultaneous computation of several single-source fields via running (independent) serial processes on each of the featured cores.

4.2 Windowing function

As examined in Sec. 2.4, the TS formula (2.14) remains valid as long as the measure of solution distance (2.5) is endowed with a windowing function $W \in C^0(\mathbb{R})$ that is compactly supported over $[0, T]$. Ideally, $W(t)$ should i) equal unity over most of the germane sampling interval, and ii) have sufficiently slow variation so that the Fourier amplitude spectrum of the adjoint field (2.10) is *commensurate* with that of the free field. Under the latter restriction, a common FE mesh of the reference domain (such as that in Fig. 4.1) can be used to compute *both* elastodynamic fields. To meet the foregoing requirements, the windowing function is selected as

$$W(t) \;=\; \begin{cases} 0, & t < 0 \\ 1, & 0 \leqslant t < T - \Delta T \\ W_B\Big(\frac{1}{2} + \frac{t-T+\Delta T}{2\Delta T}\Big), & T - \Delta T \leqslant t < T \\ 0, & t \geqslant T \end{cases}, \tag{4.2}$$

where T is the featured observation interval; $\Delta T \ll T$ is a suitable smoothing period, and W_B denotes the Blackman window [54] given by

$$W_B(t) \;=\; 0.42 \;-\; 0.5\cos(2\pi t) \;+\; 0.08\cos(4\pi t).$$

As an illustration, composite windowing function (4.2) is plotted in Fig. 4.3 together with the Fourier amplitude spectrum of the component Blackman window for a fixed observation interval ($T = 7.4/f_c$) and several values of the smoothing period ΔT.

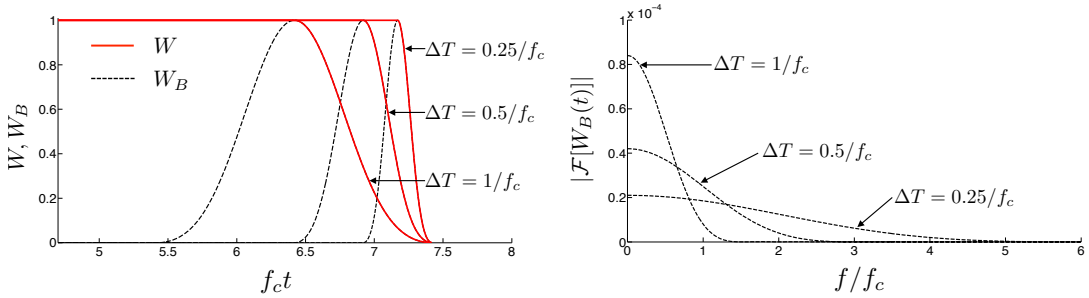

Figure 4.3: Left panel: windowing function $W(t)$ and component Blackman window $W_B\big(0.5 + (t - T + \Delta T)/(2\Delta T)\big)$ evaluated for $T = 7.4/f_c$ and three sample values of the smoothing period: $\Delta T = 0.25/f_c$, $\Delta T = 0.5/f_c$, and $\Delta T = 1/f_c$. Right panel: Fourier amplitude spectra of the respective Blackman window functions.

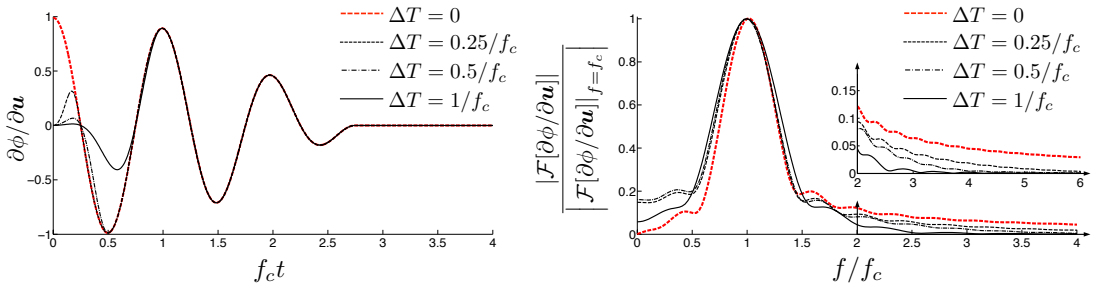

Figure 4.4: Smoothing effect of the weighting function $W(t)$ on a prototypical adjoint-field excitation $\partial\phi/\partial\boldsymbol{u}[\boldsymbol{u}(\cdot, T-t), \cdot, T-t]$ for sample values of the smoothing period ΔT: temporal variation (left panel) and Fourier amplitude spectrum (right panel).

For completeness, Fig. 4.4 highlights the effect of smoothing on the example temporal variation of the adjoint-field excitation

$$\frac{\partial\phi}{\partial\boldsymbol{u}}[\boldsymbol{u}(\cdot, T-t), \cdot, T-t] \;=\; -\,s\big(\tfrac{2.75}{f_c} - t\big), \tag{4.3}$$

where $s(t)$ denotes the original excitation wavelet given by (3.3). In the context of the featured experimental setup, the virtual excitation in (2.10) whose time history resembles (4.3) can be expected for observation points that are located close to the piezoceramic excitation source. As can be seen from the left panel in Fig. 4.4, $\partial\phi/\partial\boldsymbol{u}\big|_{t=0} = -s(\frac{2.75}{f_c}) \neq 0$ which is the principal source of high-frequency "pollution" of the adjoint field in numerical simulations. In particular when $\Delta T = 0$ i.e. $W(t) = H(t)H(T-t)$, the amplitude spectrum of $\partial\phi/\partial\boldsymbol{u}$ diminishes very slowly with f/f_c (see the right panel in Fig. 4.4) which poses a major hurdle toward accurate FE simulation of the adjoint field. A comparison of the respective (source) Fourier spectra in Figs. 3.3 and 4.3 further shows that the smoothing period ΔT should, ideally, be larger than $1/f_c$ for the adjoint field to permit accurate numerical simulation using *the same* FE mesh as that used for computing the free field. On the other hand, "excessive" values of ΔT (in the sense that the hypothesis $\Delta T \ll T$ is violated) may lead to significant loss of information provided by the experimental observations. On the basis of the above considerations, the fixed value of $\Delta T = 0.5/f_c$ is adopted for all experiments.

4.3 Synthetic imaging in graphite block

For synthetic modeling, the SLDV test (detailed in Sec. 3.5.4) computed at $f_c = 30\,\text{kHz}$ is taken as a basis in the sense that the layout of the scan points and excitation sources are the same as in the actual test, while the experimental SLDV data are replaced by the wavefield simulations on a "defective" mesh shown in Fig. 4.5. Similar to the SLDV test, the wavefield is modeled separately for each of the 7 transducer locations shown on the display. In each single-source experiment, the transducer's impact is reproduced via a Dirichlet boundary condition interpolating the SLDV data obtained from corresponding scan points, while the rest of the specimen is considered traction-free. Using thus obtained synthetic observations data as input, the free and adjoint fields are simulated over durations ranging from $T = \ell/c_P$ to $T = 6\,\ell/c_P$. Here, virtual excitation of the adjoint state in terms of point forces prescribed in the locations of the SLDV measurement points (see Fig. 3.9d) was computed by substituting the SLDV data by synthetic data from the true field simulations. Following developments in Sec. 4.2, adjoint field virtual excitation is also time-windowed with a smoothing period $\Delta T = 0.25/f_c = 8\,\mu\text{s}$ to mitigate the effect

of nonzero initial conditions. Using (2.14), single-source TS distributions are calculated and subsequently summed up yielding the multi-source reconstruction maps.

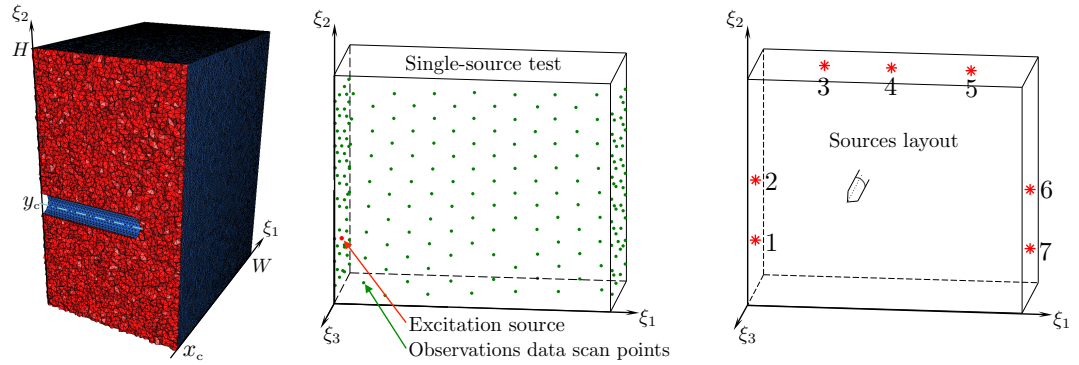

Figure 4.5: Synthetic observations data reconstruction via "defective" FE mesh for graphite block specimen.

To assess the quality of the TS-based reconstruction under various testing conditions, a parametric study was conducted by varying: i) source aperture $\mathcal{S} \subseteq \{1, 2, 3, 4, 5, 6, 7\}$ signifying the collection of excitation sources in Fig. 4.5, and ii) duration of the observation period $T \in \{\tau, 2\tau, \ldots, 6\tau\}$, where $\tau = \ell/c_{\mathrm{P}}$. Since computed TS fields exhibit pronounced negative values in the immediate vicinity of $\partial\Omega$ inherently leading to erroneous defect reconstruction (see also Sec. 5.1), the spatial distributions of the TS maps were truncated at $d_{\mathrm{sp}} = 25\,\mathrm{mm}$ from the margins of the block such that sampling region $\Omega^{\mathrm{TS}} \subset \Omega$ is defined as follows:

$$\Omega^{\mathrm{TS}} = [d_{\mathrm{sp}}, W - d_{\mathrm{sp}}] \times [d_{\mathrm{sp}}, H - d_{\mathrm{sp}}] \times [-D + d_{\mathrm{sp}}, -d_{\mathrm{sp}}]$$

Fig. 4.6 shows individual contributions of the first six sources to the reconstruction of the cavity defect obtained at $T = 6\,\tau$, where the source position is indicated schematically via star-shaped markers. For better visualization, the 3D TS maps are given in terms of several plane projections featuring two planes $\xi_1 = x_{\mathrm{c}}$ and $\xi_2 = y_{\mathrm{c}}$ intersecting along the axis of the void, and 4 planes normal to the axis of the void located at $\xi_3 = -0.4D$, $\xi_3 = -0.5D$, $\xi_3 = -0.6D$, and $\xi_3 = -0.7D$. To focus on the negative values of the TS, positive values are not shown on the maps, while each plane projection is conveniently normalized to the minimum value of -1. As seen from the display, single source maps are contaminated to various extent with spurious minima not affiliated

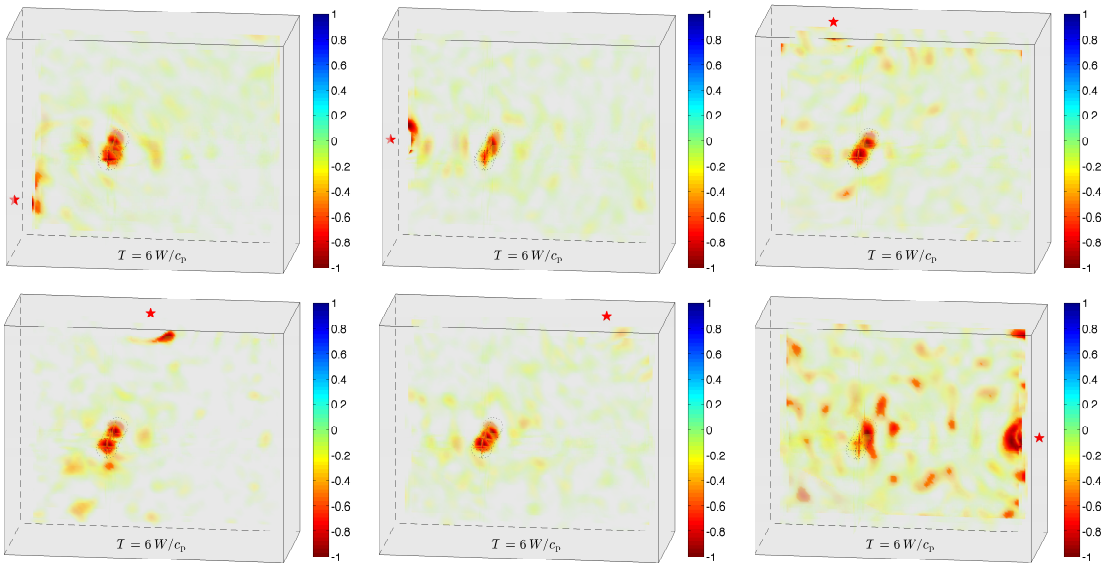

Figure 4.6: Contribution of individual sources to synthetic reconstruction of the cavity defect in graphite block specimen obtained at $f_{\rm c}=30\,\text{kHz}$, $T=6\,\ell/c_{\rm P}$.

with the void deteriorating the reconstruction. In general, summing up maps from various sources helps level out such spurious minima while emphasizing the true minimum circumscribing the defect, see Fig. 4.8.

The effect of duration of the observation period T is shown in Fig. 4.7, featuring TS maps obtained at full source aperture and varying T in terms of characteristic time $\tau = \ell/c_{\rm P}$, $\ell = W = 364\,\text{mm}$. A possible insight on the observed behavior of the TS reconstruction in terms varying duration T could be related to a time scale in the problem defined by the length of the excitation burst $T_{\rm b}=5/f_{\rm c}=1.2\,\ell/c_{\rm P}$ (see Fig. 3.3). Clearly, reconstruction is poor when $T \leq 2T_{\rm b} \simeq 2.4\tau$. On the other hand, there is the spurious wave dispersion in the numerical FE solution, whose adverse effect accumulates with the distance traveled, i.e. with increasing duration T. In the case of synthetic testing, as opposed to the actual experimental imaging in Sec. 5, the latter effect is much less pronounced since numerical dispersion is effectively canceled by the fact that any numerical infidelity introduced to the propagation of the free and adjoint wavefields will be present at the same level in the true wavefield provided similar spatiotemporal discretizations of the true/reference domains. Also known as *inverse crime*, this effect is specific to any inverse problem exposed to synthetic observations data [55].

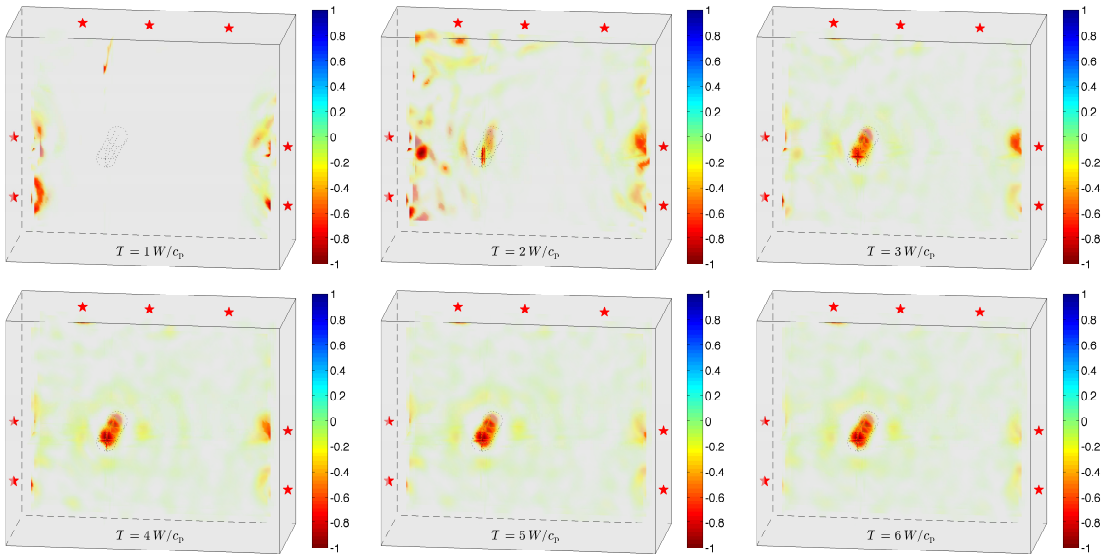

Figure 4.7: The effect of duration T on synthetic reconstruction of the cavity defect in graphite block specimen obtained at full source aperture $\mathcal{S} = \{1, 2, 3, 4, 5, 6, 7\}$ and $f_c = 30\,\text{kHz}$.

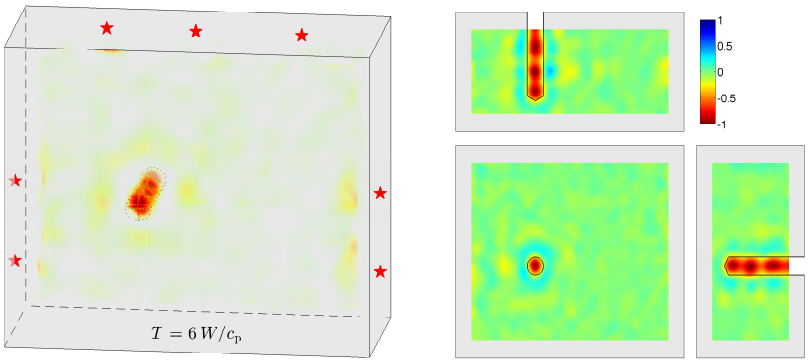

Figure 4.8: Full aperture, $T = 6\tau$, $f_c = 30\,\text{kHz}$ synthetic TS map obtained in Block-1 specimen. Planar views on the right panel feature three mutually orthogonal projections: $\xi_1 = x_c$, $\xi_2 = y_c$, $\xi_3 = -0.5D$, (x_c, y_c) being the center of the cavity in ξ_1–ξ_2 plane.

Chapter 5

Results and discussion

5.1 Imaging in aluminum plate

To investigate the performance of the TS-based reconstruction under various experimental conditions, a parametric study of the TS maps computed via (2.14) was conducted by varying

- Carrier frequency of the excitation signal f_c, see Fig. 3.3;
- Source aperture $\mathcal{S} \subseteq \{1, 2, 3, 4, 5\}$, signifying the collection of excitation sources in Fig. 3.6, and
- Duration of the observation period $T \leqslant T_{\text{exp}}$, featured in cost functional (2.4).

In total, 20 individual TS maps are computed for any fixed T, corresponding to five source locations and four values of the carrier frequency f_c as described in Sec. 3.5.1. To aid the qualitative obstacle reconstruction by way of TS two auxiliary parameters, namely the truncation parameter d_{sp} and cutoff index α, also are introduced as follows.

Truncation parameter d_{sp}. Consistent with the observations from earlier studies [17, 19], it was found that the computed TS fields exhibit pronounced negative values in the immediate vicinity of $\partial\Omega$, which inherently leads to erroneous defect reconstruction. As suggested in [33], such behavior may be affiliated with the localized nature of motion sensing, and could be attributed to the near-field behavior of elastodynamic Green's

tensors when the problem is formulated within a boundary integral equation framework. To mitigate such spurious effect, the obstacle reconstruction can be effected by plotting the spatial distribution of TS *away* from the domain boundaries, as was done for instance in [19]. In the sequel, this strategy is implemented by setting the support of the TS images as

$$\Omega^{\mathrm{TS}} \;=\; [d_{\mathrm{sp}},\ell-d_{\mathrm{sp}}]\times[d_{\mathrm{sp}},\ell-d_{\mathrm{sp}}], \tag{5.1}$$

see e.g. Fig. 5.1; the scaling is effected with respect to its centroid, and d_{sp} specifies the separation between $\partial\Omega^{\mathrm{TS}}$ and $\partial\Omega$. From numerical simulations, it was found that $d_{\mathrm{sp}}=80\,\mathrm{mm}\simeq\ell/12$ is a suitable value for the problem of interest.

Cutoff index α. For the sake of simplicity, each TS map is conveniently normalized as

$$\tilde{\mathsf{T}}(\boldsymbol{z}) \;=\; \mathcal{N}\big[\mathsf{T}(\boldsymbol{z})\big] \;=\frac{\mathsf{T}(\boldsymbol{z})}{\big|\min\limits_{\boldsymbol{z}\in\Omega^{\mathrm{TS}}}\mathsf{T}(\boldsymbol{z})\big|}\;\geqslant -1. \tag{5.2}$$

To focus on the regions on Ω where the TS attains most pronounced negative values, a thresholded distribution [31] of $\tilde{\mathsf{T}}$ is further introduced as

$$\tilde{\mathsf{T}}_{\alpha}(\boldsymbol{z})=\begin{cases}\tilde{\mathsf{T}}(\boldsymbol{z}), & -1\leqslant\tilde{\mathsf{T}}\leqslant-\alpha,\\ 0, & \tilde{\mathsf{T}}>-\alpha,\end{cases}\qquad 0<\alpha<1. \tag{5.3}$$

In general, thresholded TS maps can be used either as a stand-alone tool for *preliminary* obstacle reconstruction (as is the case in this study), or as a preconditioner for the next iteration of the customary TS imaging algorithm, see e.g. [25].

Effect of the illumination frequency Figs. 5.1 and 5.2 plot respectively the spatial distributions of $\tilde{\mathsf{T}}$ and $\tilde{\mathsf{T}}_{\alpha}$ with $\alpha=0.5$ at full source aperture ($\mathcal{S}=\{1,2,3,4,5\}$), maximum duration of the observation period ($T=T_{\mathrm{exp}}=4\,\ell/c_{\mathrm{P}}$ in this case), windowing function parameter $\Delta T=0.5/f_{\mathrm{c}}$, and four carrier i.e. "center" frequencies f_{c} of the illuminating wavelet. As can be seen from the display, the TS resolves circular obstacle B_{hole} (with diameter $d_{\mathrm{h}}=90\,\mathrm{mm}$) via *two distinct modes*, namely by taking pronounced negative values

- *within* B_{hole} at "lower" excitation frequencies, namely $f_{\mathrm{c}}=10\,\mathrm{kHz}$ where $\lambda_{\mathrm{S}}/d_{\mathrm{h}}\simeq 3.4$, and

- *in the neighborhood of* $\partial B_{\rm hole}$ at "higher" excitation frequencies, namely $f_{\rm c} \in \{30\,{\rm kHz}, 40\,{\rm kHz}\}$ where $\lambda_{\rm S}/d_{\rm h} < 1.2$.

In this setting, it is noted that the obstacle reconstruction via TS in the so-called resonance region [56] (where the illuminating wavelength is commensurate with the size of the obstacle) may entail either mode of resolution, or their amalgam – as is the case with "intermediate" frequency $f_{\rm c} = 20\,{\rm kHz}$ where $\lambda_{\rm S}/d_{\rm h} \simeq 1.7$. For completeness, one should also mention that the featured bimodal performance of TS was previously observed in [31, 32] via three-dimensional numerical simulations. In particular the results in [31] suggest, consistent with the findings of this study, that the shear-wavelength-to-mean-obstacle-size ratios of $\lambda_{\rm S}/d_{\rm h} \simeq 2.6$ and $\lambda_{\rm S}/d_{\rm h} \simeq 0.7$ correspond respectively to the "low" and "high" frequency mode of TS reconstruction. Considering the latter, the results in Figs. 5.1 and 5.2 for $f_{\rm c} \geqslant 30\,{\rm kHz}$ clearly reflect the absence of receivers and sources along the bottom edge of the plate in that the "bottom" part of $\partial B_{\rm hole}$ is not reconstructed. In terms of the elongated obstacle $B_{\rm slit}$ whose thickness (6 mm) is more than a decade smaller than its length ($d_{\rm s} = 100\,{\rm mm}$), on the other hand, the TS unequivocally indicates its presence only for $f_{\rm c} \gtrsim 20\,{\rm kHz}$, i.e. $\lambda_{\rm S}/d_{\rm s} \lesssim 1.7$.

To make full use of the multiple data sets obtained at distinct carrier frequencies of the illuminating wavelet (3.2), it is further useful to compute the multi-frequency TS map as

$$\tilde{\mathsf{T}}^{\Sigma}(\boldsymbol{z}) \;=\; \mathcal{N}\left[\sum_{k=1}^{4} \tilde{\mathsf{T}}(\boldsymbol{z})\big|_{f_{\rm c}=f_{\rm c}^{k}}\right], \qquad f_{\rm c}^{k} = 10k\,[{\rm kHz}] \tag{5.4}$$

that is again a piecewise-constant function in Ω and subject to further thresholding according to (5.3). Fig. 5.3 plots the spatial distribution of $\tilde{\mathsf{T}}^{\Sigma}$ and $\tilde{\mathsf{T}}^{\Sigma}_{\alpha=0.5}$, evaluated at full source aperture $\mathcal{S} = \{1, 2, 3, 4, 5\}$ and maximum observation period $T = 4\,\ell/c_{\rm P}$. For future reference, the right panel also indicates via dashed contour the subregion $\Omega' \subset \Omega$ that focuses attention on a neighborhood of the two defects. As can be seen from the display, the featured multi-frequency maps yield reasonably accurate resolution of $B_{\rm hole}$ (especially its "upper" portion) and somewhat less satisfactory reconstruction of $B_{\rm slit}$. As will be shown next, the latter feature is due to substantial sensitivity of the reconstruction maps to source aperture.

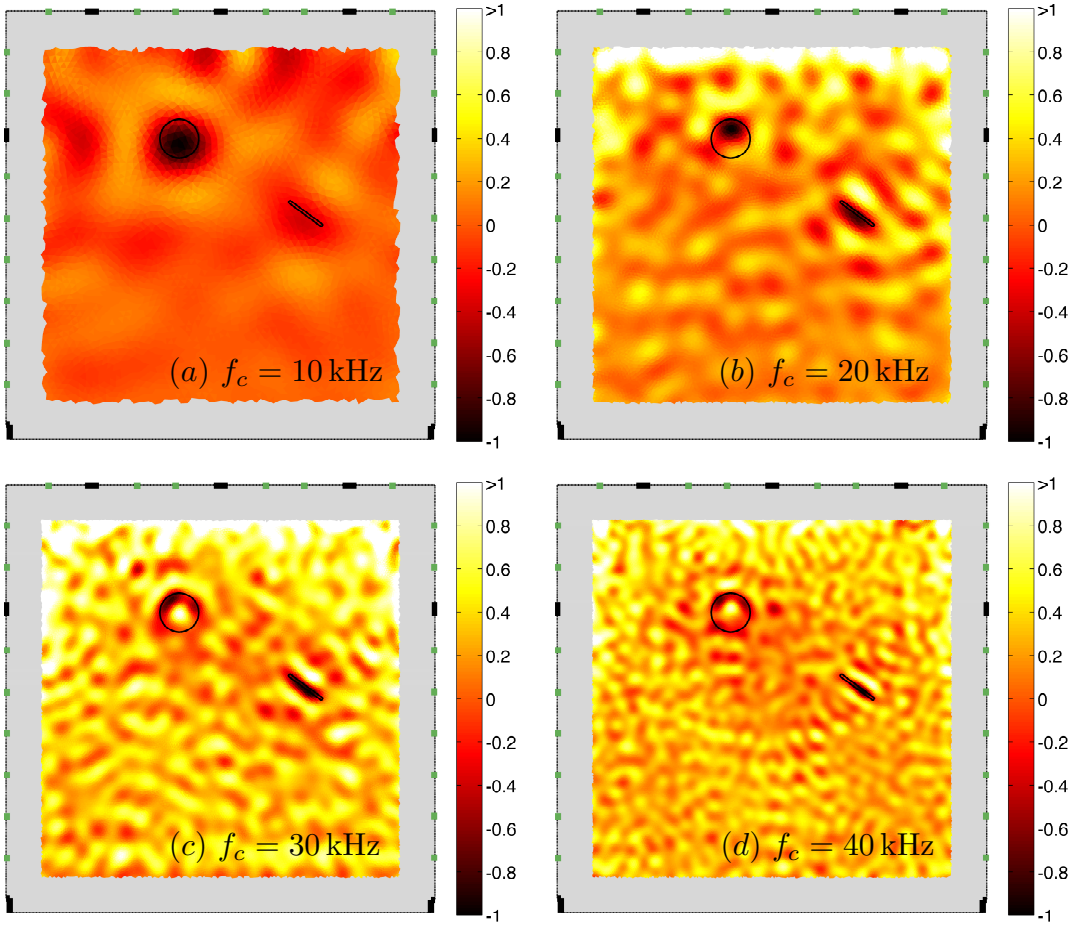

Figure 5.1: Monochromatic maps $\tilde{\mathsf{T}}(\boldsymbol{z})$ obtained with the full source aperture $\mathcal{S} = \{1, 2, 3, 4, 5\}$, observation period $T = 4\,\ell/c_{\mathrm{P}}$, and four carrier frequencies f_{c} of the excitation wavelet. Along the perimeter, thick black lines indicate the Dirichlet part of the boundary S^{D}, while the short green lines signify the observation surface S^{obs}. The true defects B_{hole} and B_{slit} are outlined in black.

Effect of the source aperture Fig. 5.4 plots the multi-frequency maps $\tilde{\mathsf{T}}^{\Sigma}_{0.5}$ over Ω', computed with maximum duration of the observation period $T = 4\,\ell/c_{\mathrm{P}}$ and several source apertures $\mathcal{S} \subset \{1, 2, 3, 4, 5\}$. In the display, panels (a)–(e) show the individual contribution of each source location to the reconstruction of B_{hole} and B_{slit}, where the germane source position is indicated *schematically* via small arcs. From this result, one can identify two distinct source groups, namely i) sources $\{1, 2, 3\}$ that contribute only

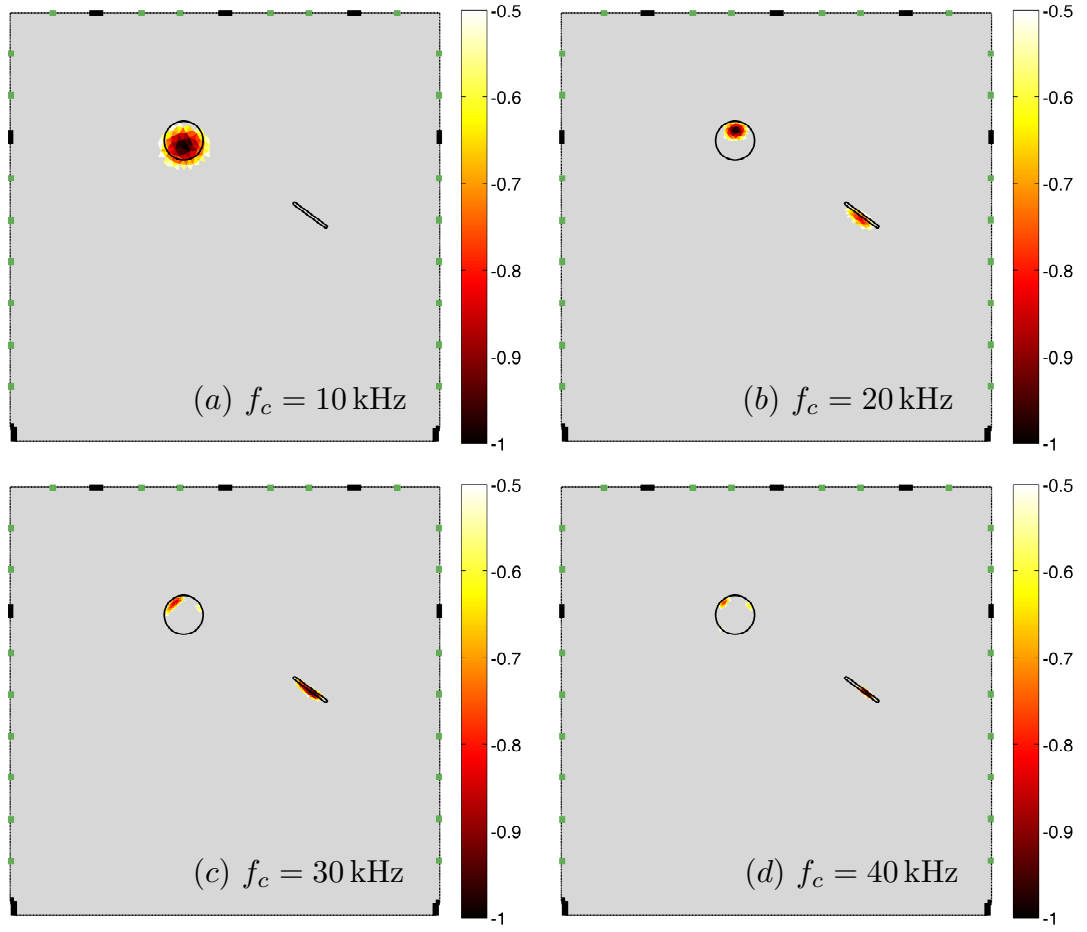

Figure 5.2: Thresholded monochromatic maps $\tilde{\mathsf{T}}_{0.5}(\boldsymbol{z})$ obtained with the full source aperture $\mathcal{S}=\{1,2,3,4,5\}$, observation period $T=4\,\ell/c_{\mathrm{P}}$, and four carrier frequencies f_{c} of the excitation wavelet. Along the perimeter, thick black lines indicate the Dirichlet part of the boundary S^{D}, while the short green lines signify the observation surface S^{obs}. The true defects B_{hole} and B_{slit} are outlined in black.

to the reconstruction of B_{hole}, and ii) sources $\{4,5\}$ that identify B_{slit} while yielding virtually no information about the "distant" circular defect. On summing the contributions from all source locations as in Fig. 5.3, the local minimum of $\tilde{\mathsf{T}}^{\Sigma}$ corresponding to B_{hole}, generated by sources $\{1,2,3\}$, becomes more pronounced than its B_{slit} counterpart due to sources 4 and 5 – which explains the subpar reconstruction of B_{slit}. This apparent

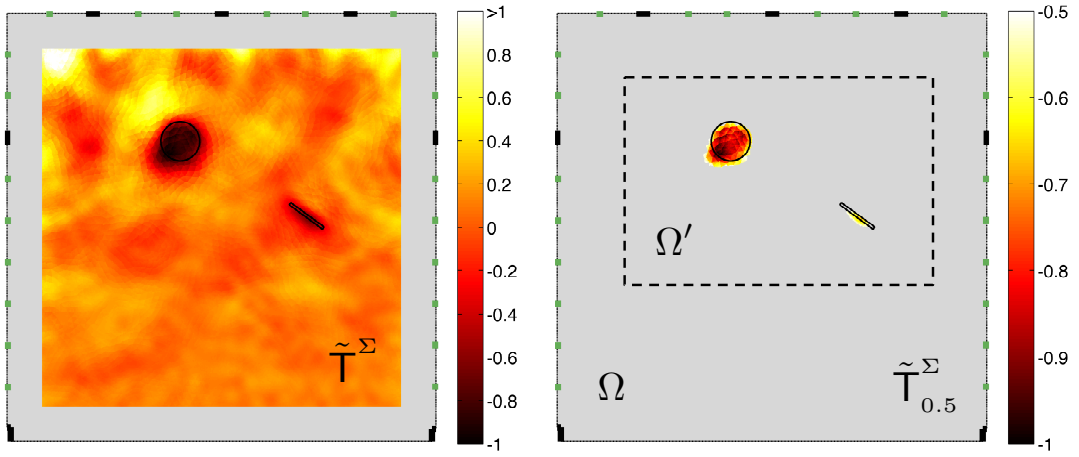

Figure 5.3: Multi-frequency maps $\tilde{\mathsf{T}}^{\Sigma}(\boldsymbol{z})$ (left panel) and $\tilde{\mathsf{T}}^{\Sigma}_{0.5}(\boldsymbol{z})$ (right panel) obtained with the full source aperture $\mathcal{S}=\{1,2,3,4,5\}$ and observation period $T=4\,\ell/c_{\mathrm{P}}$. The true defects B_{hole} and B_{slit} are outlined in black. The right panel also indicates a reference neighborhood, Ω', of the two defects.

sensitivity to the source aperture is further illustrated in panels (f)–(h) of Fig. 5.4, which plot $\tilde{\mathsf{T}}^{\Sigma}_{0.5}$ for selected source subsets $\mathcal{S}\subseteq\{1,2,3,4,5\}$. Indeed, a comparison between the right panel in Fig. 5.3 and panel (i) in Fig. 5.4 demonstrates that by *excluding* the first source location (i.e. by judiciously reducing the source aperture) one enhances the reconstruction of the dual defect via (5.4).

Influence of the observation period The duration of the observation period T, featured in (2.4), essentially represents the amount of information captured in the experiment by a receiver on $\partial\Omega$. In the context of the present study, T is measured in terms of the characteristic time ℓ/c_{P}, which specifies the time for the P-wave to travel the full width of the plate. Another time scale that is relevant in this investigation is the duration of the excitation wavelet, $T_{\mathrm{b}}=\frac{5}{f_{\mathrm{c}}}$, see Fig. 3.3. In this setting, the effect of changing the observation period (while keeping the smoothing period $\Delta T = 0.5/f_{\mathrm{c}}$ unchanged, see Sec. 4.2) is illustrated in Fig. 5.5 by way of the reconstruction maps $\tilde{\mathsf{T}}_{0.5}$, computed at $f_{\mathrm{c}}=30\,\mathrm{kHz}$ with $\mathcal{S}=\{2,3,4,5\}$. For this choice of the excitation wavelet, $T_{\mathrm{b}}=5/f_{\mathrm{c}}\simeq 0.9\,\ell/c_{\mathrm{P}}$.

As can be seen from panel (a), for short durations of the observation period where

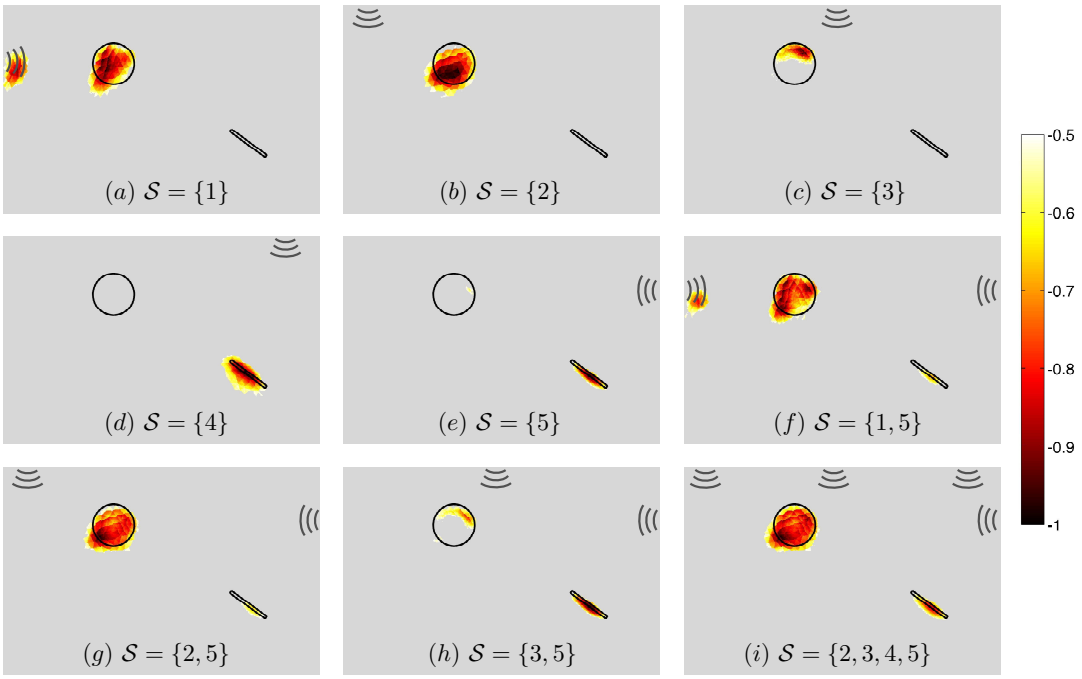

Figure 5.4: Multi-frequency maps $\tilde{\mathsf{T}}^{\Sigma}_{0.5}$, evaluated with $T = 4\,\ell/c_{\mathrm{P}}$ and varying source aperture $\mathcal{S} \subset \{1, 2, 3, 4, 5\}$, over the neighborhood region Ω'.

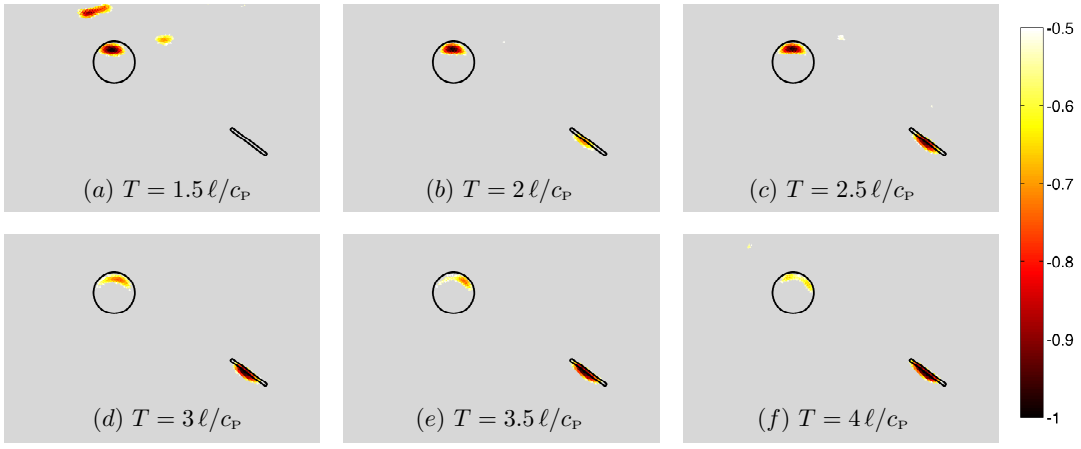

Figure 5.5: Monochromatic maps $\tilde{\mathsf{T}}_{0.5}$ at $f_{\mathrm{c}} = 30\,\mathrm{kHz}$, evaluated with variable duration of the observation period $T \leqslant 4\,\ell/c_{\mathrm{P}}$ and partial source aperture $\mathcal{S} = \{2, 3, 4, 5\}$, over the neighborhood region Ω'.

T is comparable to T_{b}, the TS map is polluted with spurious minima that render the reconstruction meaningless. As T increases, however, the added information strengthens

the local minima near B_{hole} and B_{slit} (panels (b)–(f)), and yields notably improved result starting at $T = 2\,\ell/c_{\text{P}}$. Furthermore, one may observe a partial *shape reconstruction* of the dual defect for $T \geqslant 3\,\ell/c_{\text{P}}$. The latter could be explained as follows. For short observation periods the sources at locations 2 and 3, that are the closest to B_{hole} (see Fig. 3.6), contribute most to the TS minima as seen in panels (a)–(c). With increasing T, on the other hand, the waves (scattered by B_{hole} and B_{slit}) originating from the remaining sources start reaching the receivers, thus exposing ∂B_{hole} to a larger extent, see panels (d)–(f). Also supporting this improvement is the fact that for larger values of T, the circular defect is additionally probed by the waves *reflected* from $\partial\Omega$ which effectively enhances the source aperture. Counteracting the foregoing favorable effects, however, is the spurious wave dispersion in the numerical solution whose adverse effect accumulates with the distance traveled, i.e. with increasing T in the context of shape reconstruction. An interplay between the above competing factors can be seen from panels (d)–(f) in Fig. 5.5, which demonstrate that the quality of TS reconstruction in fact starts to deteriorate for $T \gtrsim 3.5\ell/c_{\text{P}}$.

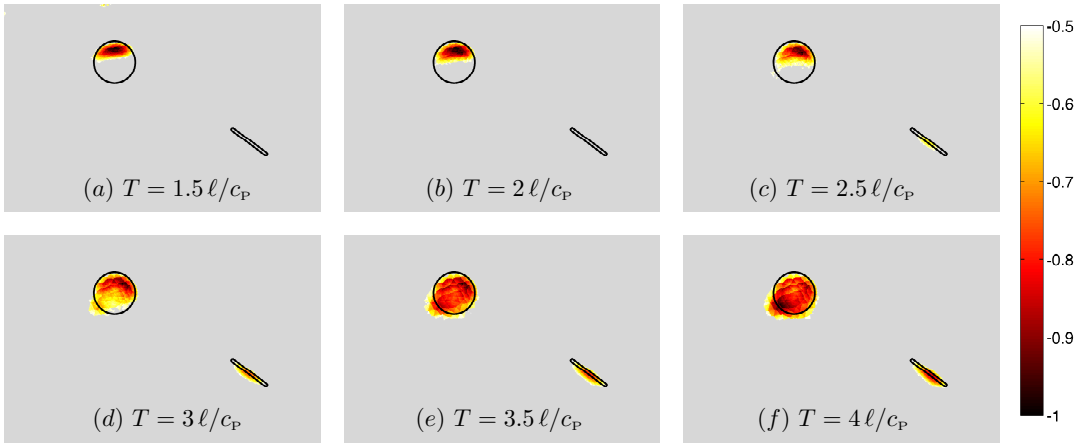

Figure 5.6: Multi-frequency maps $\widetilde{\mathsf{T}}^{\Sigma}_{0.5}$, evaluated with variable duration of the observation period $T \leqslant 4\,\ell/c_{\text{P}}$ and partial source aperture $\mathcal{S} = \{2, 3, 4, 5\}$, over the neighborhood region Ω'.

For completeness, Fig. 5.6 plots the multi-frequency counterpart of the "monochromatic" results in Fig. 5.5. In this case, the discussion is complicated by the varying duration of the excitation wavelet, which ranges from $T_{\text{b}} \simeq 0.7\,\ell/c_{\text{P}}$ at $f_{\text{c}} = 40\,\text{kHz}$ to

$T_{\rm b} \simeq 2.7\,\ell/c_{\rm P}$ at $f_{\rm c} = 10\,{\rm kHz}$. With reference to Fig. 5.2 one in particular notes that for $T \leqslant 2.5\,\ell/c_{\rm P}$, the TS reconstruction in panels (a)–(c) is dominated by the higher-frequency contributions, i.e. those for $f_{\rm c} \geqslant 20\,{\rm kHz}$. This result is consistent with the observations made earlier in that $T/T_{\rm b}|_{f_{\rm c}=10\,{\rm kHz}} < 1$ for $T \leqslant 2.5\,\ell/c_{\rm P}$, which makes the results at 10 kHz ineffective for such "short" observation periods. In the same spirit, one observes a marked improvement in the multi-frequency TS reconstruction for $T \geqslant 3\,\ell/c_{\rm P}$ in panels (d)–(f), where the contribution at 10 kHz begins to "populate" the support of $B_{\rm hole}$.

5.2 Comparison with topological energy-type functionals

For the sake of transparency, it is next instructive to compare the preceding results with their counterparts deriving from the reduced TS functionals proposed in [30, 37, 39]. In [30] and [37], the authors consider the so-called time domain *topological energy* (TDTE) method that identifies obstacles via significant values of the non-negative indicator functional

$$\mathsf{E}(\boldsymbol{z}) \;=\; \{(\boldsymbol{u}\cdot\boldsymbol{u}) * (\hat{\boldsymbol{u}}\cdot\hat{\boldsymbol{u}})\}(\boldsymbol{z},T), \tag{5.5}$$

where $\boldsymbol{u}$ and $\hat{\boldsymbol{u}}$ are the free and adjoint displacement fields defined in Sec. 2. As argued by the authors, (5.5) is designed as a "simple" obstacle indicator that does not require the information about the shape $\mathcal{B}$ of a vanishing defect – that specifies the polarization tensor $\mathcal{A}$ in (2.14). In [39], on the other hand, the authors consider a variant of (5.5) in the form of

$$\mathsf{G}(\boldsymbol{z}) = \{\boldsymbol{u} * \hat{\boldsymbol{u}}\}^2(\boldsymbol{z},T), \tag{5.6}$$

and refer to the resulting reconstruction technique as the fast topological imaging (FTIM) method. Here it is noted that neither forms (5.5) nor (5.6) are bilinear, which complicates their application in the current experimental setting where the source aperture is built *synthetically*, by moving a single excitation transducer from one location to another. Indeed, both [37] and [39] deploy linear ultrasonic arrays where the source aperture is built *physically*, by simultaneously emitting the excitation from all source locations.

To make full use of the featured experimental data set via the TDTE and FTIM methods, the free and adjoint field in (5.5) and (5.6) are provisionally superseded by

the respective aggregate fields

$$\boldsymbol{u}^{\mathrm{tot}}(\boldsymbol{\xi},t)=\sum_{i=1}^{5}\boldsymbol{u}^{i}(\boldsymbol{\xi},t),\quad \hat{\boldsymbol{u}}^{\mathrm{tot}}(\boldsymbol{\xi},t)=\sum_{i=1}^{5}\hat{\boldsymbol{u}}^{i}(\boldsymbol{\xi},t),\quad \boldsymbol{\xi}\in\Omega,\quad t\in[0,T], \tag{5.7}$$

where $\boldsymbol{u}^{i}$ and $\hat{\boldsymbol{u}}^{i}$ are the free and adjoint fields in Ω computed assuming single-source physical excitation at $S_{\mathrm{i}}^{\mathrm{piezo}}$, $i=\overline{1,5}$ (see Fig. 3.6). In this way, the contributions from all sources are merged into a single free field and single adjoint field to emulate the "paintbrush" excitation scheme in [37, 39]. Here it is noted, however, that (5.7) suffers from the *inconsistency* in that the boundary condition over $S_{\mathrm{j}}^{\mathrm{piezo}}\subset\partial\Omega$ in (5.7) has Dirichlet character for $i=j$, and Neumann character otherwise (see Sec. 3.5.1) – which prevents the superposition principle from being applied. Given the smallness of the portion of $\partial\Omega$ covered by $S_{\mathrm{i}}^{\mathrm{piezo}}$, $i=\overline{1,5}$, however, it is still instructive to compare the full-aperture maps of T with those of E and G computed on the basis of (5.7). For the ease of comparison, the non-negative distributions (5.5) and (5.6) are conveniently normalized as

$$\tilde{\mathsf{E}}(\boldsymbol{z})=\frac{\mathsf{E}(\boldsymbol{z})}{\max\limits_{\boldsymbol{z}\in\Omega^{\mathrm{TS}}}\mathsf{E}(\boldsymbol{z})},\qquad \tilde{\mathsf{G}}(\boldsymbol{z})=\frac{\mathsf{G}(\boldsymbol{z})}{\max\limits_{\boldsymbol{z}\in\Omega^{\mathrm{TS}}}\mathsf{G}(\boldsymbol{z})},$$

and thresholded by

$$\tilde{\mathsf{E}}_{\alpha}(\boldsymbol{z})=\begin{cases}\tilde{\mathsf{E}}(\boldsymbol{z}), & \alpha\leqslant\tilde{\mathsf{E}}\leqslant 1,\\ 0, & \tilde{\mathsf{E}}<\alpha,\end{cases}\qquad 0<\alpha<1,$$

$$\tilde{\mathsf{G}}_{\alpha}(\boldsymbol{z})=\begin{cases}\tilde{\mathsf{G}}(\boldsymbol{z}), & \alpha\leqslant\tilde{\mathsf{G}}\leqslant 1,\\ 0, & \tilde{\mathsf{G}}<\alpha,\end{cases}\qquad 0<\alpha<1.$$

In this setting, Fig. 5.7 compares $\tilde{\mathsf{T}}_{0.5}(\boldsymbol{z})$ from Fig. 5.2 with the "all-source" maps of $\tilde{\mathsf{E}}_{0.5}$ and $\tilde{\mathsf{G}}_{0.5}$ for carrier frequencies $f_{\mathrm{c}}=10\,\mathrm{kHz}$, $20\,\mathrm{kHz}$, and $30\,\mathrm{kHz}$. As before, all diagrams are computed over the reduced region (5.1) which excludes sampling points in the immediate vicinity of $\partial\Omega$. As can be seen from the display, $\tilde{\mathsf{E}}_{0.5}(\boldsymbol{z})$ and $\tilde{\mathsf{G}}_{0.5}(\boldsymbol{z})$ yield useful information only at long wavelengths corresponding to $f_{\mathrm{c}}=10\,\mathrm{kHz}$. In contrast, their maps at $f_{\mathrm{c}}=20\,\mathrm{kHz}$ and $f_{\mathrm{c}}=30\,\mathrm{kHz}$ are dominated by highly localized peaks that yield no knowledge about the hidden obstacles.

In general, the subpar performance of the TDTE and FTIM methods in the context of this investigation can be attributed to several reasons, including (i) the reduced nature

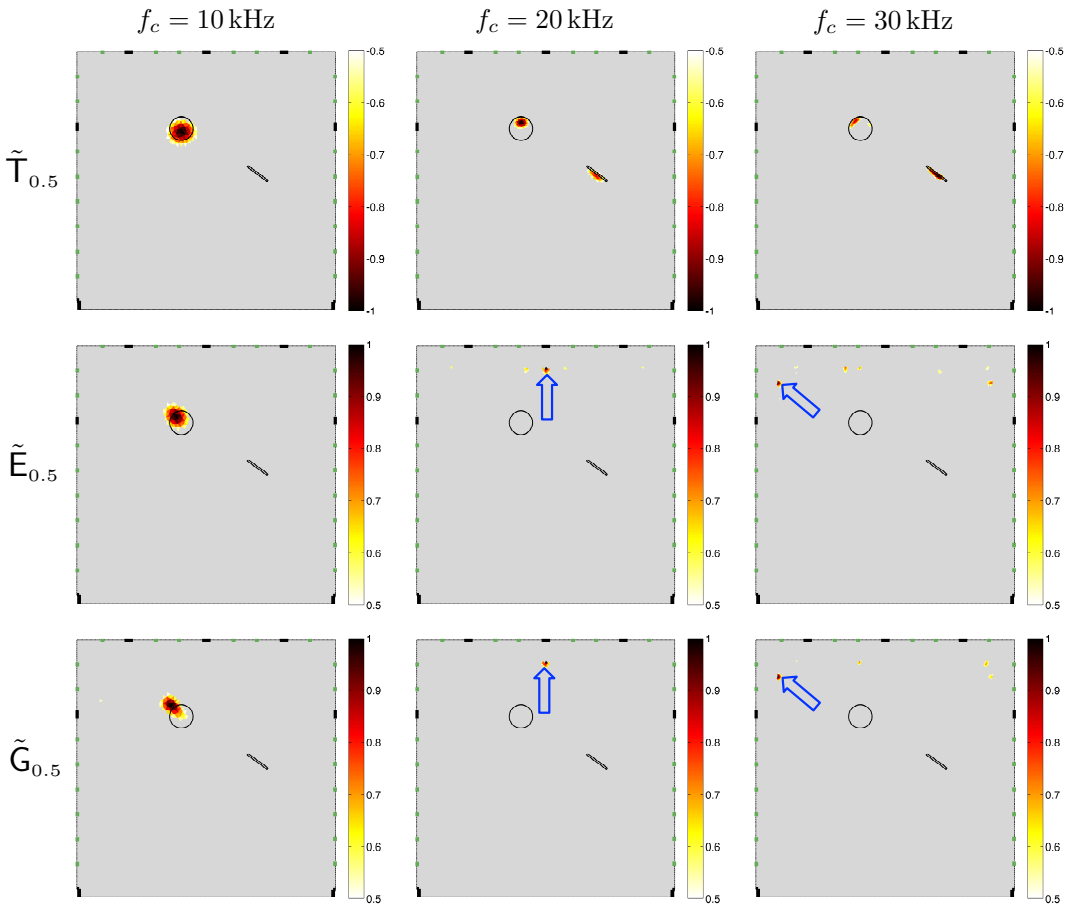

Figure 5.7: Comparison between the *all-source* maps of TS (top row), TDTE (middle row), and FTIM (bottom row) at several excitation frequencies. In the bottom two rows, the arrows indicate the peaks of $\tilde{\mathsf{E}}_{0.5}(\boldsymbol{z})$ and $\tilde{\mathsf{G}}_{0.5}(\boldsymbol{z})$.

of (5.5) and (5.6) relative to (2.14); (ii) the inconsistency in the boundary conditions over $S_{\mathrm{j}}^{\mathrm{piezo}}$ in (5.7), and (iii) low density of the illuminating sources relative to those deployed in [37, 39]. To eliminate the adverse effect of (ii), Fig. 5.8 compares the *single-source* maps of $\tilde{\mathsf{T}}_{0.5}$, $\tilde{\mathsf{E}}_{0.5}$ and $\tilde{\mathsf{G}}_{0.5}$ at $f_{\mathrm{c}} = 20\,\mathrm{kHz}$, which voids the need for using (5.7). For generality, the comparison is effected for three individual source locations, namely $\mathcal{S} = \{1\}$, $\mathcal{S} = \{3\}$, and $\mathcal{S} = \{5\}$. As can be seen from the display, the single-source maps affiliated with the TDTE and FTIM methods are again non-informative, resembling the respective distributions of $\tilde{\mathsf{E}}_{0.5}$ and $\tilde{\mathsf{G}}_{0.5}$ at $f_{\mathrm{c}} = 20\,\mathrm{kHz}$ in Fig. 5.7. From the physical

perspective, one may also mention that the experimental studies in [37] and [39] deploy dense (resp. 64- and 32-element) linear source arrays to create nearly planar incident wavefields. In contrast, the incident fields underpinning Fig. 5.8 stem from a highly localized source, which can possibly explain the disparate performance of the TDTE and FTIM methods when applied to the present data set.

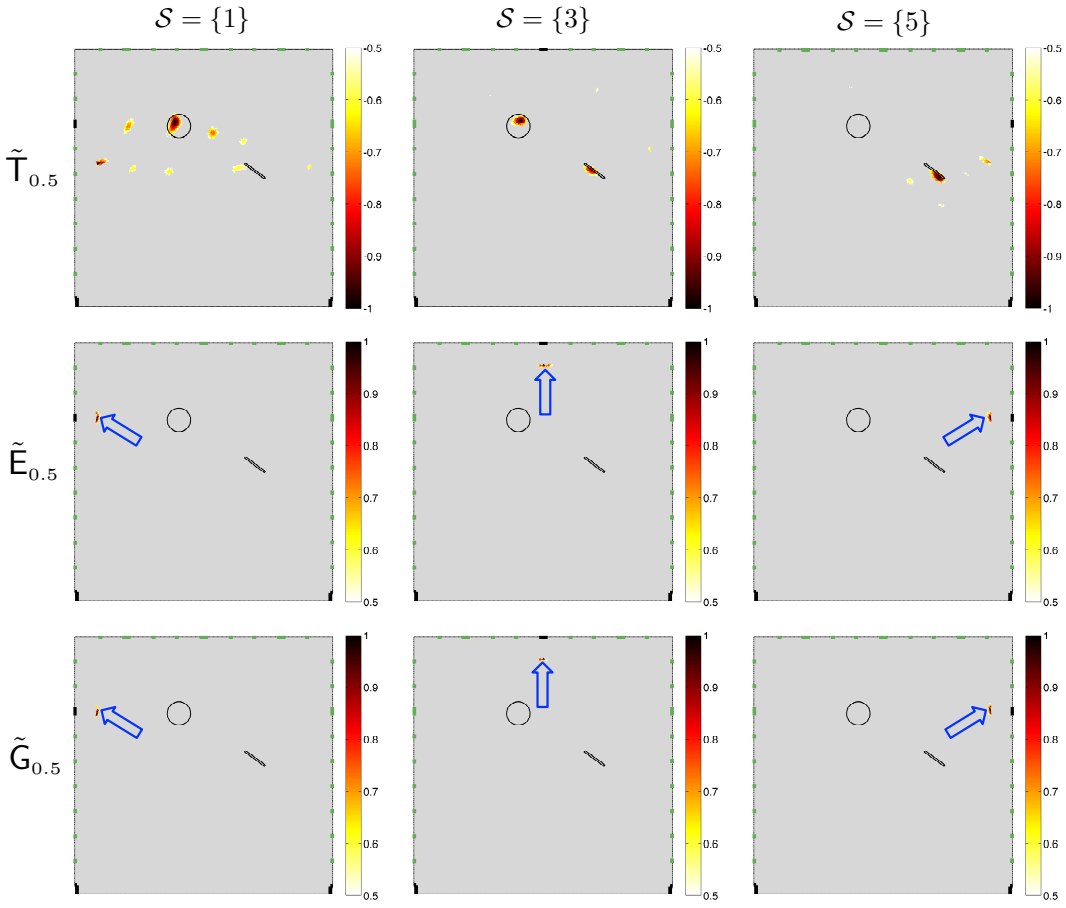

Figure 5.8: Comparison between the *single-source* maps of TS (top row), TE (middle row), and FTIM (bottom row) obtained at $f_c = 20\,\mathrm{kHz}$. In the bottom two rows, the arrows indicate the peaks of $\tilde{\mathsf{E}}_{0.5}(\boldsymbol{z})$ and $\tilde{\mathsf{G}}_{0.5}(\boldsymbol{z})$.

5.3 Imaging in a graphite plate

To facilitate the discussion of the influence of the duration and excitation frequency on the quality of the experimental TS reconstruction, the TS maps $\tilde{\mathsf{T}}$ (notation is borrowed from Sec. 5.1) obtained in the graphite plate specimen are organized in the table shown in Fig. 5.9. Here, the TS maps were truncated with $d_{\mathrm{sp}} = 25\,\mathrm{mm} \simeq \ell/15$. As seen from the display, the hole defect is clearly detected in terms of well-defined minimum on the $f_{\mathrm{c}} = 10\,\mathrm{kHz}$ and $f_{\mathrm{c}} = 20\,\mathrm{kHz}$ maps while at higher frequencies, $f_{\mathrm{c}} \geq 30\,\mathrm{kHz}$, the corresponding minimum is much less pronounced rendering reconstruction almost meaningless. The latter issue is likely related to the inaccuracy of the plane stress approximation as mentioned in Sec. 3.5.3. Note the influence of duration T: at lower frequencies, $f_{\mathrm{c}} \leq 20\,\mathrm{kHz}$, the reconstruction improves as duration increases consistent with the studies on aluminum plate; however at higher frequencies the effect of increasing T is detrimental, i.e. the reconstruction maps deteriorate. Note also that compared to the aluminum plate, larger duration T in terms of characteristic times ℓ/c_{P} is required in the graphite plate to reach satisfactory reconstruction of B_{hole}.

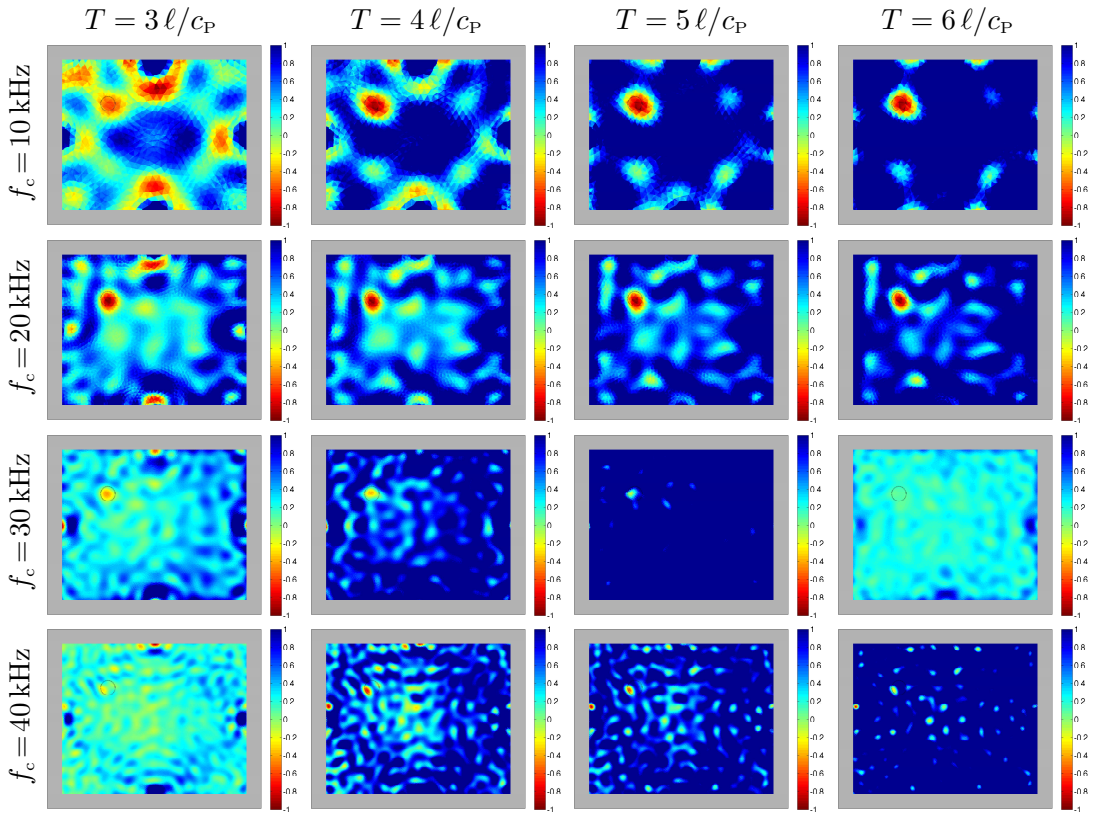

Figure 5.9: 2D TS maps $\tilde{\mathsf{T}}$ obtained in graphite plate specimen at different excitation frequencies f_{c} and durations T.

5.4 Imaging in graphite block

As pointed out in Sec. 4.1, the numerical error in the adopted computational scheme can be controlled via using dense meshes (at least 12 elements per dominant shear wavelength) and tailoring the time step of the Newmark time integration. In 3D, FE simulations are significantly more expensive which renders running additional tests for the sake of tuning the discretization parameters very time consuming. Indeed, with reference to Sec. 4 and Fig. 4.1, the 2D mesh employed for simulation of $f_{\mathrm{c}} = 30\,\mathrm{kHz}$ wavefields in the aluminum plate discretized at $\kappa = 12.9$ contains 84800 triangular elements, while similar coarser 3D mesh for graphite block discretized at $\kappa = 8$ for the

same frequency embodies as many as 5251402 tetrahedral elements. Such dramatic increase in the number of elements is reflected on the inversion times of the linear system, in which sense using a conjugate gradient iterative solver is indispensable for solving $O(10^6)$ system in a reasonable time. From numerical tests, it was found that using CG solver together with Jacobi preconditioner yields CPU inversion time $t_{\rm CG} \simeq 4\,$seconds for a mesh containing about 5 million tetrahedral elements, which added to the the times of (i) stress computation, and (ii) data output into a file, renders the total computational time for simulating single $f_{\rm c}=20\,$kHz wavefield in graphite block to a final time of $T=6\,\ell/c_{\rm P}$ at about 6 hours. It is assumed here that the established earlier spatial-to-temporal discretization ratio is utilized, $h_{\max}/(c_{\rm P}\Delta t)=1.45$.

Due to the high cost of simulations in 3D, TS maps in graphite block were obtained at this stage using coarser ($\kappa \simeq 8$ as in Fig. 4.1b) tetrahedral meshes. In this setting, Figs. 5.10 and 5.11 plot (truncated at $d_{\rm sp}=20\,$mm$=\ell/18$) monochromatic multi-source TS maps $\tilde{\mathsf{T}}_{0.5}$ (the notation borrowed again from Sec. 5.1) obtained respectively at $f_{\rm c}=20\,$kHz and $f_{\rm c}=30\,$kHz in graphite block at various durations T. On the displays, the three-dimensional TS maps are sampled in terms of the following planar views with reference to a Cartesian frame $\{O;x,y,z\}$: (i) two perpendicular axial planes $x=x_{\rm c}$, $y=y_{\rm c}$, and (ii) four normal planes $z=z_{\rm c}^j$, $j=\overline{1,4}$ dissecting $B_{\rm void}$ at $z_{\rm c}^j=-(3+j)\cdot(D/10)$. Here, $(x_{\rm c},y_{\rm c})$ is the location of the axis of $B_{\rm void}$ in ξ_1–ξ_2 plane (see Fig. 3.9d), and $D=172\,$mm is the depth of the block, note that the depth of the void is $d_{\rm c}=130\,$mm$=0.76D$.

As seen from the $f_{\rm c}=20\,$kHz maps in Fig. 5.10, a "meaningful" reconstruction of $B_{\rm void}$ can only be obtained when the duration of the observation period is large, $T\simeq 6\,\ell/c_{\rm P}$ which is consistent with the results of synthetic imaging in Sec. 4.3. Note that within this duration the P-wave travels as far as $r=16\lambda_{\rm P}$ which is about the same as in the case of $f_{\rm c}=20\,$kHz, $T=4\,\ell/c_{\rm P}$ reconstruction in aluminum plate for which $r=14.8\lambda_{\rm P}$. However, in contrast to the results of synthetic reconstruction, one can see the presence of spurious minima not affiliated with the actual obstacle $B_{\rm void}$, whose presence/intensity diminishes but does not vanish as T increases. Note that it is possible to mitigate the effect of spurious near-boundary minima by increasing the truncation distance to $d_{\rm sp}=40\,$mm. In this manner, however, very small fraction of the block will be exposed, while more than 40 % by volume will be lost, which renders the imaging almost meaningless.

When the illuminating frequency is increased to $f_{\rm c}=30\,$kHz (see Fig. 5.11), the

detrimental effect of large durations T becomes even more pronounced in the sense of strong localization of the negative values of the TS field inside smaller subregions of B_{void}. Here, the effect of increasing d_{sp} does not bring any improvement to the reconstruction of the obstacle whatsoever. An effort was also made to amend the observed effect by alternating the accuracy of the numerical treatment in terms of reducing the numerical time step such that $h_{\max}/(c_{\text{P}}\Delta t) = 3$, the result of which is given in Fig. 5.12. Note a significant change in the distribution of the TS field featuring improved "visibility" of B_{void} but (persistent) pollution with spurious minima dispersed over Ω similar to Fig. 5.10.

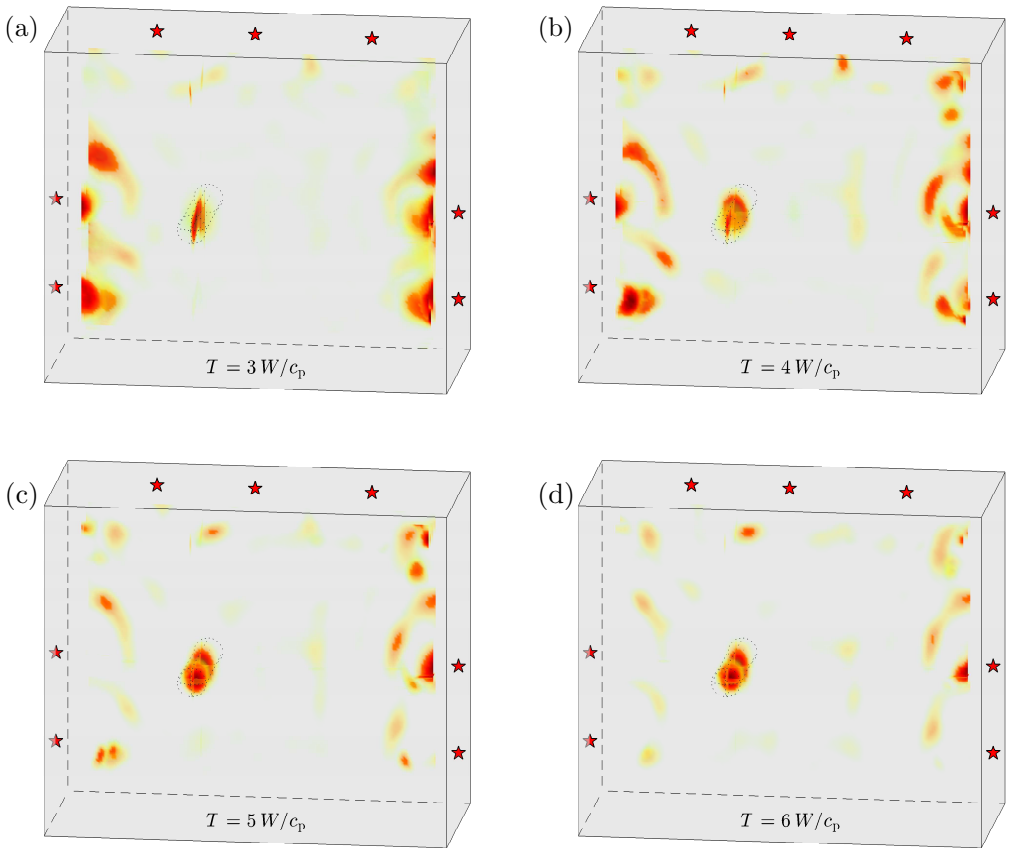

Figure 5.10: Monochromatic reconstruction TS maps obtained in graphite block at $f_{\text{c}} = 20\,\text{kHz}$ at different durations: a) $T = 3\,\ell/c_{\text{P}}$; b) $T = 4\,\ell/c_{\text{P}}$; c) $T = 5\,\ell/c_{\text{P}}$; d) $T = 6\,\ell/c_{\text{P}}$.

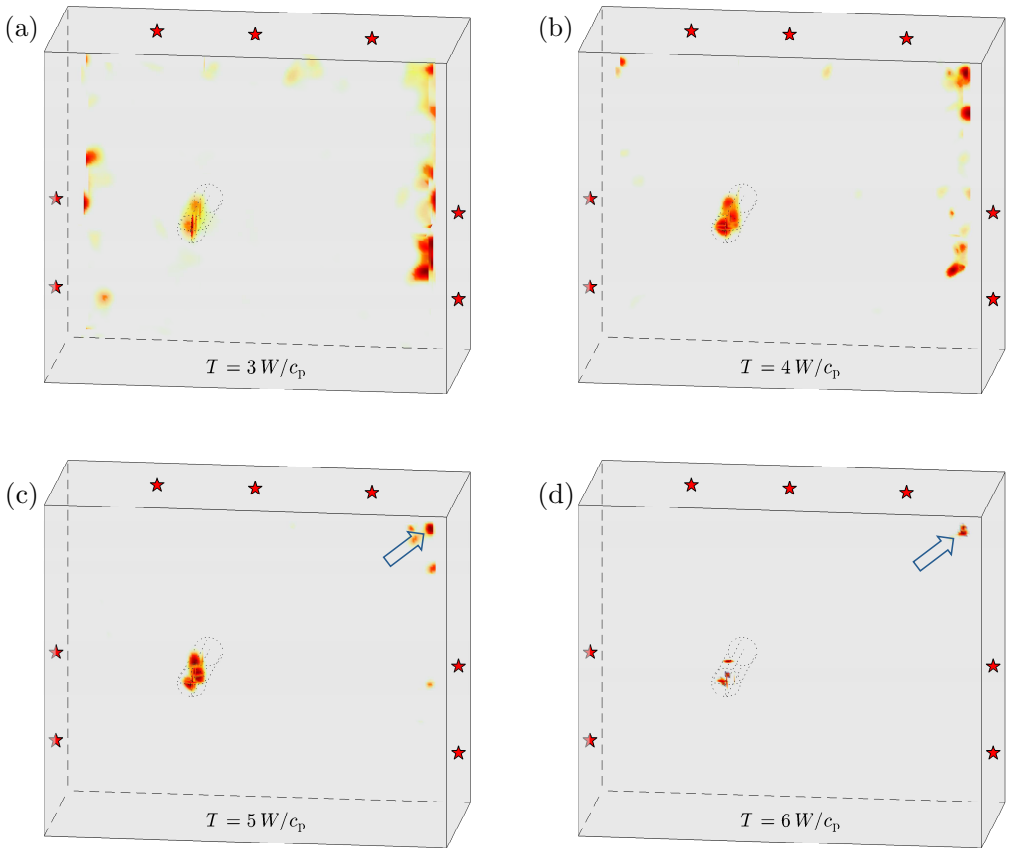

Figure 5.11: Monochromatic reconstruction TS maps obtained in graphite block at $f_{\mathrm{c}} = 30\,\mathrm{kHz}$ at different durations: a) $T = 3\,\ell/c_{\mathrm{P}}$; b) $T = 4\,\ell/c_{\mathrm{P}}$; c) $T = 5\,\ell/c_{\mathrm{P}}$; d) $T = 6\,\ell/c_{\mathrm{P}}$.

5.5 Possible sources of error in experimental TS imaging

The results of the experimental studies presented in this chapter clearly indicate that the ability to reconstruct defects in solids by virtue of plotting multi-source TS function is strongly dependent on several different factors including the frequency content of the illuminating elastic waves, source and motion sensing apertures, duration of the motion sensing records, as well as the TS maps post-processing parameters. On top of all of these effects, previously studied in the context of synthetic imaging, one additional and exceptionally important impact was also observed, namely the influence of the numerical

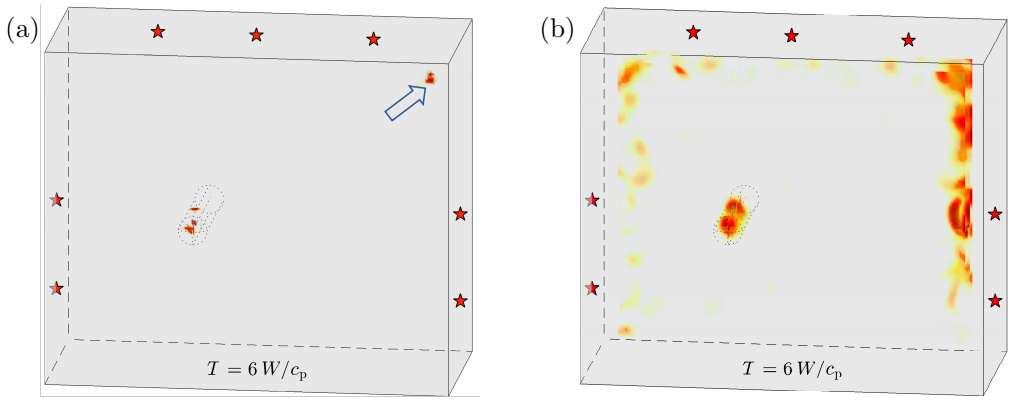

Figure 5.12: Reconstruction TS maps obtained in graphite block at $f_{\mathrm{c}}=30\,\mathrm{kHz}$, $T=6\,\ell/c_{\mathrm{P}}$ using: a) $h_{\max}/(c_{\mathrm{P}}\Delta t)=1.45$; b) $h_{\max}/(c_{\mathrm{P}}\Delta t)=3$.

modeling of the reference wave propagation problem. In this manner, the success of reconstruction is (quite drastically) affected by the accuracy of the adopted mathematical model and its subsequent numerical treatment. The situation is aggravated by the fact that any error in the model is accumulated with travel distance of the elastodynamic waves propagating in the reference medium. Indeed, the induced propagation error will affect the reconstruction in a linear fashion since TS distribution is a linear function of the dataset (2.14). To quantify the propagation error, one may use the dimensionless ratio $\Delta T/T_0$, where ΔT is some (constant) phase shift of the model and T_0 is a period of the wave. Since $\Delta T=|L/c_{\mathrm{P}} - L/c_{\mathrm{P}}^{\mathrm{mod}}|$, where $c_{\mathrm{P}}^{\mathrm{mod}} \neq c_{\mathrm{P}}$ is a model velocity, L – distance traveled by the wave, and $T_0=1/f$ – period of the wave, f – frequency of the wave:

$$\frac{\Delta T}{T_0} = f\frac{L}{c_{\mathrm{P}}^{\mathrm{mod}}}\,\frac{|c_{\mathrm{P}}^{\mathrm{mod}} - c_{\mathrm{P}}|}{c_{\mathrm{P}}} = fT\,\frac{|c_{\mathrm{P}}^{\mathrm{mod}} - c_{\mathrm{P}}|}{c_{\mathrm{P}}}, \tag{5.8}$$

where $T=L/c_{\mathrm{P}}^{\mathrm{mod}}$ is the duration of propagation. Therefore, the propagation error is proportional to both the frequency of the illuminating wave, and the duration of propagation. Note that if reconstruction is performed at high frequencies and longer durations, even small relative velocity error can produce significant propagation error and lead to an erroneous TS map.

The question of quantifying the contributions from each of the possible sources of error in the wave propagation problem is beyond the scope of this study. From the

mathematical model point of view, one should examine the influence of the uncertainty in the boundary conditions as well as the effect of variation in the elastic moduli of the utilized BVP. It is also important to study the effect of signal-to-noise ratio in the experimental data to the performance of TS reconstruction. From the computational platform standpoint, a rigorous analysis of the accumulated error in the FE-simulated wavefields is required. Notwithstanding the complexity of the general error analysis, the last chapter of this study makes an attempt towards improving imaging results in the graphite block by implementing alternative computational technique termed Discontinuous Galerkin method.

Chapter 6

Discontinuous Galerkin FE solver upgrade

One major hurdle for the TS waveform tomography is testing under the conditions of limited excitation/sensing aperture, for example when some of the boundaries of the domain are inaccessible for measurement purposes. For finite domains, the "spatial" lack of information in the sensory data can be somewhat compensated by increasing the temporal duration of the waveform measurements – which allows the waves to reflect from the outer boundaries and "sample" the anomalies from various directions. In this setting, one has to tackle the long-range simulation of transient wave motion which poses major challenges in terms of desired accuracy and affiliated computational cost. One possible solution is to deploy a high-order Discontinuous Galerkin (DG) method. In the first attempt to exercise the method, serial implementation in Matlab has shown very good accuracy for simulating long-range wave propagation in two dimensions with coarse mesh. To tackle the more expensive problem of three-dimensional wave propagation, a parallel DG code was implemented with the aid of of an open-source FEM package FEniCS. Equipped with the latter, the TS imaging in a graphite block is performed and the results are compared to i) synthetic imaging, and ii) imaging with previously established CG method.

6.1 Introduction

Discontinuous Galerkin Method, further referred to as the DG method, was first introduced in the context of neutron transport problem by Reed and Hill, 1973 [57]. It was not until recently, however, that the DG methods have evolved in a manner that made them suitable for use in various computational tasks. A complete overview of the development of the method can be found, for example, in [58] and references there. The main ingredient of the DG approach to tackling (nonlinear) systems of partial differential equations is borrowed from the finite volume method framework, namely the concept of numerical fluxes [59]. Essentially, DG methods employ conventional finite element methodology without strong enforcement of the C^0-continuity of the shape functions across the sides of the elements, whereas numerical fluxes are utilized to weakly impose the cross-element physical constraints. In this setting, the physical solution of a problem is projected onto a (polynomial) finite dimensional space in each element locally, while the information between the adjacent elements and through the outer boundaries of the computational domain is exchanged via non-vanishing boundary flux-term that is a function of the solutions from both sides of the boundary. Such scheme, therefore, allows for discontinuities in the system variables, while the goal of the flux function is to mimic the underlying physics as necessary to obtain accurate (possibly naturally discontinuous) solutions.

Due to aforementioned locality of the spatial approximation, auxiliary degrees of freedom need to be introduced to the system, which renders the DG methods computationally more expensive (both memory- and CPU time-wise) when compared to the conventional finite element and finite difference techniques. On the other hand, the DG methods also possess a set of attractive features, namely: i) the actual order of accuracy of a DG method solely depends on the exact solution, i.e. formally arbitrarily high-order method can be obtained by suitably choosing the order of the approximating polynomials in the corresponding elements, ii) discontinuous shape functions render easily-invertible block-diagonal mass matrix making DG methods well suited for massive parallelization, and iii) DG methods provide excellent adaptivity since mesh refinement or coarsening as well as alternating local polynomial basis are not restricted by the continuity and conformity conditions between the elements. As with any other numerical

method, the efficiency of DG approach depends on many computational and analytical aspects pertaining to a specific application. It should also be noted that another drawback of DG methods is more complex algorithm which decelerates the coding and general development.

On par with numerous applications in the parent field of computational fluid dynamics, see e.g. [60], the DG approach has also been employed in the context of elastic wave propagation. In particular, recently proposed in this vein is the so-called Arbitrary high-order DERivative Discontinuous Galerkin method (ADER-DG) [61] suitable for various classes of transient elastic wave propagation problems, including propagation in viscoelastic [62], heterogeneous [63], and anisotropic media [64]. The results of exercising the method in several test problems in these works show favorable convergence rates with accuracies reaching machine precision when the order of the approximating polynomials is very high ($\gtrsim 8$). Moreover, the method was recently successfully applied to a large-scale numerical seismology problem of modeling dynamic ruptures [65, 66]. In essence, ADER-DG method combines high-order DG elements and high-order ADER time integration [59] to obtain a numerical scheme of the same (theoretically arbitrarily high) order in space and time. The method also utilizes orthogonal basis functions [67] yielding diagonal mass matrix which together with the explicit one-step time marching scheme renders the method feasible for computationally elaborate problems such as long-range wave propagation. Another feature that is relevant in the context of this study is the use of an upwind flux function (Godunov flux) that is known [68] to have dominant numerical dissipation error over the dispersion error. In this setting, the higher frequency modes, i.e. those that are poorly resolved by the spatial grid, are automatically attenuated without affecting the germane modes pertaining to the numerical model. All things considered, ADER-DG provides a robust computational platform for high-fidelity numerical treatment of transient wave propagation in the context of TS imaging especially when longterm propagation is desired.

6.2 Discontinuous Galerkin formulation of linear elastodynamics

This section briefly derives the DG semi-discrete system for the case of 3D elastic wave propagation in a homogeneous linear isotropic media. With reference to the Cartesian coordinate system $\{O; x, y, z\}$ consider stress-velocity formulation of the equations of linear elastodynamics:

$$\frac{\partial}{\partial t}\boldsymbol{u}(\boldsymbol{x},t) + A\frac{\partial}{\partial x}\boldsymbol{u}(\boldsymbol{x},t) + B\frac{\partial}{\partial y}\boldsymbol{u}(\boldsymbol{x},t) + C\frac{\partial}{\partial z}\boldsymbol{u}(\boldsymbol{x},t) = \boldsymbol{S}(\boldsymbol{x},t), \tag{6.1}$$

where $\boldsymbol{u} = [\boldsymbol{\sigma}, \boldsymbol{v}]^{\mathrm{T}}$ – state vector combining the stresses $\boldsymbol{\sigma} = [\sigma_{xx}, \sigma_{yy}, \sigma_{zz}, \sigma_{xy}, \sigma_{yz}, \sigma_{xz}]^{\mathrm{T}}$ and the velocities $\boldsymbol{v} = [v_x, v_y, v_z]^{\mathrm{T}}$, A, B, C – Jacobi matrices, whose explicit definition in terms of Lame moduli λ, μ and mass density ρ is given in [41], and $\boldsymbol{S} = [\boldsymbol{0}, \rho\boldsymbol{f}]^{\mathrm{T}}$ – source term catering for body forces $\boldsymbol{f}$. The eigenstructure of thus constructed hyperbolic system is the key component of developing the numerical scheme based on DG discretization.

The eigenvalues Λ_i, $i = \overline{1,9}$ of the Jacobi matrices in 6.1, given in the ascending order, are the following:

$$\begin{aligned} \Lambda_1 = -c_{\mathrm{P}}, \quad \Lambda_2 = -c_{\mathrm{S}}, \quad \Lambda_3 = -c_{\mathrm{S}}, \\ \Lambda_4 = 0, \quad \Lambda_5 = 0, \quad \Lambda_6 = 0, \\ \Lambda_7 = c_{\mathrm{S}}, \quad \Lambda_8 = c_{\mathrm{S}}, \quad \Lambda_9 = c_{\mathrm{P}}, \end{aligned} \tag{6.2}$$

where c_{P}, c_{S} – P- and S- phase velocities, respectively, defined previously in Sec. 2.1. System 6.1 supports propagation of the two compressional waves (Λ_1, Λ_9) and four shear waves (Λ_2, Λ_3, Λ_7, Λ_8), taking into account two possible polarizations. The corresponding eigenvectors, computed for matrix A, are given column-wise by the matrix

of the right eigenvectors R^{A}:

$$R^{\mathrm{A}} = \begin{bmatrix} \lambda+2\mu & 0 & 0 & 0 & 0 & 0 & 0 & 0 & \lambda+2\mu \\ \lambda & 0 & 0 & 0 & 1 & 0 & 0 & 0 & \lambda \\ \lambda & 0 & 0 & 0 & 0 & 1 & 0 & 0 & \lambda \\ 0 & \mu & 0 & 0 & 0 & 0 & 0 & \mu & 0 \\ 0 & 0 & 0 & 1 & 0 & 0 & 0 & 0 & 0 \\ 0 & 0 & \mu & 0 & 0 & 0 & \mu & 0 & 0 \\ c_{\mathrm{P}} & 0 & 0 & 0 & 0 & 0 & 0 & 0 & -c_{\mathrm{P}} \\ 0 & c_{\mathrm{S}} & 0 & 0 & 0 & 0 & 0 & -c_{\mathrm{S}} & 0 \\ 0 & 0 & c_{\mathrm{S}} & 0 & 0 & 0 & -c_{\mathrm{S}} & 0 & 0 \end{bmatrix} \tag{6.3}$$

Upon partitioning the computational domain $\Omega \in \mathbb{R}^3$ into a set of conforming tetrahedral elements $\Omega \approx \cup_{m=1}^{N_{\mathrm{el}}} T_{\mathrm{m}}$, and approximating the components of the state vector u_p, $p = \overline{1,9}$, constrained to an element T_{m}, by a linear combination of the space-dependent polynomials of degree N, $\{\Phi_l^{(m)}(\boldsymbol{x})\}_{l=1}^{N_\Phi}$, $N_\Phi = (N+1)(N+2)(N+3)/6$, and the time-dependent degrees of freedom $\hat{u}_{pl}(t)$:

$$u_p(\boldsymbol{x},t)|_{T_{\mathrm{m}}} \approx u_p^h(\boldsymbol{x},t)|_{T_{\mathrm{m}}} = \Phi_l^{(m)}(\boldsymbol{x})\, \hat{u}_{pl}^{(m)}(t). \tag{6.4}$$

Rewriting (6.1) in index notation, multiplying it by test function Φ_k, and integrating over the element T_{m}:

$$\int_{T_{\mathrm{m}}} \Phi_k \frac{\partial u_p}{\partial t} \mathrm{d}V + \int_{T_{\mathrm{m}}} \Phi_k \left(A_{pq} \frac{\partial u_q}{\partial x} + B_{pq} \frac{\partial u_q}{\partial y} + C_{pq} \frac{\partial u_q}{\partial z} \right) \mathrm{d}V = \int_{T_{\mathrm{m}}} \Phi_k S_p \mathrm{d}V, \tag{6.5}$$

Further, integrating second term in (6.5) by parts yields

$$\begin{aligned} &\int_{T_{\mathrm{m}}} \Phi_k \frac{\partial u_p}{\partial t} \mathrm{d}V + \int_{\partial T_{\mathrm{m}}} \Phi_k F_p^h \mathrm{d}S \\ &- \int_{T_{\mathrm{m}}} \left(\frac{\partial \Phi_k}{\partial x} A_{pq} u_q + \frac{\partial \Phi_k}{\partial y} B_{pq} u_q + \frac{\partial \Phi_k}{\partial z} C_{pq} u_q \right) \mathrm{d}V = \int_{T_{\mathrm{m}}} \Phi_k S_p \mathrm{d}V, \end{aligned} \tag{6.6}$$

where numerical flux function $\boldsymbol{F}^h = \boldsymbol{F}^h[\boldsymbol{u}^h]$, detailed later, has been introduced to facilitate (possible) discontinuity of $\boldsymbol{u}^h$ at the interfaces between the elements. Note that without the additional surface integral affiliated with the numerical flux, the weak form (6.6) resembles conventional finite element framework in domain $\Omega = T_{\mathrm{m}}$.

6.2.1 Upwind numerical flux

The numerical flux function $\boldsymbol{F}^h$ is further defined with the aid of the exact Riemann solver for a linear hyperbolic system (6.1). An evolution problem with initial values that are piecewise constant, discontinuous across an interface, is called a Riemann problem [59]. Riemann problems are local, involving only the points immediately contiguous to the discontinuity interface. The explicit solution of a Riemann problem $\boldsymbol{u}^{\mathrm{G}}(\boldsymbol{u}^{\mathrm{L}}, \boldsymbol{u}^{\mathrm{R}})$ in terms of the "left" $\boldsymbol{u}^{\mathrm{L}}$ and "right" $\boldsymbol{u}^{\mathrm{R}}$ boundary data for the system (6.1) is given, e.g. in [66]. With the aid of the latter, the state at the interface between the adjacent tetrahedral elements m and m_j, $j = \overline{1,4}$ is defined via *upwinding* with the following expression of the numerical flux (also referred to as Godunov flux):

$$\boldsymbol{F}^h = \boldsymbol{F}^h[\boldsymbol{u}^{\mathrm{G}}(\boldsymbol{u}^{(m)}, \boldsymbol{u}^{(m_j)})] = \tfrac{1}{2} T \left(A + |A|\right) T^{-1} \boldsymbol{u}^{(m)} + \tfrac{1}{2} T \left(A - |A|\right) T^{-1} \boldsymbol{u}^{(m_j)}, \quad (6.7)$$

where $\boldsymbol{u}^{(m)}$ and $\boldsymbol{u}^{(m_j)}$ are the boundary extrapolated values of the numerical solution from the element m and its j-th side neighbor m_j, respectively. Matrix $T = T(\boldsymbol{n}, \boldsymbol{s}, \boldsymbol{t})$ and its inverse T^{-1} are the rotation matrices catering for transforming the state vector $\boldsymbol{u}$, respectively, from and to the face-aligned coordinate system equipped with an outward pointing norm vector $\boldsymbol{n}$ and a pair of tangential vectors, $\{\boldsymbol{s}, \boldsymbol{t}\}$, see [41] for details. Note that due to rotation to the face-aligned frame, in which $\boldsymbol{n} = \boldsymbol{e}_{\mathrm{x}}$, only matrix A is needed to compute the flux. The absolute value operator acting on A has a meaning of applying absolute value operator to the eigenvalues (6.2) of the matrix:

$$|A| = R^{\mathrm{A}} \operatorname{diag}(|\Lambda_1|, \ldots, |\Lambda_9|) \, (R^{\mathrm{A}})^{-1} \quad (6.8)$$

In this setting, the flux (6.7) describes both outgoing and incoming waves arising on the interface between the adjacent elements. Note that the flux function $\boldsymbol{F}^h$ takes as arguments both states – to the left and to the right of the intercell interface. One can show that (6.7) also corresponds to the expression derived in [69] using Rankine-Hugoniot jump conditions [e.g., 59] for a more general case of solid-fluid interaction, also exposed in [70]. Consistency and stability of numerical flux (6.7) are also proven in [69].

Splitting the boundary integral in (6.6) into the contributions from each face $j = \overline{1,4}$ of the parent tetrahedron T_{m}, and denoting $A^{\pm} = \frac{1}{2}\left(A \pm |A|\right)$, one arrives at a semi-discrete DG scheme describing evolution of degrees of freedom $\hat{u}_{pk}(t)$, $p = \overline{1,9}$, $k = \overline{1, N_\Phi}$

in each element T_{m}:

$$\begin{aligned}
&\frac{\partial \hat{u}_{pl}}{\partial t} \int_{T_{\mathrm{m}}} \Phi_k^{(m)}\, \Phi_l^{(m)}\, \mathrm{d}V \\
&+ \sum_{j=1}^{4} T_{pq}^{j} A_{qr}^{+} \left(T_{rs}^{j}\right)^{-1} \hat{u}_{sl}^{(m)} \int_{(\partial T_{\mathrm{m}})_j} \Phi_k^{(m)} \Phi_l^{(m)} \mathrm{d}S \\
&+ \sum_{j=1}^{4} T_{pq}^{j} A_{qr}^{-} \left(T_{rs}^{j}\right)^{-1} \hat{u}_{sl}^{(m_j)} \int_{(\partial T_{\mathrm{m}})_j} \Phi_k^{(m)} \Phi_l^{(m_j)} \mathrm{d}S \\
&- \left(A_{pq} \int_{T_{\mathrm{m}}} \frac{\partial \Phi_k^{(m)}}{\partial x}\, \Phi_l^{(m)}\, \mathrm{d}V + B_{pq} \int_{T_{\mathrm{m}}} \frac{\partial \Phi_k^{(m)}}{\partial y}\, \Phi_l^{(m)}\, \mathrm{d}V + C_{pq} \int_{T_{\mathrm{m}}} \frac{\partial \Phi_k^{(m)}}{\partial z} \Phi_l^{(m)}\, \mathrm{d}V \right) \hat{u}_{ql}^{(m)} \\
&= \int_{T_{\mathrm{m}}} \Phi_k^{(m)}\, S_p\, \mathrm{d}V,
\end{aligned} \tag{6.9}$$

where $(\partial T_{\mathrm{m}})_j$ denotes the j-th face of T_{m} endowed with rotation matrix T^j. It is noted here that employing hierarchical orthogonal shape functions $\{\tilde{\Phi}_l\}_{l=1}^{N_\Phi}$, given in [67], the mass matrix affiliated with the first term in (6.9) reduces to a diagonal matrix that can be inverted trivially.

6.2.2 External boundary conditions

A particular feature of DG methods, inherited from the finite volume methods, is the usage of numerical fluxes at element interfaces. To complete the IBVP (6.1) approximated via semi-discrete system (6.9), upwind numerical fluxes have to be also prescribed over the external boundary of the domain to accommodate physical boundary conditions. In this setting, one has to solve an inverse Riemann problem to define a missing state $\boldsymbol{u}^{\mathrm{R}}$ on the outside of the external boundary and thus the upwind flux (6.7) to (weakly) facilitate desired Godunov state $\boldsymbol{u}^{\mathrm{G}}$. Modeling wave propagation in the tested specimens (see Sec. 3) requires implementation of the two particular types of the boundary conditions: Neumann traction-free, and time-dependent Dirichlet boundary. In the context of DG modeling, the former can be implemented via the stress symmetry argument [40, 41]. In this setting, the numerical flux $\boldsymbol{F}_{\mathrm{N}}^{h}$ on the traction-free boundaries is given via:

$$\boldsymbol{F}_{\mathrm{N}}^{h} = \tfrac{1}{2} T \left(A + |A|\right) T^{-1} \boldsymbol{u}^{(m)} + \tfrac{1}{2} T \left(A - |A|\right) \Gamma T^{-1} \boldsymbol{u}^{(m)}, \tag{6.10}$$

where $\Gamma = \mathrm{diag}(-1,1,1,-1,1,-1,1,1,1)$ accounts for the mirroring of the normal and shear stresses of the state $\boldsymbol{u}^{(m)}$ with respect to the facet-aligned coordinate system. Numerical tests of (6.10) in the context of the Lamb's problem demonstrate good accuracy of this approach [40]. Using similar considerations, (6.10) can be extended to non-zero tractions on the boundary, see [69]. Two other types of boundary conditions that have been exposed in the context of solving the system of elasticity (6.1) with DG are the absorbing boundary conditions and the periodic boundary conditions [e.g., 41]. However, no illustration of implementing (time-dependent) Dirichlet boundary conditions in the context of elastic wave propagation could be found in the literature. At this stage to facilitate the numerical simulations, the following formula for the numerical flux, $\boldsymbol{F}^h_{\mathrm{D}}$, is implemented on the boundary with the Dirichlet data $\boldsymbol{u}^\star$:

$$\boldsymbol{F}^h_{\mathrm{D}} = \tfrac{1}{2} T \left(A + |A|\right) T^{-1} \boldsymbol{u}^{(m)} + \tfrac{1}{2} T \left(A - |A|\right) T^{-1} \begin{bmatrix} \boldsymbol{\sigma}^{(m)} \\ -\boldsymbol{v}^{(m)} + 2\dot{\boldsymbol{u}}^\star \end{bmatrix}. \tag{6.11}$$

It can be shown that the "left" and the "right" data in the flux (6.11) implement Godunov state $\boldsymbol{u}^{\mathrm{G}} = [\boldsymbol{\sigma}^{\mathrm{G}}, \boldsymbol{v}^{\mathrm{G}}]$ featuring $\boldsymbol{v}^{\mathrm{G}} = \boldsymbol{v}^\star = \dot{\boldsymbol{u}}^\star$. For completeness, the flux corresponding to absorbing boundary conditions is given here:

$$\boldsymbol{F}^h_{\mathrm{abs}} = \tfrac{1}{2} T \left(A + |A|\right) T^{-1} \boldsymbol{u}^{(m)}, \tag{6.12}$$

where the second term corresponding to incoming waves and endowed with matrix $A + |A|$ vanishes to facilitate radiation conditions.

6.3 Runge-Kutta time integration

Using appropriate quadrature rules, (6.9) can be assembled into a global multi degrees of freedom system:

$$M\dot{\boldsymbol{U}}(t) + F\boldsymbol{U}(t) - K\boldsymbol{U}(t) = \boldsymbol{S}(t), \tag{6.13}$$

where $\boldsymbol{U} = \left[[\hat{u}^{(1)}_{11}, \ldots, \hat{u}^{(1)}_{9N_\Phi}]^{\mathrm{T}}, \ldots, [\hat{u}^{(N_{\mathrm{el}})}_{11}, \ldots, \hat{u}^{(N_{\mathrm{el}})}_{9N_\Phi}]^{\mathrm{T}} \right]^{\mathrm{T}}$ and mass M, flux F, and stiffness K matrices are assembled from their element-local bilinear forms in (6.9), while the right-hand side vector $\boldsymbol{S}(t)$ is assembled from the linear form catering for the body forces. With reference to Sec. 6.2.2 the boundary conditions are accounted for via modification of the upwind flux functions in (6.6) when integrating over the external boundaries. In

this vein, it is convenient to split the flux over the Dirichlet boundaries (6.10) into two parts: $\boldsymbol{F}^h_{\mathrm{D}} = \boldsymbol{F}^h_{\mathrm{D},0} + \boldsymbol{F}^h_{\mathrm{D},1}$:

$$\begin{aligned} \boldsymbol{F}^h_{\mathrm{D},0} &= \tfrac{1}{2} T \left(A + |A|\right) T^{-1} \boldsymbol{u}^{(m)} + \tfrac{1}{2} T \left(A - |A|\right) T^{-1} \begin{bmatrix} \boldsymbol{\sigma}^{(m)} \\ -\boldsymbol{v}^{(m)} \end{bmatrix}, \\ \boldsymbol{F}^h_{\mathrm{D},1} &= T \left(A - |A|\right) T^{-1} \begin{bmatrix} 0 \\ \dot{\boldsymbol{u}}^{\star} \end{bmatrix}, \end{aligned} \tag{6.14}$$

in which case the term $\boldsymbol{F}^h_{\mathrm{D},0}$ (fixed boundary) contributes to the flux matrix F via corresponding bilinear form, while the term $\boldsymbol{F}^h_{\mathrm{D},1}$ yields a (time-dependent) linear form that contributes to the right-hand side $\boldsymbol{S}(t)$.

Semi-discrete system (6.13) can be integrated using conventional Runge-Kutta (RK) multi-stage schemes to achieve high-order approximation in time. Thanks to block-diagonal structure of the mass matrix M, inversion can be performed trivially block-by-block which is why explicit time integration schemes are commonly used in the DG framework, see [58]. However, as pointed out in [40], increasing the order of a RK scheme is reasonable only up to some limit given by Butcher barriers [71] that state that the efficiency of an explicit RK scheme drastically decreases if the order of the scheme is larger than 4. Another important constraint in this setting is the stability criterion embodied by the Courant-Friedrichs-Lewy (CFL) condition; some analysis of the maximum CFL number for various RK schemes can be found in [72]. In this matter, a third-order total variation diminishing RK (TVD-RK) scheme [42] is a good candidate for time integration of the semi-discrete system:

$$\begin{aligned} \boldsymbol{U}^{(1)} &= \boldsymbol{U}^{(0)} + \Delta t\, \boldsymbol{R}(\boldsymbol{U}^{(0)}, t^{(0)}), \\ \boldsymbol{U}^{(2)} &= \frac{3}{4}\boldsymbol{U}^{(0)} + \frac{1}{4}\boldsymbol{U}^{(1)} + \frac{1}{4}\Delta t\, \boldsymbol{R}(\boldsymbol{U}^{(1)}, t^{(0)} + \Delta t), \\ \boldsymbol{U}^{(3)} &= \frac{1}{3}\boldsymbol{U}^{(0)} + \frac{2}{3}\boldsymbol{U}^{(2)} + \frac{2}{3}\Delta t\, \boldsymbol{R}(\boldsymbol{U}^{(2)}, t^{(0)} + \frac{\Delta t}{2}), \end{aligned} \tag{6.15}$$

where $\boldsymbol{R}(\boldsymbol{U}(t), t) = M^{-1}\left(K\boldsymbol{U}(t) - F\boldsymbol{U}(t) + \boldsymbol{S}(t)\right)$. From preliminary runs, the minimal stable time step Δt_{stab} for this scheme was estimated at:

$$\Delta t_{\mathrm{stab}} = 0.085\, \frac{l_{\min}}{c_{\mathrm{P}}}, \tag{6.16}$$

in terms of $l_{\min} = 2r_{\min}$ – minimum diameter of the elements' inscribed spheres, and c_{P} – fastest velocity of the propagating waves.

6.4 Arbitrary high-order derivative time integration

Another time integration method that has been recently exploited in conjunction with the DG method is so-called ADER approach. Two main ingredients of the method are: i) expanding the solution to (6.1) in Taylor series with respect to the time variable, and ii) replacing the time derivatives in the expansion by a corresponding combination of the spatial derivatives via Cauchy-Kovalewski procedure. The ADER schemes were originally proposed in [73].

To proceed with performing high-order time integration of (6.9) it is more practical to work in a reference coordinate system $\{O;\xi,\eta,\zeta\}$ affiliated with the reference element $T_{\mathrm{r}}=\{(\xi,\eta,\zeta)\colon 0<\zeta<1 \wedge 0<\eta+\zeta<1 \wedge 0<\xi+\eta+\zeta<1\}$ and endowed with element-constant Jacobi transformation matrix $J^{(m)}$ catering for transforming coordinates from T_{m} to T_{r}:

$$J^{(m)}=\frac{\partial\boldsymbol{\xi}}{\partial\boldsymbol{x}}=\frac{\partial(\xi,\eta,\zeta)}{\partial(x,y,z)} \tag{6.17}$$

For brevity, index (m) is omitted in the further developments. Upon defining a linear combination of the Jacobian matrices in each element T_{m},

$$\begin{aligned} A^{\star} &= J_{11}A + J_{12}B + J_{13}C,\\ B^{\star} &= J_{21}A + J_{22}B + J_{23}C,\\ C^{\star} &= J_{31}A + J_{32}B + J_{33}C, \end{aligned} \tag{6.18}$$

equations (6.1) for $\boldsymbol{x}\in T_{\mathrm{m}}$ are transformed to the reference system:

$$\frac{\partial}{\partial t}\boldsymbol{Q}(\boldsymbol{\xi},t)+A^{\star}\frac{\partial}{\partial\xi}\boldsymbol{Q}(\boldsymbol{\xi},t)+B^{\star}\frac{\partial}{\partial\eta}\boldsymbol{Q}(\boldsymbol{\xi},t)+C^{\star}\frac{\partial}{\partial\zeta}\boldsymbol{Q}=\boldsymbol{F}(\boldsymbol{\xi},t), \tag{6.19}$$

where $\boldsymbol{Q}(\boldsymbol{\xi},t)=\boldsymbol{u}(\boldsymbol{x}(\boldsymbol{\xi}),t)$ and $\boldsymbol{F}(\boldsymbol{\xi},t)=\boldsymbol{S}(\boldsymbol{x}(\boldsymbol{\xi}),t)$, $\boldsymbol{\xi}\in T_{\mathrm{r}}$. Given here without a proof is the result of applying Cauchy-Kovalewski procedure to (6.19) in regard of computing k-th time derivative of $\boldsymbol{Q}(\boldsymbol{\xi},t)$ [40]:

$$\begin{aligned} \frac{\partial^k}{\partial t^k}\boldsymbol{Q}(\boldsymbol{\xi},t) =&(-1)^k\left(A^{\star}\frac{\partial}{\partial\xi}+B^{\star}\frac{\partial}{\partial\eta}+C^{\star}\frac{\partial}{\partial\zeta}\right)^k\boldsymbol{Q}(\boldsymbol{\xi},t)\\ &+\sum_{s=0}^{k-1}(-1)^s\left(A^{\star}\frac{\partial}{\partial\xi}+B^{\star}\frac{\partial}{\partial\eta}+C^{\star}\frac{\partial}{\partial\zeta}\right)^s\frac{\partial^{k-s-1}}{\partial t^{k-s-1}}\boldsymbol{F}(\boldsymbol{\xi},t). \end{aligned} \tag{6.20}$$

Next, the solution of (6.19) is developed via Taylor expansion up to order N:

$$\boldsymbol{Q}(\boldsymbol{\xi},t)\approx\sum_{k=0}^{N}\frac{t^k}{k!}\frac{\partial^k}{\partial t^k}\boldsymbol{Q}(\boldsymbol{\xi},0), \tag{6.21}$$

which, by virtue of (6.20) can be rewritten in the following way:

$$\boldsymbol{Q}(\boldsymbol{\xi},t) \approx \sum_{k=0}^{N} \frac{t^k}{k!} \left[(-1)^k \boldsymbol{L}^k \left[\boldsymbol{Q}(\boldsymbol{\xi},0) \right] + \sum_{s=0}^{k-1} (-1)^s \boldsymbol{L}^s \left[\frac{\partial^{k-s-1}}{\partial t^{k-s-1}} \boldsymbol{F}(\boldsymbol{\xi},0) \right] \right], \tag{6.22}$$

where a linear differential operator $\boldsymbol{L}[\boldsymbol{w}]$ acting on a state vector $\boldsymbol{w}=\boldsymbol{w}(\boldsymbol{\xi})$ is introduced as follows:

$$\boldsymbol{L}[\boldsymbol{w}] = \left(A^\star \frac{\partial}{\partial \xi} + B^\star \frac{\partial}{\partial \eta} + C^\star \frac{\partial}{\partial \zeta} \right) \boldsymbol{w}(\boldsymbol{\xi}). \tag{6.23}$$

For simplicity, it is assumed here that the right-hand side source term in (6.19) can be approximated by a distribution of N_S point sources in Ω, i.e.

$$\boldsymbol{S}(\boldsymbol{x},t) = \sum_{i=1}^{N_\mathrm{S}} \boldsymbol{S}_i(t)\, \delta(\boldsymbol{x}-\boldsymbol{x}_i), \tag{6.24}$$

where $\boldsymbol{S}_i(t)$ is a corresponding time dependence of source i located at $\boldsymbol{x}_i$. In this vein, the numerical model is also adapted for prescribing adjoint excitation, see in Sec. 3.5.4. Consider an element T_m containing one of the point sources. After transforming the spatial coordinates to the reference element T_r, the right-hand side of (6.19) takes the form $\boldsymbol{F}(\boldsymbol{\xi},t) = \boldsymbol{F}^s(t)\, \delta(\boldsymbol{\xi}-\boldsymbol{\xi}_s)$, where $\boldsymbol{\xi}_s$ is the location of the point source in the reference system of T_r, and $\boldsymbol{F}^s(t)$ – its corresponding time dependence. Assume also, that in each time step $[t^n, t^n+\Delta t]$, $\boldsymbol{F}^s(t)$ can be approximated by Legendre polynomial basis functions Ψ_l, $l=\overline{1, N_\Psi}$, i.e. in index notation:

$$F_p^s(\boldsymbol{\xi},t) = \hat{F}_{pl} \Psi_l(t)\, \delta(\boldsymbol{\xi}-\boldsymbol{\xi}_s) \qquad t \in [t^n, t^n+\Delta t] \tag{6.25}$$

By virtue of spatial approximation of the solution (6.4) and the assumptions above, (6.22) can be rewritten in index notation in the following way:

$$Q_p(\boldsymbol{\xi},t) \approx \sum_{k=0}^{N} \frac{t^k}{k!} \left[(-1)^k \left[L_{pq}^k \Phi_l \right](\boldsymbol{\xi})\, \hat{Q}_{ql}(0) + \sum_{s=0}^{k-1} (-1)^s \left[L_{pq}^s \Phi_n \right](\boldsymbol{\xi}_s)\, \frac{\partial^{k-s-1}}{\partial t^{k-s-1}} \Psi_m(0) \right], \tag{6.26}$$

where the components of a multi-index function $\left[L_{pq}^k \Phi_l\right](\boldsymbol{\xi})$ are computed based on (6.23) in a term-by-term fashion.

Approximating the reference solution $Q_p(\boldsymbol{\xi},t)$ similar to (6.4), (6.26) can be L^2-projected onto each of the basis spatial functions Φ_n and integrated in time within one time step:

$$\int_0^{\Delta t} \hat{Q}_{pl}(\tau)\mathrm{d}\tau = I_{plqm}(\Delta t)\hat{Q}_{qm}(0) + I^\mathrm{S}_{plqm}(\Delta t)\hat{F}_{qm}(0), \tag{6.27}$$

where the time-evolution 4-index entities I and I^{S} are introduced according to the following definitions:

$$
\begin{aligned}
I_{plqm}(\Delta t) &= \langle \Phi_n, \Phi_l \rangle_{T_{\mathrm{r}}}^{-1} \left\langle \Phi_n, \sum_{k=0}^{N} \frac{\Delta t^{(k+1)}}{(k+1)!} (-1)^k \left[L_{pq}^k \Phi_l \right] (\boldsymbol{\xi}) \right\rangle_{T_{\mathrm{r}}}, \\
I_{plqm}^{\mathrm{S}}(\Delta t) &= \langle \Phi_n, \Phi_l \rangle_{T_{\mathrm{r}}}^{-1} \left\langle \Phi_n, \sum_{k=0}^{N} \frac{\Delta t^{(k+1)}}{(k+1)!} \sum_{s=0}^{k-1} \left[L_{pq}^s \Phi_n \right] (\boldsymbol{\xi}_s) \frac{\partial^{k-s-1}}{\partial t^{k-s-1}} \Psi_m(0) \right\rangle_{T_{\mathrm{r}}},
\end{aligned}
\tag{6.28}
$$

where $\langle \cdot, \cdot \rangle_{T_{\mathrm{r}}}$ denotes a dot product in the reference element T_{r}.

Finally, upon integrating in time (6.6), the ADER scheme can be obtained that provides an explicit single-step algorithm to update solution $\hat{Q}_{pk}^{(m)}$ in element T_{m} from time step t^n to t^{n+1}:

$$
\begin{aligned}
&\mathcal{M}_{kl} \left[\left(\hat{Q}_{pl}^{(m)} \right)^{n+1} - \left(\hat{Q}_{pl}^{(m)} \right)^{n} \right] \\
&+ \sum_{j=1}^{4} T_{pq}^j A_{qr}^+ \left(T_{rs}^j \right)^{-1} \left(\frac{|S_j|}{|J|} \right) \mathcal{F}_{kl}^{j,0} \left(I_{plqm}(\Delta t) \left(\hat{Q}_{qm}^{(m)} \right)^{n} + I_{plqm}^{\mathrm{S}}(\Delta t) \left(\hat{F}_{qm}^{(m)} \right)^{n} \right) \\
&+ \sum_{j=1}^{4} T_{pq}^j A_{qr}^- \left(T_{rs}^j \right)^{-1} \left(\frac{|S_j|}{|J|} \right) \mathcal{F}_{kl}^{j,i} \left(I_{plqm}(\Delta t) \left(\hat{Q}_{qm}^{(m_j)} \right)^{n} + I_{plqm}^{\mathrm{S}}(\Delta t) \left(\hat{F}_{qm}^{(m_j)} \right)^{n} \right) \\
&- \left(A_{pq}^\star \mathcal{K}_{kl}^\xi + B_{pq}^\star \mathcal{K}_{kl}^\eta + C_{pq}^\star \mathcal{K}_{kl}^\zeta \right) \left(I_{plqm}(\Delta t) \left(\hat{Q}_{qm}^{(m)} \right)^{n} + I_{plqm}^{\mathrm{S}}(\Delta t) \left(\hat{F}_{qm}^{(m)} \right)^{n} \right) \\
&= \Phi_k(\boldsymbol{\xi}_s) \int_{t^n}^{t^{n+1}} F_p^s(t) \mathrm{d}t,
\end{aligned}
\tag{6.29}
$$

with the reference element matrices (see explicit expressions for 2D case and hierarchical orthogonal basis functions $\tilde{\Phi}$ in [61]):

$$
\begin{aligned}
\mathcal{M}_{kl} &= \langle \Phi_k, \Phi_l \rangle_{T_{\mathrm{r}}}, \\
\mathcal{K}_{kl}^\xi &= \left\langle \frac{\partial \Phi_k}{\partial \xi}, \Phi_l \right\rangle_{T_{\mathrm{r}}}, \\
\mathcal{K}_{kl}^\eta &= \left\langle \frac{\partial \Phi_k}{\partial \eta}, \Phi_l \right\rangle_{T_{\mathrm{r}}}, \\
\mathcal{K}_{kl}^\zeta &= \left\langle \frac{\partial \Phi_k}{\partial \zeta}, \Phi_l \right\rangle_{T_{\mathrm{r}}}, \\
\mathcal{F}_{kl}^{j,0} &= \int_0^1 \Phi_k^{(m)}(\boldsymbol{\xi}(\chi_j)) \, \Phi_l^{(m)}(\boldsymbol{\xi}(\chi_j)) \, \mathrm{d}\chi_j, \\
\mathcal{F}_{kl}^{j,i} &= \int_0^1 \Phi_k^{(m)}(\boldsymbol{\xi}(\chi_j)) \, \Phi_l^{(m_j)}(\boldsymbol{\xi}(\chi_j)) \, \mathrm{d}\chi_j,
\end{aligned}
\tag{6.30}
$$

where the index $i = \overline{1,4}$ reflects four various mutual facet orientations on the (m)-(m_j) interface in the physical system $\{O; x, y, z\}$. $|J|$ and $|S_j|$ denote the Jacobians arising, respectively, in the volume and surface integrals in (6.6) after transforming to the reference system of T_r. Since matrices in (6.30) can be computed analytically and stored, the method is quadrature-free. Commonly adopted in the context of ADER-DG treatment are hierarchical modal shape functions [67] based on orthogonal Dubiner basis. With the latter, mass matrix in (6.30) is diagonal rendering the inversion trivial and saving computational time. Temporal evolution $\left(Q_{pk}^{(m)}\right)^n \rightarrow \left(Q_{pk}^{(m)}\right)^{n+1}$ in (6.29) is performed locally in the element (m) given i) (if nonzero) the values of the body forces in the element in terms of $\int_{t^n}^{t^{n+1}} \boldsymbol{F}^s(t)\,\mathrm{d}t$ and $\hat{F}_{qm}^{(m)}$, and its neighbors in terms of $\hat{F}_{qm}^{(m_j)}$, and ii) the solution at the previous time step in the adjacent elements in terms of $\left(\hat{Q}_{qm}^{(m_j)}\right)^n$. In this setting, no global assembly is required for ADER-DG time integration, whereas the solution in each element can be updated locally.

As pointed in [40, 41], the stability criterion for the ADER-DG scheme can be estimated as:

$$\Delta t_\mathrm{stab} = \frac{C_\mathrm{CFL}}{2N+1}\,\frac{l_\mathrm{min}}{c_\mathrm{P}}, \tag{6.31}$$

where N – order of the scheme (in terms of spatial and temporal approximation), and $C_\mathrm{CFL} < 0.7$ is required for stability. In practice, $C_\mathrm{CFL} = 0.5$ is usually adopted, which at $N = 3$ is about 15 % lower than the corresponding criterion of the RK time integration (6.16).

6.5 2D test numerical simulations with ADER-DG

To verify the ADER-DG scheme, a 2D version of the presented algorithm was first implemented in a serial code using Matlab. Matrices (6.30) were computed exactly for polynomials up to order 9 with the aid of symbolic calculus in Mathematica. In order to exercise the ADER-DG method and assess the numerical error of the long range wave propagation, fundamental solution test was set up similar to Sec. 4.1. On taking the excitation wavelet $s(t)$ as in Fig. 3.3 with $f_\mathrm{c} = 10$, 20, 30, 40 kHz, the numerical approximation of $\boldsymbol{u}^s$ is computed by discretizing the "test" circular domain Ω^test of radius $R^\mathrm{test} = 2$ m with triangular elements as shown in Fig. 6.1 so that $\kappa = 1.2$, 0.6, 0.4, 0.3, respectively. Here, material properties of the domain are taken the same as in a graphite

(see Table 3.2). The flux on the external edges of the outer triangles (marked green in the figure) was prescribed following (6.12). Thus computed numerical wavefields can be compared to the analytical solution obtained via convolution with the impulse response function (see Sec. 4.1. In the simulations, the time step was selected according to the stability limit (6.31) with $C_{\text{CFL}}=0.4$. Figure 6.2 shows the snapshots of the simulated waveforms in terms of horizontal velocity v_1 taken in the frame $[0,1]\times[0,1]$ and computed at $t=0.5\,\text{ms}$. Note the pronounced effect of numerical attenuation of the wavefields when simulating high-frequency waveforms ($\kappa<0.5$) with polynomials of low order ($N<6$). For completeness, Fig. 6.3 presents the comparison of the time signals of displacement $u_1(\boldsymbol{\xi}^{\text{test}})$, $\boldsymbol{\xi}^{\text{test}}=(1.5,0)$ simulated with $\mathcal{P}8$ interpolation and its analytical counterpart for $\kappa=0.4$ and $\kappa=0.6$ corresponding to $|\boldsymbol{\xi}^{\text{test}}|=11.2\,\lambda_{\text{P}}$ and $|\boldsymbol{\xi}^{\text{test}}|=16.7\,\lambda_{\text{P}}$ respectively. As seen from the displays, high-order interpolation in space and time of the ADER-DG approach allows very accurate transient wave propagation even when the resolution of the mesh is very coarse. Note higher accumulated error in the time signal affiliated with shorter S-wave in case $\kappa=0.4$. Given the results of the test simulations, it might be concluded that when dealing with long range propagation ($\geq 10\,\lambda_{\text{P}}$), $\kappa>0.5$ spatial discretization coupled with $\mathcal{P}8$ interpolation is expected to produce accurate results. An estimate of the efficiency gain of the ADER-DG approach with respect to originally adopted Newmark-CG scheme is intricate since ADER-DG provides a solution to both the physical variable (particle velocity) and its derivative (stress) while the latter only solves for displacements and additional effort is required to evaluate the stresses. Roughly one can say that in two dimensions the number of degrees of freedom per scalar field variable is the same for the case of DG-$\mathcal{P}8$ discretization with $\kappa=0.5$ and CG-$\mathcal{P}1$ discretization with $\kappa=12$.

6.6 Parallel implementation of DG method in 3D

In 3D applications the number of degrees of freedom in a high-order DG method is high even in case of coarse meshes. For example, to simulate 20 kHz wavefield in the graphite block discretized with a structured mesh of tetrahedra of one dominant wavelength in size, i.e. with $\kappa=1$, one needs approximately 1350 elements. With $\mathcal{P}8$ interpolation, each element contains $9\cdot N_{\Phi}=1485$ degrees of freedom, where factor 9 caters for 6 stress

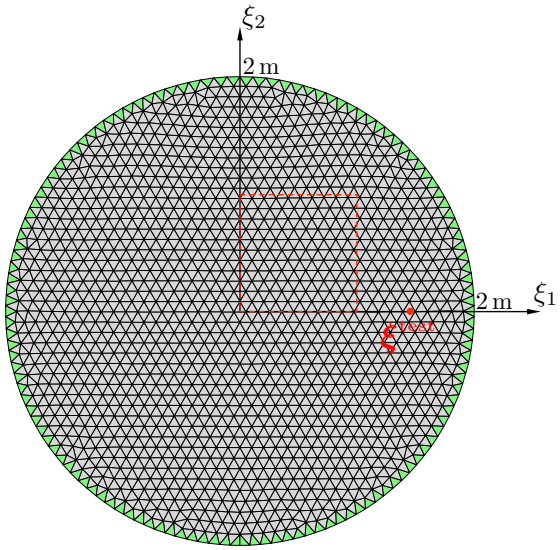

Figure 6.1: Test circular domain Ω^{test} discretized with triangular elements. Marked in green are the triangles containing external edges where the flux is prescribed via (6.12). Red dot marks the location of the test point $\boldsymbol{\xi}^{\text{test}}$.

and 3 velocity fields. In total, one arrives at $N_{\text{DOF}} \approx 2 \cdot 10^6$ DOFs which is already quite a challenge for a regular desktop machine. At 40 kHz the number of elements increases to about 11400 resulting in $N_{\text{DOF}} \approx 15 \cdot 10^6$ DOFs. Another computational impediment of high-order ADER-DG scheme is restrictive stability criterion in terms of the maximum time step (6.31) that is proportional to the minimal size (diameter of an inscribed ball) of the elements in the mesh. Assuming structured mesh with $\kappa = 1$, simulation of wave propagation in the graphite block with $\mathcal{P}8$ to the final time $T = 6\,\ell/c_{\text{P}} = 0.8$ ms at $f_{\text{c}} = 20$ kHz and $f_{\text{c}} = 40$ kHz requires 4100 and 8300 time steps respectively. In practice, however, structured meshes are rarely used due to inherent issues related to discretization of fine geometrical features. Indeed, the boundary conditions adopted for the graphite block during the experimental stage (see Sec. 3.5.4) and their implementation in the context of DG modeling through numerical fluxes over the external facets (see Sec. 6.2.2) require much smaller elements ($\kappa \ll 1$) near the transducer's impact patch to facilitate accurate modeling of the excitation. In this manner, these elements may significantly increase the number of time steps and render computational time impractical. Note that this issue is even more pronounced in case of Runge-Kutta time integration

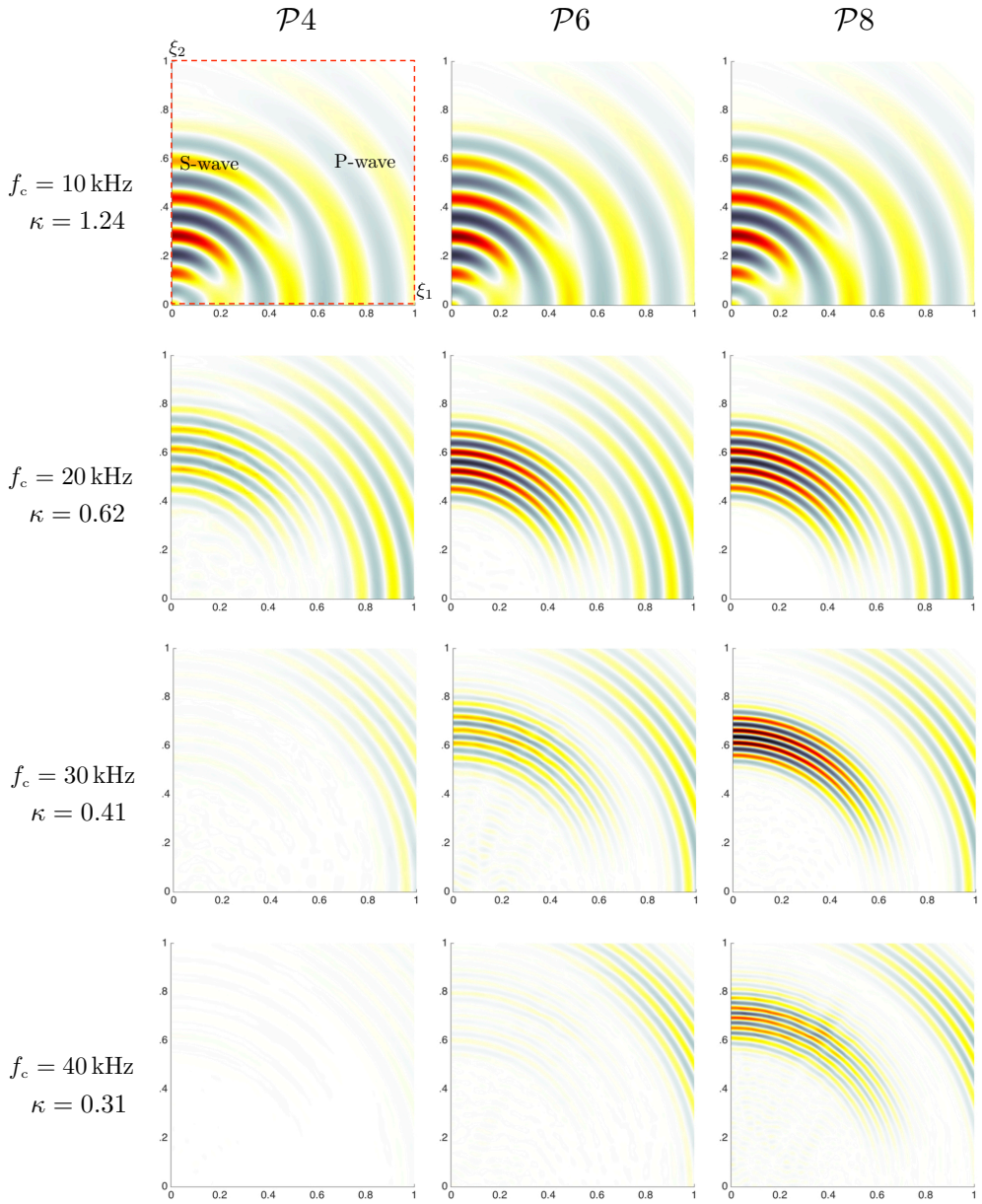

Figure 6.2: Test simulation of the fundamental solution test simulations with ADER-DG at different levels of the h- and p- discretizations.

due to additional effort affiliated with substage integrating. To mitigate the computational cost, local time integration [74] can be implemented in the context of ADER-DG approach in which case each element updates its state according to its local stable time

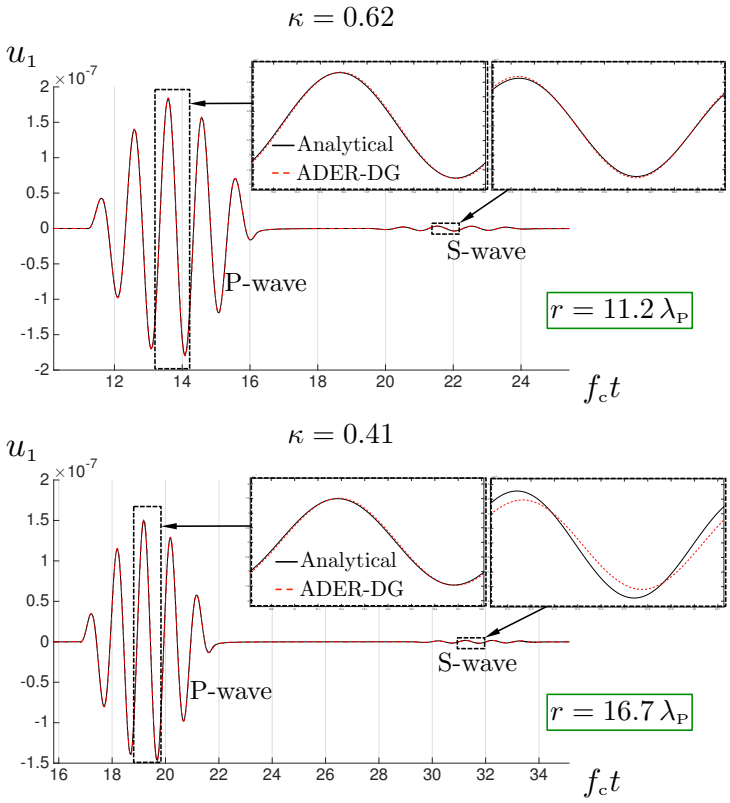

Figure 6.3: Test simulation of the fundamental solution with ADER-DG endowed with $\mathcal{P}8$ polynomials.

step while thus induced asynchronization is accounted for by virtue of ADER time integration.

On the other hand, parallel implementation of the code is often utilized in the context of DG technique to accelerate the computations. To test the parallel scalability of the DG method, preliminary tests were run using the FEniCS package with METIS mesh partitioning tool enabled. Distribution of the task and communication between the processing cores in FEniCS is implemented via Message Passing Interface (MPI). The tests were run both on a multicore desktop machine equipped with two quad-core processors and 32 GB of memory and a High Performance Computer (Itasca cluster) at the Minnesota Supercomputing Institute. The global matrices M, K, and F were assembled for a mesh with 10^4 $\mathcal{P}3$-elements and distributed between the cores of a preselected pool for a system of total $N_{\mathrm{DOF}} = 1.9 \cdot 10^6$ degrees of freedom. At this stage,

only nodal Lagrange-type shape functions are supported by DG elements in FEniCS rendering the mass matrix block-diagonal. Mass matrix inversion was performed using Conjugate Gradient iterative solver endowed with block-Jacobi parallel preconditioner. The global CPU time was measured for i) parallel assembly procedure of the mass, stiffness, and flux matrices, and ii) parallel solution of the system $M\boldsymbol{U} = (K - F)\,\boldsymbol{R}$ with randomly-generated data $\boldsymbol{R}$. Figure 6.4 shows the resulting graph of measured CPU time versus number of cores in the MPI pool. As seen from the display, the time required for global assembly (red curve) reduces almost linearly with increased number of cores both on the desktop machine and on the HPC cluster yielding scaling with efficiency of about 82 % at 8 cores. On the other hand, the speed-up of the solution of the linear system (black curve) is much less pronounced with efficiency of scaling quickly dropping with increasing number of cores and yielding the value of about 46 % at 8 cores. Poor scaling in the latter case is attributed to major losses on the communication time between the cores for this relatively small problem. Since communications between the cores are performed via the facets of the elements, an estimate of the scaling efficiency might be deduced from the average volume-to-area ratio of the mesh partitions.

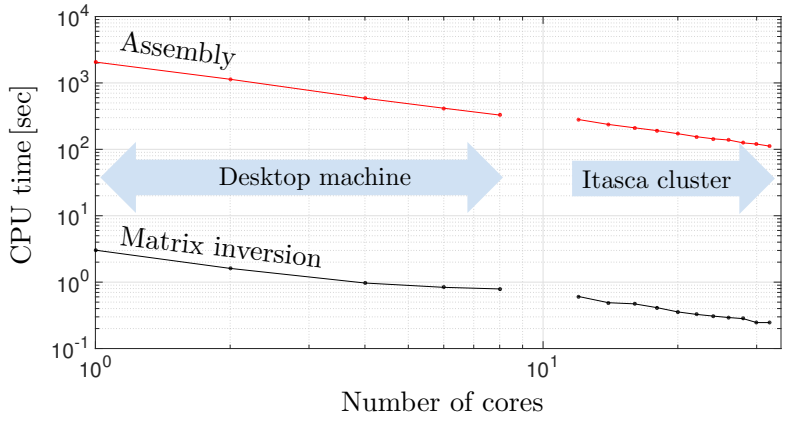

Figure 6.4: CPU time decrease with an increasing number of cores in parallel computation with DG-$\mathcal{P}3$ method.

6.7 TS imaging in a graphite block using DG computational platform

As mentioned in Sec. 5.5, quantifying the error of TS imaging in the experimental setting is problematic due to variety of the sources of possible error. One possible way to shed some light on this problem is to compare the results of reconstruction in an experimental and synthetic frameworks. To this end, the synthetic experiment was set up with newly established DG computational platform. The basis of the numerical experiment is an actual SLDV test of the block performed at $f_c = 20\,\text{kHz}$ with transducer located in position 1, see Fig. 3.9. Two tetrahedral meshes of the block, mounting i) reference domain, and ii) "damaged" domain encapsulating true B_{void}, were generated, see Fig. 6.5. Both meshes featured element-to-wavelength ratio $\kappa \simeq 1.6$. Note that to reduce the total number of elements and avoid very small elements strongly affecting the global CFL condition (6.16) the circular void in the second mesh is approximated by a diamond-shaped cavity.

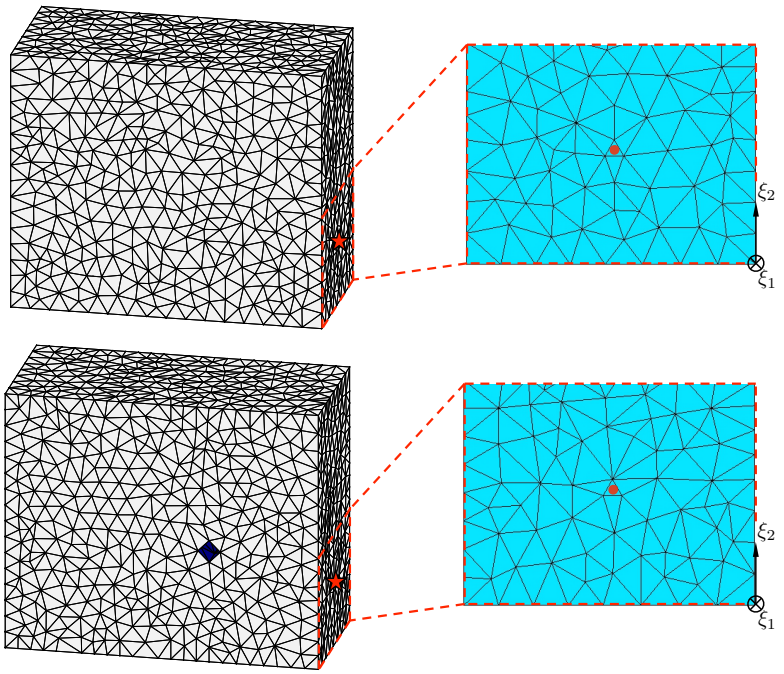

Figure 6.5: Reference (top) and "defective" (bottom) tetrahedral meshes of the graphite block featuring 10456 and 11681 elements respectively.

To evaluate the free and true fields, physical excitation of the block was modeled by prescribing numerical flux (6.11) over the external facet corresponding to the location of the transducer during the actual testing, see the right panel of Fig. 6.5, with $\boldsymbol{v}^\star$ replaced by SLDV data obtained in the corresponding scan point. The rest of the external facets were treated with traction-free fluxes (6.10). Virtual excitation of the adjoint state in terms of point forces $\boldsymbol{f}$ prescribed in the locations of the SLDV measurement points (see Fig. 3.9d) was computed by substituting the experimental SLDV data with synthetic data obtained from the true field simulation. The trivial Dirichlet boundary conditions in the adjoint state were accordingly prescribed via flux (6.11) with $\boldsymbol{v}^\star = 0$.

To save computational time, the true, free, and adjoint fields were computed using DG-$\mathcal{P}3$ method coupled with three-stage RK time integration. Simulations were run in parallel on Itasca cluster using 3 computational nodes and 24 cores. The resulting topological sensitivity reconstruction map $\tilde{\mathsf{T}}_{0.5}$ evaluated on the free and synthetic adjoint field data is presented in Fig. 6.6. To facilitate the analysis of the quality of imaging, reconstruction maps presented in this section are sampled using dense three-dimensional grid $\boldsymbol{\xi}^{\text{grid}} = \{(p\text{s}, q\text{s}, r\text{s}) : \ p, q, r \in \mathbb{Z}\}$ spaced at $\text{s} = 2\,\text{mm}$. Sampling is performed over the region $\Omega^{\text{TS}} = [d_{\text{sp}}, W - d_{\text{sp}}] \times [d_{\text{sp}}, H - d_{\text{sp}}] \times [-D, -d_{\text{sp}}]$ with $d_{\text{sp}} = 35\,\text{mm}$, where W, H, and D denote the width, height, and depth of the block denoted previously. On the display, the three-dimensional map is presented in terms of a general 3D view and two orthographic projections producing a view from the right (right panel), and a view from the top (bottom panel), see also Fig. 3.9.

As seen from the display, single-source TS reconstruction map provides sufficiently good evidence of the presence of a void defect in the block under the conditions of a synthetic experiment. By taking the result of imaging in synthetic conditions as benchmark, TS reconstruction maps are next evaluated using as input the actual SLDV data. In this vein, the adjoint field was re-evaluated using $\mathcal{P}3$ interpolation and the same reference mesh (see Fig. 6.5) and the new TS function was computed utilizing the available free field data. Accordingly, Fig. 6.7 plots the reconstruction map using the established post-processing framework. As seen from the display, the quality of reconstruction in the experimental setting is significantly reduced and almost all evidence of the presence of the void defect is lost. In order to facilitate discussion on the impact of the numerical error in the simulations, free and adjoint fields were recalculated using higher order

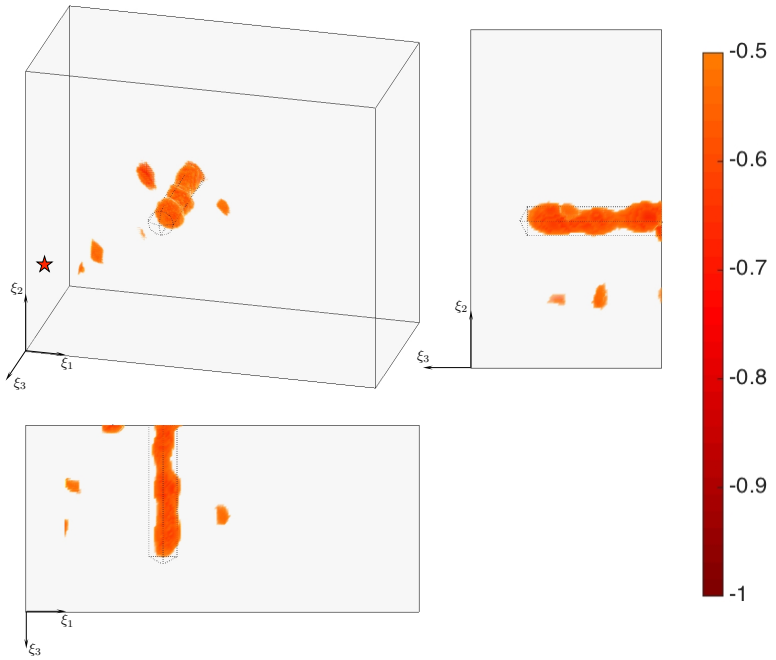

Figure 6.6: Synthetic single-source reconstruction map $\tilde{\mathsf{T}}_{0.5}$ obtained in graphite block at excitation frequency $f_{\mathrm{c}}=20\,\mathrm{kHz}$ with transducer located at position 1, duration $T=6\,\ell/c_{\mathrm{P}}$.

polynomial interpolation $\mathcal{P}4$ on the same spatial mesh. In this setting, Fig. 6.8 plots the reconstruction map evaluated on the new dataset. By comparing the maps in Figs. 6.7, 6.8, virtually no change in the distribution of TS function can be observed when accuracy of the numerical scheme is improved which suggests that the major source of error in the evaluated TS distributions is not related to numerical dispersion/attenuation in the simulated wavefields.

In an effort to detect a dominant source of error in the evaluated TS function, $\mathcal{P}3$ simulations of the free and adjoint fields were performed using an alternative reference mesh, see Fig. 6.9, in which the external facet corresponding to the location of the excitation patch was reduced in size to better represent the physical impact of the transducer. Computed in this setting reconstruction map, presented in Fig. 6.10, displays some change in terms of distribution of the spurious artifacts, however no important improvement in terms of shape/size of the minimum in vicinity of B_{void} can be observed. For completeness, the reconstruction map was also re-evaluated employing previously adopted CG computational platform with reference mesh featuring 5251020 elements

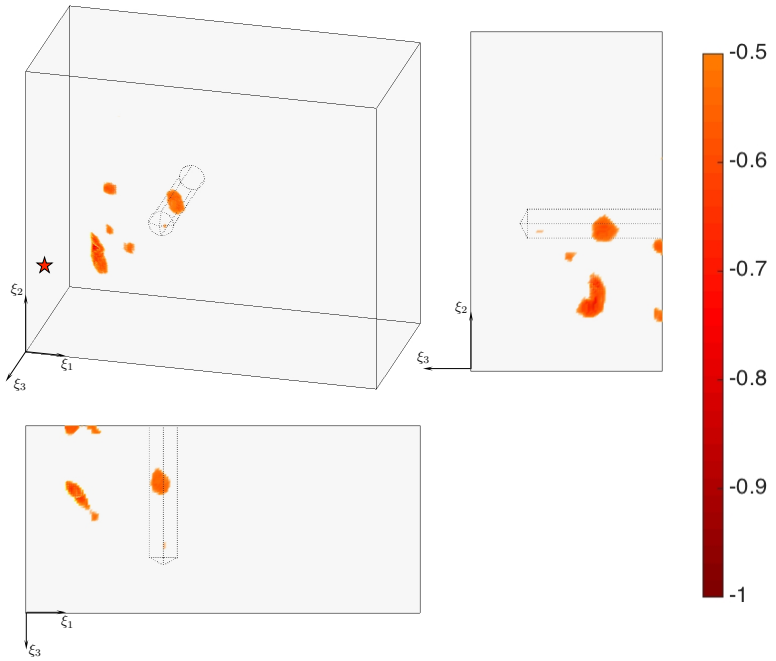

Figure 6.7: Experimental reconstruction map $\tilde{\mathsf{T}}_{0.5}$ evaluated using DG-$\mathcal{P}3$ simulations on a reference mesh containing 10456 elements.

($\kappa = 12$), see Fig. 6.11. Computed reconstruction map is presented in Fig. 6.12. By comparing Figs. 6.12 and 6.10, somewhat similar artifact pattern can be observed on both reconstruction maps, suggesting that the major error in the evaluated TS distributions likely is not related to the numerical treatment of the wave propagation, but rather is attributed either to the uncertainties in the mathematical model, or experimental noise in the SLDV data.

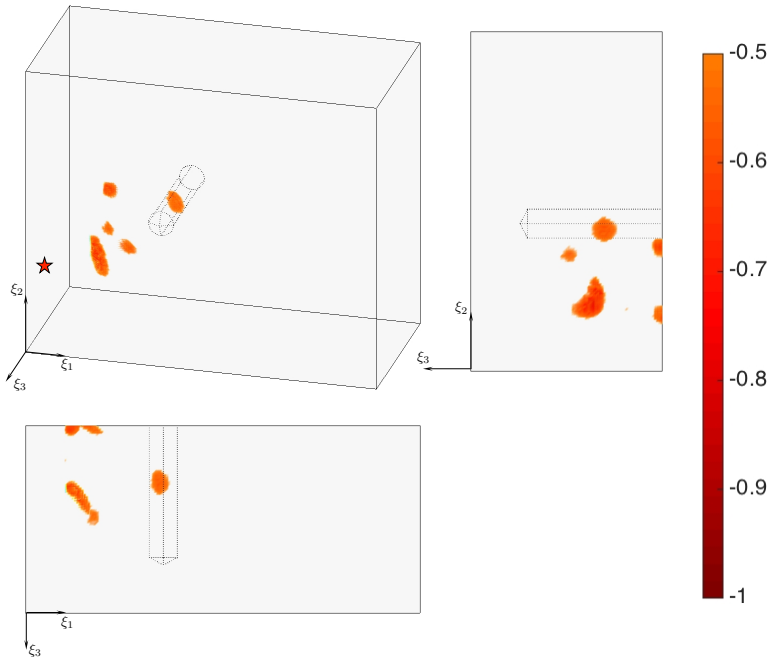

Figure 6.8: Experimental reconstruction map $\tilde{\mathsf{T}}_{0.5}$ evaluated using DG-$\mathcal{P}4$ simulations on a reference mesh containing 10456 elements.

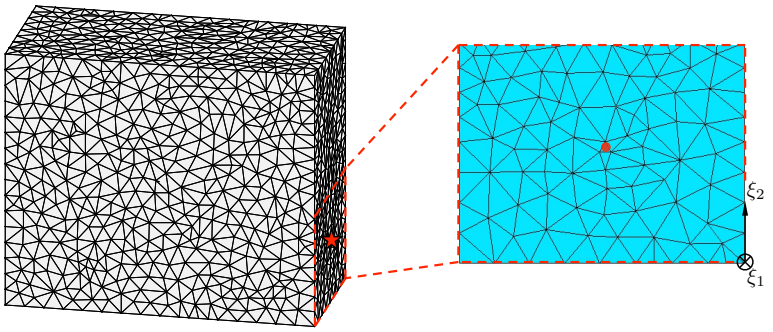

Figure 6.9: Reference mesh of the graphite block featuring 14771 elements.

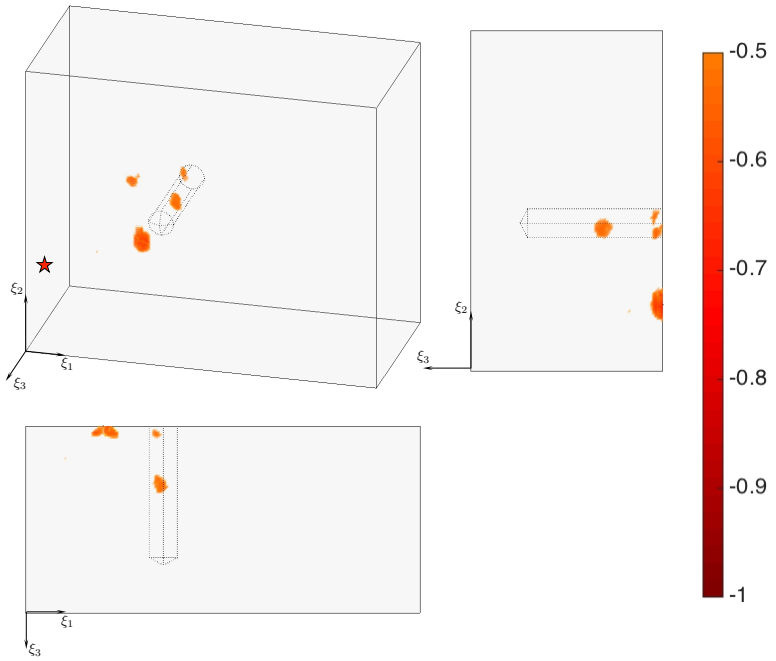

Figure 6.10: Experimental reconstruction map $\tilde{\mathsf{T}}_{0.5}$ evaluated using DG-$\mathcal{P}3$ simulations on a reference mesh containing 14771 elements.

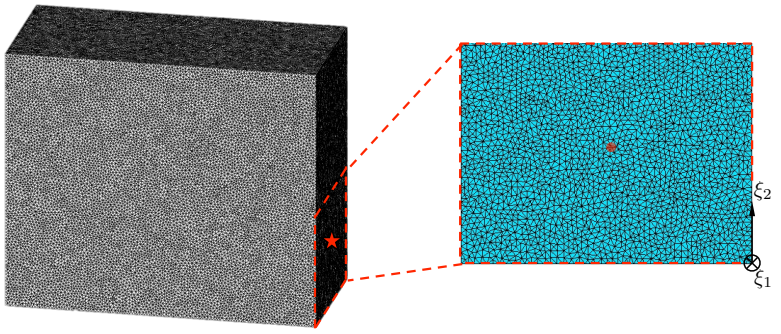

Figure 6.11: Reference mesh of the graphite block featuring 5251020 elements, utilized for computations with CG framework.

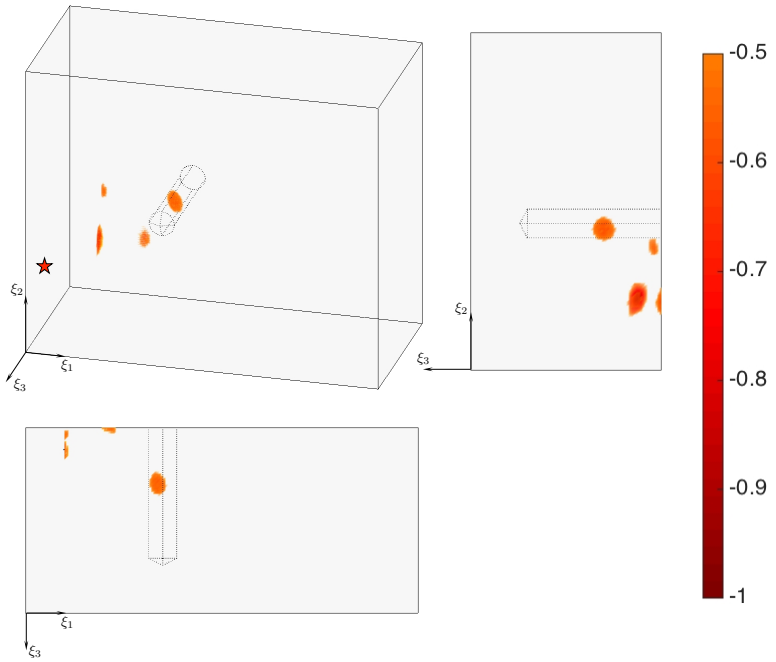

Figure 6.12: Experimental reconstruction map $\tilde{\mathsf{T}}_{0.5}$ evaluated using CG computational platform on a reference mesh with 5251020 elements.

Chapter 7

Conclusions

In this study, the method of topological sensitivity (TS) is applied experimentally toward non-iterative, full-waveform reconstruction of discrete cavities in i) aluminum plate, ii) graphite plate, and iii) graphite block from the boundary observations of transient elastodynamic fields scattered by the defects. To this end, the specimens are excited via a piezoceramic transducer while remotely monitoring the induced two-dimensional in-plane (plates) and three-dimensional (block) motion, in terms of particle velocity, by way of a 3D Scanning Laser Doppler Vibrometer (SLDV).

On the analytical front, the TS analysis is formulated for generality within two alternative frameworks, catering respectively for the sensory data in the form of particle displacement and particle velocity. It is also shown that the use of a smoothing temporal windowing function in specifying the L2-norm misfit between the model and the data (that forms the basis for the TS formulation) is essential from both theoretical and computational points of view.

On establishing the suitability of the plane stress approximation for the forward problem, a computational platform for obstacle reconstruction in the aluminum plate specimen is developed on the basis of i) 2D FE method with carefully tuned spatiotemporal discretization, and ii) Blackman-type temporal window as a tool to regularize the TS evaluation. In this setting the computed TS maps are shown, via their local minima, to be in good agreement with the geometry of the dual (void-and-slit) defect. The experimental investigation is further conducted to expose the effect of key problem parameters on the quality of obstacle reconstruction such as the (dominant) excitation

frequency, the source aperture, and the duration of the temporal record. Considering the sensitivity of TS maps to the rate of excitation, it was found (consistent with previous numerical studies) that the TS aids obstacle reconstruction via two distinct modes, namely by taking pronounced negative values (i) inside the obstacle at lower excitation frequencies, and (ii) in the neighborhood of its boundary at higher excitation frequencies. On the other hand, increases in the source aperture and duration of the recording interval were found to generally better the obstacle reconstruction, with caveats such that stem from the adverse effect of numerical dissipation plaguing the forward model. To provide a link with previous studies, the investigation also includes a comparison between the TS method and its reductions (proposed elsewhere in the literature) as obstacle reconstruction tools. The results suggest that for the germane class of experimental configurations, the use of pristine TS indicator furnishes the most consistent output.

With the experimental testing platform and computational framework established with the aid of testing on an aluminum plate, the study proceeded with an experimental imaging of material damage in nuclear graphite. Ultrasound tests were first conducted to validate isotropic behavior and determine elastic material constants of graphite. The results of experimental imaging in graphite plate revealed failure of the method to reconstruct the geometry of the void defect at higher excitation rates and larger durations of the recording interval due to insufficient accuracy of the adopted plane stress approximation.

As for testing in a more realistic 3D setting, the SLDV tests were next performed in a graphite block after adopting a modified physical excitation procedure to simplify the simulation of germane boundary conditions. Here, TS imaging is examined in a challenging scenario of limited excitation and motion sensing apertures. In this setting, synthetic imaging was first performed by virtue of replacing the SLDV observations data with numerically simulated data obtained by adopting an appropriate 'true' field model. Computed in this manner TS distributions show excellent agreement with the geometry of the void defect provided that the duration of the recording interval is set relatively long. From the experimental imaging point of view, however, the TS maps computed in similar testing configurations were shown to be highly polluted with near-boundary spurious minima strongly deteriorating the reconstruction of the true defect.

To help combat the major source of error in the experimental TS maps of a graphite block, the last chapter of this study makes an attempt to improve the accuracy of numerical simulations of wave propagation with the aid of a recently developed discontinuous Galerkin (DG) treatment. By virtue of comparing the TS distribution obtained via the new computational platform with its synthetic counterpart, it was found that the major source of error in the evaluated TS map is not (anymore) related to the numerical dispersion/attenuation error accumulating in the propagating wavefields. On the basis of identifying possible sources of error in the experimental TS imaging, an assumption is made concerning possible errors in the adopted mathematical model of elastic wave propagation in graphite including uncertainties in the modeling of boundary conditions and measured elastic moduli. In terms of future developments, it is recommended that the research continues in direction of identifying further the significant sources of reconstruction error.

References

[1] A. Tarantola. Linearized inversion of seismic reflection data. *Geophys. Prospecting*, 32:998–1015, 1984.

[2] N. Bleistein, J.K. Cohen, and J.W. Stockwell, Jr. *Mathematics of Multidimensional Seismic Imaging, Migration, and Inversion*. Springer-Verlag, New York, 2001.

[3] M. Bonnet and B. Guzina. Elastic-wave identification of penetrable obstacles using shape-material sensitivity framework. *J. Comp. Phys.*, 228:294–311, 2009.

[4] J Virieux and S Operto. An overview of full-waveform inversion in exploration geophysics. *Geophysics*, 74:WCC1–WCC26, 2009.

[5] D. Colton and A. Kirsch. A simple method for solving inverse scattering problems in the resonance region. *Inverse Problems*, 12:383–393, 1996.

[6] D. Colton, J. Coyle, and P. Monk. Recent developments in inverse acoustic scattering theory. *SIAM Review*, 42:369–414, 2000.

[7] A. Kirsch and N. Grinberg. *The Factorization Method for Inverse Problems*. Oxford University Press, Oxford, UK, 2007.

[8] D. Colton and H. Haddar. An application of the reciprocity gap functional to inverse scattering theory. *Inverse Problems*, 21:383–398, 2005.

[9] R. Potthast. *Point Sources and Multipoles in Inverse Scattering Theory*. Chapman & Hall/CRC, New York, 2001.

[10] A.J. Devaney. *Mathematical Foundations of Imaging, Tomography and Wavefield Inversion*. Cambridge University Press, Cambridge, UK, 2012.

[11] D. Cassereau, F. Wu, and M. Fink. Limits of self-focusing using closed time-reversal cavities and mirrors-theory and experiment. In *Proc. IEEE Ultrasonics Symposium*, pages 1613–1618, 1990.

[12] C. Prada and M. Fink. Eigenmodes of the time reversal operator: A solution to selective focusing in multiple-target media. *Wave Motion*, 20:151–163, 1994.

[13] M. S. Vogelius, D. J. Cedio-Fengya, and S. Moskow. Identification of conductivity imperfections of small diameter by boundary measurements. Continuous dependence and computational reconstruction. *Inverse Problems*, 14:553–595, 1998.

[14] H. Ammari and H. Kang. *Reconstruction of Small Inhomogeneities from Boundary Measurements*. Springer, Berlin, New York, 2004.

[15] E.A. Marengo, F.K. Gruber, and F. Simonetti. Time-reversal MUSIC imaging of extended targets. *IEEE Trans. on Image Processing*, 16:1967–1984, 2007.

[16] D. Givoli. Time reversal as a computational tool in acoustics and elastodynamics. *J. Comp. Acous.*, 22:1430001, 2014.

[17] B. B. Guzina and M. Bonnet. Topological derivative for the inverse scattering of elastic waves. *Quart. J. Mech. Appl. Math.*, 57:161–179, 2004.

[18] G. R. Feijoo. A new method in inverse scattering based on the topological derivative. *Inverse Problems*, 20:1819–1840, 2004.

[19] M. Bonnet and B. B. Guzina. Topological derivative for the inverse scattering of elastic waves. *Int. J. Num. Meth. Eng.*, 57:161–179, 2004.

[20] H. A. Eschenauer, V. V. Kobelev, and A. Schumacher. Bubble method for topology and shape optimization of structures. *Structural Optimization*, 8:42–51, 1994.

[21] J. Sokolowski and A. Zochowski. On the topological derivative in shape optimization. *SIAM J. Control Optim.*, 37:1251–1272, 1999.

[22] S. Garreau, P. Guillaume, and M. Masmoudi. The topological asymptotic for PDE systems: the elasticity case. *SIAM J. Control Optim.*, 39:1756–1778, 2001.

[23] B. B. Guzina and M. Bonnet. Small-inclusion asymptotic of misfit functionals for inverse problems in acoustics. *Inverse Problems*, 22:1761–1785, 2006.

[24] A. Malcolm and B.B. Guzina. On the topological sensitivity of transient acoustic fields. *Wave Motion*, 45:821–834, 2008.

[25] A. Carpio and M. L. Rapun. Solving inhomogeneous inverse problems by topological derivative methods. *Inverse Problems*, 24:045014, 2008.

[26] M. Bonnet. Inverse acoustic scattering by small-obstacle expansion of a misfit function. *Inverse Problems*, 24:035022, 2008.

[27] M. Masmoudi, J. Pommier, and B. Samet. The topological asymptotic expansion for the Maxwell equations and some applications. *Inverse Problems*, 21:547–564, 2005.

[28] O. Dorn and D. Lesselier. Level set methods for inverse scattering. *Inverse Problems*, 22:R67–R131, 2006.

[29] M. Bonnet. Topological sensitivity for 3D elastodynamics and acoustic inverse scattering in the time domain. *Comp. Meth. Appl. Mech. Eng.*, 195:5239–5254, 2006.

[30] N. Dominguez, V. Gibiat, and Y. Esquerre. Time domain topological gradient and time reversal analogy: an inverse method for ultrasonic target detection. *Wave Motion*, 42:31–52, 2005.

[31] B. B. Guzina and I. Chikichev. From imaging to material identification: a generalized concept of topological sensitivity. *J. Mech. Phys. Solids*, 55:245–279, 2007.

[32] I. Chikichev and B. B. Guzina. Generalized topological derivative for the Navier equation and inverse scattering in the time domain. *Comp. Meth. Appl. Mech. Eng.*, 197:4467–4484, 2008.

[33] C. Bellis and M. Bonnet. A FEM-based topological sensitivity approach for fast qualitattive identification of buried cavities from elastodynamic overdetermined boundary data. *Int. J. Solids Struct.*, 47:1221–1242, 2010.

[34] H. Ammari, J. Garnier, V. Jugnon, and H. Kang. Stability and resolution analysis for a topological derivative based imaging functional. *SIAM J. Contr. Opt.*, 50:48–76, 2012.

[35] Cédric Bellis, Marc Bonnet, and Fioralba Cakoni. Acoustic inverse scattering using topological derivative of far-field measurements-based L^2 cost functionals. *Inverse Problems*, 29:075012, 2013.

[36] B. Greene. Mind over matter. *Smithsonian Magazine*, July-August 2013:22–24, 2013.

[37] N. Dominguez and V. Gibiat. Non-destructive imaging using the time domain topological energy method. *Ultrasonics*, 50:367–372, 2010.

[38] V. Gibiat and P. Sahuguet. Wave guide imaging through time domain topological energy. *Ultrasonics*, 50(2):172–179, 2010.

[39] S. Rodriguez, P. Sahuguet, V. Gibiat, and X. Jacob. Fast topological imaging. *Ultrasonics*, 52:1010–1018, 2012.

[40] M. Kaser and M. Dumbser. An arbitrary high order discontinuous galerkin method of ealstic waves on unstructured meshes – i. the two-dimensional isotropic case with external source terms. *Geophys. J. Int.*, 166:855–877, 2006.

[41] M. Kaser and M. Dumbser. An arbitrary high order discontinuous galerkin method of ealstic waves on unstructured meshes – ii. the three-dimensional isotropic case. *Geophys. J. Int.*, 167:319–336, 2006.

[42] H. Atkins and C.-W. Shu. Quadrature-free implementation of discontinuous galerkin method for hyperbolic equations. *AIAA Journal*, 36, 1998.

[43] A. Logg, K.A. Mardal, and G. Wells. *Automated Solution of Differential Equations by the Finite Element Method: The FEniCS Book*. Springer, 2012.

[44] L.T. Wheeler and E. Sternberg. Some theorems in classical elastodynamics. *Arch. Ration. Mech. Anal.*, 31:51–90, 1968.

[45] A. C. Eringen and E. S. Suhubi. *Elastodynamics*, volume 2. Academic Press, 1975.

[46] Lawrence E. Malvern. *Introduction to the Mechanics of a Continuous Medium.* Prentice-Hall, Englewood Cliffs, New Jersey, 1969.

[47] H. Lamb. On waves in an elastic plate. *Proc. Roy. Soc. London, Ser. A*, 93:114–128, 1917.

[48] H. Kolsky. *Stress Waves in Solids.* Dover, New York, 1963.

[49] K.J. Marfurt. Accuracy of finite-difference and finite-element modeling of the scalar and elastic wave equations. *Geophysics*, 49:533–549, 1984.

[50] S. Ham and K. J. Bathe. A finite element method enriched for wave propagation problems. *Computers and Stuct.*, 94–95:1–12, 2012.

[51] G. Eason, J. Fulton, and I.N. Sneddon. The generation of waves in an infinite elastic solid by variable body forces. *Phil. Trans. Roy. Soc. London*, 248(955):575–607, 1956.

[52] Y.C. Wang, V. Murti, and S. Valliappan. Assessment of the accuracy of the Newmark method in transient analysis of wave propagation problems. *Earth. Eng. Str. Dyn.*, 21:987–1004, 1992.

[53] G. Sadaka. FreeFem++, a tool to solve PDEs numerically. Preprint, Université de Picardie Jules Verne, `http://arxiv.org/pdf/1205.1293.pdf`, 2012.

[54] R.B Blackman and J.W. Tukey. *The Measurement of Power Spectra.* Dover Publications, New York, 1958.

[55] D. Colton and R. Kress. *Inverse Acoustic and Electromagnetic Scattering Theory.* Springer-Verlag, New York, 1998.

[56] D. Colton and R. Kress. *Inverse Acoustic and Electromagnetic Scattering Theory.* Appl. Math. Sci. 93. Springer Verlag, New York, 2nd edition, 1998.

[57] W.H. Reed and T.R. Hill. Triangular mesh methods for the neutron transport equation. Technical Report LA-UR-73-479, Los Alamos, NM, 1973.

[58] B. Cockburn and G. Karniadakis. *Discontinuous Galerkin methods: Theory, computation, and applications.* Springer, 2000.

[59] E.F. Toro. *Riemann Solvers and Numerical Methods for Fluid Dynamics*. Springer, 2009.

[60] B.Q. Li. *Discontinuous Finite Elements in Fluid Dynamics and Heat Transfer*. Springer, 2006.

[61] M. Dumbser and C.-D. Munz. Arbitrary high order discontinuous galerkin schemes. In *IRMA Lectures in Mathematics and Theoretical Physics 7*, 2005. Numerical Methods for Hyperbolic and Kinetic Problems.

[62] M. Kaser, M. Dumbser, J. de la Puente, and H. Igel. An arbitrary high-order discontinuous galerkin method for elastic waves on unstructured meshes - iii. viscoelastic attenuation. *Geophys. J. Int.*, 168:224 – 242, 2007.

[63] C. Castro, M. Kaser, and G. Brietzke. Seismic waves in heterogeneous material: subcell resolution of the discontinuous galerkin method. *Geophys. J. Int.*, 169, 2007.

[64] J. de la Puente, M. Kaser, M. Dumbser, and H. Igel. An arbitrary high-order discontinuous galerkin method for elastic waves on unstructured meshes - iv. anisotropy. *Geophys. J. Int.*, 169, 2007.

[65] J. de la Puente, J.-P. Ampere, and M. Kaser. Dynamic rupture modeling on unstructured meshes using a discontinuous galerkin method. *J. of Geophysical Research*, 114, 2009.

[66] C. Pelties, J. de la Puente, J.-P. Ampere, and G.B. Brietzke. Three-dimensional dynamic rupture simulation with a high-order discontinuous galerkin method on unstructured tetrahedral meshes. *J. of Geophysical Research*, 117, 20.

[67] G.E. Karniadakis and S.J. Sherwin. *Spectral/hp Element Methods in CFD*. Oxford University Press, 1999.

[68] F.Q. Hu, M.Y. Hussaini, and P. Rasetarinera. An analysis of the discontinuous galerkin method for wave propagation problems. *J. of Comp. Phys.*, 151:921 – 946, 1999.

[69] L.C. Wilcox, G. Stadler, C. Burstedde, and O. Ghattas. A high-order discontinuous galerkin method for wave propagation through coupled elastic-acoustic media. *J. of Comp. Phys.*, 229:9373 – 9396, 2010.

[70] M. Kaser and M. Dumbser. A highly accurate discontinuous galerkin method for complex interfaces between solids and moving fluids. *Geophysics*, 73:T23 – T35, 2008.

[71] J.C. Butcher. *The Numerical Analysis of Ordinary Differential Equations: Runge-Kutta and General Linear Methods.* John Wiley & Sons, 1987.

[72] C.-W. Shu and S. Osher. Efficient implementation of essentially non-oscillatory shock-capturing schemes. *J. of Comp. Physics*, 77:439 – 471, 1988.

[73] V.A. Titarev and E.F. Toro. Ader: Arbitrary high order godunov approach. *J. of Scientific Computing*, 17, 2002.

[74] M. Dumbser, M. Kaser, and E. Toro. An arbitrary high-order discontinuous galerkin method for elastic waves on unstructured meshes - v. local time stepping and p-adaptivity. *Geophys. J. Int.*, 171:695 – 717, 2007.